



***PhD with Industrial Characterization
P.O.R. CAMPANIA FSE 2014/2020***

Università degli Studi di Napoli Federico II



Department of Earth, Environmental and Resource Sciences

Ph.D. Thesis

XXXIV CYCLE

Development of an integrated data management system for the monitoring of surficial deformations related to underground mining activity

PhD Candidate

Lorenzo Ammirati

Advisor:

Dott. Nicola Mondillo

Ph.D. Coordinator:

Prof. Vincenzo Morra

Co-Advisor:

Prof. Domenico Calcaterra

Table of Contents

1.	INTRODUCTION AND AIMS OF THE STUDY	5
2.	EARTH OBSERVATION (EO) TECHNIQUE	10
2.1.	INTRODUCTION TO SATELLITE BASED REMOTE SENSING	10
2.2.	SYNTHETIC APERTURE RADAR (SAR)	13
2.2.1.	Interferometric SAR (InSAR)	16
2.2.2.	Differential Sar Interferometry (DInSAR)	17
2.3.	MULTISPECTRAL IMAGING (MSI)	19
2.3.1.	Multispectral satellites	21
2.3.2.	Sentinel-2 data	22
3.	MONITORING LAND SURFACE DEFORMATION ASSOCIATED WITH GOLD ARTISANAL MINING IN THE ZARUMA CITY (ECUADOR)	26
3.1.	ABSTRACT	26
3.2.	INTRODUCTION	27
3.3.	ZARUMA GEOLOGICAL SETTING AND MINING ACTIVITY	28
3.4.	MATERIALS AND METHODS	32
3.5.	RESULTS	36
3.6.	DISCUSSION	42
3.7.	CONCLUSIONS	45
4.	SEMI-REAL TIME SYSTEMS FOR SUBSIDENCE MONITORING IN AREAS AFFECTED BY UNDERGROUND MINING: THE EXAMPLE OF THE NURAXI-FIGUS COAL DISTRICT (SARDINIA, ITALY)	47
4.1.	ABSTRACT	47
4.2.	INTRODUCTION	48
4.3.	HISTORY OF THE MINING ACTIVITY IN THE SULCIS COAL BASIN	49
4.4.	GEOLOGY OF THE SULCIS DISTRICT	51
4.5.	MATERIALS AND METHODS	52
4.6.	RESULTS	56
4.6.1.	Processing phase	56
4.6.2.	Post-processing phase	57
4.7.	DISCUSSION	60
4.8.	CONCLUSION	65
5.	SENTINEL-1 DATA FOR MONITORING A PRE-FAILURE EVENT OF TAILINGS DAM	66
5.1.	ABSTRACT	66
5.2.	INTRODUCTION	67
5.3.	STUDY AREA	68

5.4. DATASET	69
5.5. RESULTS AND DISCUSSION	71
5.6. CONCLUSIONS	73
6. APPLICATION OF MULTISPECTRAL REMOTE SENSING FOR MAPPING FLOOD-AFFECTED ZONES IN THE BRUMADINHO MINING DISTRICT (MINAS GERAIS, BRASIL)	75
6.1. ABSTRACT	75
6.2. INTRODUCTION	76
6.2. GEOLOGICAL SETTING	77
6.3 MAIN FEATURES OF THE BRUMADINHO TAILING DAM B1: STRUCTURE AND GEOCHEMICAL CHARACTERIZATION	80
6.4. METHODS OF STUDY	81
6.5. RESULTS	83
6.6. DISCUSSION	88
6.7. CONCLUSIONS	90
7. DISCUSSIONS AND CONCLUSIONS	91
REFERENCES	94
ACKNOWLEDGMENTS	108
APPENDIX 1	109

1. Introduction and aims of the study

Mineral resources are essential to modern industrial society and human needs to promote their development, as well as, social progression and material prosperity. The dependence on mineral resources represents complex human tasks related to sustainability, new supplies and how to mitigate the environmental impacts of mining activities. Indeed, the mineral exploitation can produce a significant effect on the local environment, and in severe cases resulting in damages, also, leading to geological disasters and environmental pollution. The presence of excavations, dumps and emissions of fine materials resulting from the processing of minerals compromises the quality of the surrounding environment due to the spreading of contaminated elements, mainly heavy metals, responsible for potential risk for the ecosystem (Rodbell et al., 2014). The mining activity can be a major reason of severe environmental and health damage due to the high level of concentration of heavy metals in surface and underground water (Yidana et al., 2008; Armah et al., 2010). In some mining areas was reported the growth of carbon emission and its impact due to the increase of extraction activities (Yang et al., 2021). Sometimes, the carbon emission can rise depending on the mining methods, geological conditions, and coal mine deployment (Wang et al., 2018). Furthermore, subsidence is another unwanted effect of the consequences of mining, with impacts on the environment, buildings and communities (Lopez et al., 2010; Abdallah et al., 2017). The overburden strata above mines may not have suitable support and can collapse generating surface subsidence, both during mining or long after mining has ended (Bell et al., 2000). The size and condition of the subsoil and the geologic features may influence the mode, scale, structure and magnitude of subsidence (Van Sambeek et al., 1997; Potts et al., 2011; Sanmiquel et al., 2018; Marian et al., 2020). Most mining areas are adjacent to dense towns, where ground subsidence causes damage to buildings, outages of transmission networks, and transport (Villegas et al., 2011; Tong et al. 2013; Teng et al., 2016; Vušović et al., 2020; Li et al., 2021; Akcin et al., 2021). Sometimes, the subsidence can be sudden and its chain effect may be catastrophic, such as increasing the gas pressure and setting up the mine fire (Ünver et al., 2019). From this point of view, it is essential to not underestimate the potential effects of mining activities. Constant monitoring of mineral resource exploitation and its effects on the ecological environment is essential for improving the sustainable development of mine operations, reducing and mitigating damage caused by exploitation. Furthermore,

mining monitoring is of greatest importance, not only for the scientific community but also for the mine companies, to reduce the potential effects and consequences. However, some mining monitoring techniques, as well as GPS and levelling have a cost of implementation that is significantly expensive for the management and the acquisition of information on large spatial and temporal scales of the entire mining area. One of the most important and valuable time-savings techniques, that has been recently developed, is remote sensing. The method allows to prevent and investigate instabilities and environmental impacts, through a rapid acquisition mode and simple data management, at relatively low costs. Among the different existing techniques, satellite monitoring is a technology that represents nowadays a very helpful and relevant supporting tool for the monitoring of mining areas. For instance, the interferometric Synthetic Aperture Radar (InSAR) technique was successfully used for the monitoring and measurement of surface deformation in several mining areas (Guéguen et al., 2009; Samsonov et al., 2013; Zhao et al., 2013; Pawluszek et al., 2020; Chen et al. 2021). The InSAR technique can not only overcome the limitations of traditional methods but can also obtain higher resolution, also reaching the centimeters level surface deformations. The application of the interferometric technique in mining areas improves the study of the temporal evolution of mining deformation (Zhang et al., 2015; Grzovic et al., 2015; Dong et al., 2015; Mura et al., 2016; Antonielli et al., 2021; Pawluszek et al., 2020;). This remote analysis was a very valuable instrument for monitoring, also, in mining infrastructure such as tailings dams identifying surface displacements useful for the prediction of catastrophic failures (Mura et al., 2018; Iannacone et al., 2018; Mazzanti et al., 2021). In addition to interferometric techniques, the use of optical sensors, such as the Multispectral Instrument (MSI), provides an excellent way to study the potential effects of mining activities on the environment. Last year, the increasing availability of high-resolution satellite imagery offered data with optimal spatial and temporal scales. The multispectral images allow the quantification of changes in land cover and land use over time (Demirel et al., 2011; Nascimiento et al., 2020). The MSI technique is very useful to detect unauthorized mining activities that cause negative effects on the environment (Lobo et al., 2017; Londoño et al., 2022).

The general idea of this research project was to assess the integration of different remote sensing techniques to carry out comprehensive mining monitoring. The development of an integrated platform in near-real time for mine safety is of

fundamental importance to identify, in a preliminary way and on a large scale, critical situations, allowing savings in terms of costs and investigation time as well as minimizing the risk for operators. The Ph.D. project is composed of four study cases, each one explaining in detail the application of remote sensing to mining monitoring and management. The chapters are organized following the structure of several papers that have been published during the Ph.D. or that are now in revision. The thesis ends with a discussion and conclusion chapter, which includes a summary of the knowledge acquired during this work. The areas of interest were located in three different nations: Ecuador, Brazil and Italy. The work provided the application of two satellite-based remote sensing methods: the DInSAR technique and the multispectral analysis.

- The DInSAR technique was used for three cases: 1) the investigation of terrain deformation associated with shallow artisanal mining in the Zaruma city in Ecuador, 2) the investigation of subsidence phenomena due to underground mining in the municipality of Nuraxi Figus (Carbonia-Iglesias province) in south-west Sardinia, Italy, and 3) the analysis of surficial displacements related with a tailing dam located in Brumadinho area in Minas Gerais region, Brazil.

- The multispectral analysis was used for investigating the areas affected by the huge flood related to the collapse of the upstream tailing dam of Vale's Córrego do Feijão located to Minas Gerais, Brazil, occurred on the 25 January 2019. The system allowed to classify at different times, the land, vegetation, and water using surficial spectral properties. The MSI technique was used to analyze a possible cause/effect relationship due to the tailing dam failure and to try to understand if this type of monitoring is reliable and able to recognize any changes in the concentration of pollutants.

In this Ph.D. project, the interferometric and multispectral products derived from Sentinel-2 (More details chapter 2.3.2), COSMO-SkyMed and Sentinel-1 (More details chapter 2.2.2) satellites were acquired, processed, and examined.

As written above, several parts of this Ph.D. thesis correspond to the content of the following papers published or submitted:

- I. Monitoring Land Surface Deformation Associated with Gold Artisanal Mining in the Zaruma City (Ecuador) Published in "Remote Sensing Journal"

Reference: Ammirati, L.; Mondillo, N.; Rodas, R.A.; Sellers, C.; Di Martire, D. Monitoring Land Surface Deformation Associated with Gold Artisanal Mining in the Zaruma City (Ecuador). *Remote Sensing* 2020, 12, 2135. <https://doi.org/10.3390/rs12132135>.

Contributions of L.Ammirati to the paper: methodology, DinSAR processing, interpretation of the data. L.Ammirati wrote the first version of the manuscript that was revised and integrated by the co-authors.

- II. Semi-real time systems for subsidence monitoring in areas affected by underground mining: the example of the Nuraxi-Figus coal district (Sardinia, Italy). Submitted in *Engineering Geology*.

Reference: Ammirati, L.; Mondillo, N.; Di Martire, D.; Russo, G.; Bordicchia, F.; Calcaterra, D. Semi-real time systems for subsidence monitoring in areas affected by underground mining: the example of the Nuraxi-Figus coal district (Sardinia, Italy). *Submitted*.

Contributions of L.Ammirati to the paper: methodology, DinSAR processing, interpretation of the data, numerical modelling. L.Ammirati wrote the first version of the manuscript that was revised and integrated by the co-authors.

- III. Sentinel-1 data for monitoring a pre-failure event of the tailings dam. Published in “Lecture Notes in Civil Engineering, Springer Cham”.

Reference: Ammirati L., Mondillo N., Calcaterra D., Di Martire D. (2021) Sentinel-1 Data for Monitoring a Pre-failure Event of Tailings Dam. In: Rizzo P., Milazzo A. (eds) *European Workshop on Structural Health Monitoring. EWSHM 2020. Lecture Notes in Civil Engineering*, vol 128. Springer, Cham. https://doi.org/10.1007/978-3-030-64908-1_13.

Contributions of L.Ammirati to the paper: methodology, conceptualization, DinSAR processing, interpretation of the data. L.Ammirati wrote the first version of the manuscript that was revised and integrated by the co-authors.

- IV. Application of multispectral remote sensing for mapping flood-affected zones in the Brumadinho mining district (Minas Gerais, Brasil). Submitted in *Remote Sensing Journal*.

Reference: Application of multispectral remote sensing for mapping flood-affected zones in the Brumadinho mining district (Minas Gerais, Brasil). *Submitted*.

Contributions of L.Ammirati to the paper: methodology, conceptualization, Sentinel-2 processing, interpretation of the data. L.Ammirati wrote the first version of the manuscript that was revised and integrated by the co-authors.

2. Earth Observation (EO) technique

2.1. Introduction to Satellite based remote sensing

Satellite based remote sensing is an earth observation (EO) technique allowing to acquire qualitative and quantitative information from a sensor (active or passive) placed on a platform (satellite-based) at a certain distance from the object of study. The technology provides a valuable structure to accurately map and monitor large-scale phenomena in a well-timed approach. Whatever the used sensor, when the electromagnetic radiation hits an object, it may be transmitted, absorbed, or reflected. In the last three decades, many applications have developed for using satellite-based remote sensing, but all are based on two types of sensors: active or passive (Fig. 2.1). The former emits radiation in the direction of the target to be examined and detects the scattered reflectance, whereas the latter detects natural radiation that is emitted or reflected by the object or scene being observed. The remote sensors can measure radiation in the visible or infrared wavelengths (700 nm – 1 mm), but also in the larger wavelengths as microwave (1 mm – 1 m) (Figure 2.2).

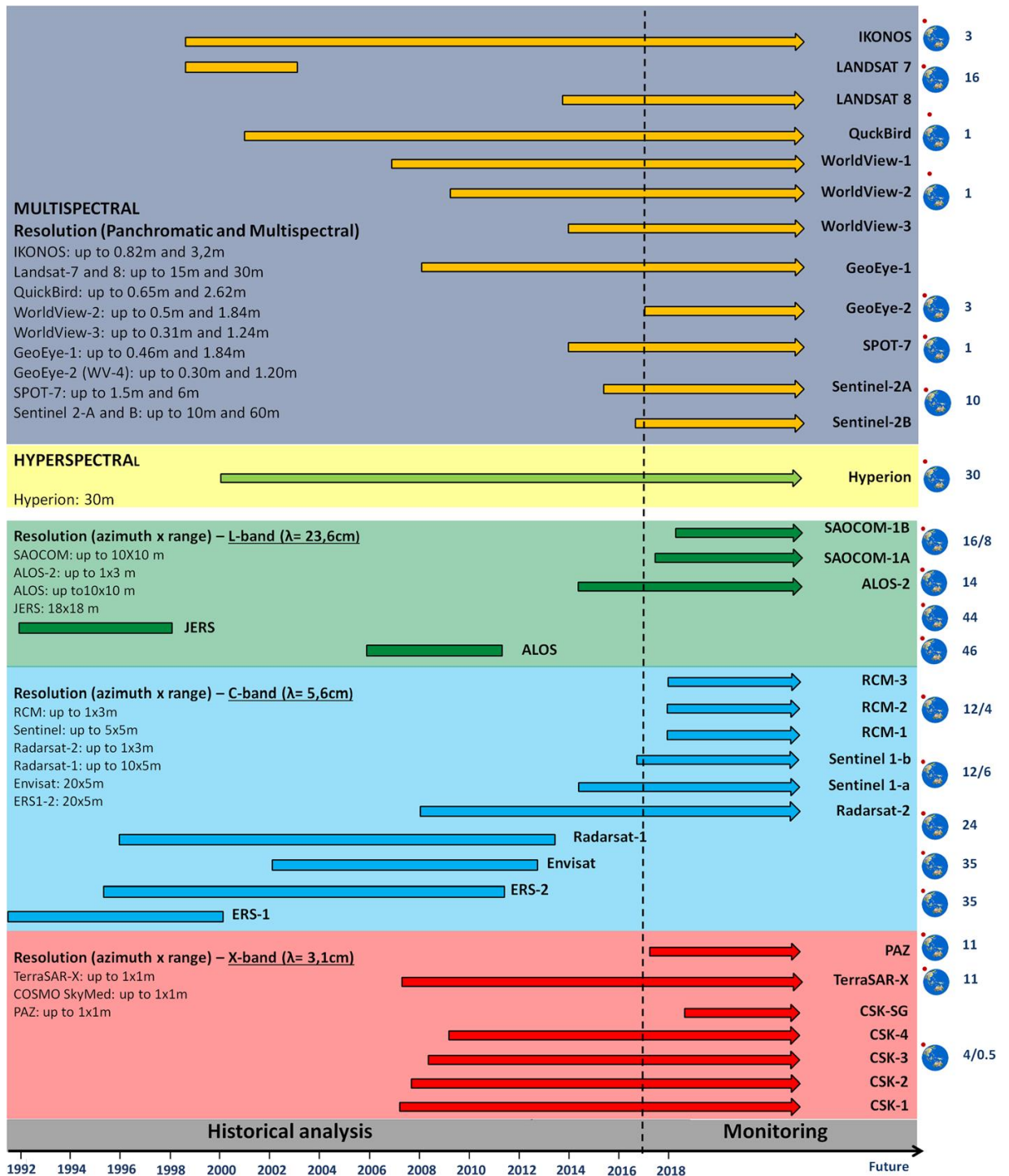


Figure 2.1. Active optical and SAR satellites, on right the revisiting time (Casagli et al., 2017).

The majority of active sensors operate in the microwave portion of the electromagnetic spectrum, as radio detection and ranging (Radar) remote sensing, which makes them able to penetrate the atmosphere under most conditions. Another active system is the Light Detection And Ranging (LiDAR). An active technique, like the SAR interferometry, views the target from either end of a baseline of known

length. The change in apparent view direction is related to the absolute distance between the instrument and target. The passive sensor types receive object reflectance that is illuminated from an additional light source, for instance, the sun. Passive sensors include different types of radiometers and spectrometers. Most passive systems used in remote sensing applications operate in the visible, infrared, thermal infrared, and microwave portions of the electromagnetic spectrum. Optical sensors are usually passive sensors, such as multispectral satellites. These sensors collect different spectral ranges, that are called bands and can vary in their number and width per sensor. The remote sensing applied to mine activity allows to analyze large areas and examine the distribution of an event, observing how the phenomenon evolves, even in the short term, such as the subsidence that is often linked to heavily exploited mining areas. Multispectral imagery allows the application of processing techniques to distinguish or enhance certain properties of materials. Combining the different remote sensing data with other types of information (field data), it is possible to improve the results. The study is based on two types of spaceborne datasets, the Synthetic Aperture Radar (SAR) imagery for the analysis of the ground deformation evolution and the Multispectral imagery (MSI) for the identification of the environmental footprint of mining operations due to the extraction site, tailing pond, and processing plant.

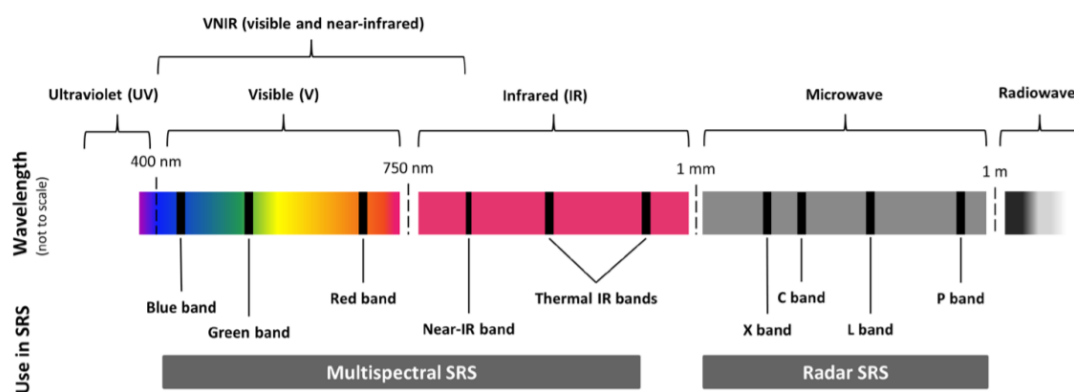


Figure 2.2. The spectrum of electromagnetic radiation with bands used in satellite remote sensing (SRS) (Pettorelli et al., 2014).

2.2.Synthetic Aperture Radar (SAR)

Synthetic Aperture Radar (SAR) is an instrument consisting of a conventional radar mounted on a platform (the ground, airplane, or satellite) that transmits radiation reflected by the target and acquired again. SAR image is a projection in the sensor's acquisition plane, slant-range plane, of the targets placed on the Earth surface, the ground-range plane. The radar antenna is pointed to the ground orthogonally to the direction of motion of the platform with an angle between 20 and 60 degrees compared to the direction of Nadir (called off-nadir) (Ferretti et al., 1998). The SAR can generally distinguish the reflected signals coming from different targets only according to the return time of the signal. The wavelength of the sensor determines the diffusion of the signal into targets. The most used frequency bands in civilian spaceborne SAR missions are the L-band, C-band, and X-band. Different kinds of geometries acquisition characterized the SAR imagery (Fig. 2.3), according to the system configuration:

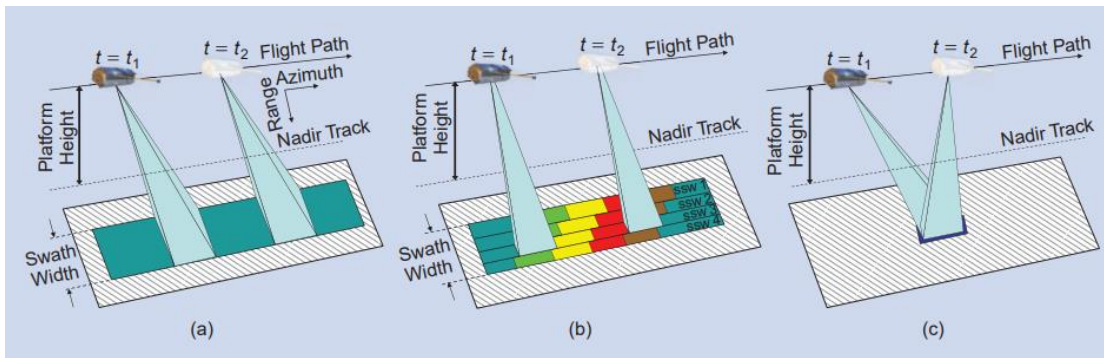


Figure 2.3. SAR Stripmap (a), ScanSAR (b), and Spotlight (c) acquisition modes (Moreira et al., 2013)

- Stripmap: Antenna pointing is fixed relative to the flight line. In this case, the result of the acquisition is a moving antenna footprint sweeping along a terrain strip parallel to path motion. The stripmap mode is usually applied for the mapping of large areas.
- ScanSAR: The sensor drives the antenna beam to illuminate a strip of terrain at any angle to the path of platform motion. The assumption is that with the ScanSAR mode, it is possible to share the radar operation time between two or more separate sub-swaths to obtain full image coverage of each of them.
- Spotlight: the sensor steers its antenna beam to continuously illuminate the terrain patch being imaged. The spotlight acquisition allows to have finer

azimuth resolution than in the other ways, even using the same physical antenna; moreover, spotlight imagery provides the possibility of imaging a scene at multiple viewing angles during one single pass.

Sometimes the SAR acquisition produces a geometric distortion or shadow depending on the relationship between the off nadir angle and the terrain relief (Figure 2.4). When the radar beam reaches the base of a tall feature tilted towards the radar before it reaches the top, foreshortening will occur. The fore-shortened areas appear brighter in the SAR image, due to the compression into a smaller image part of the backscattered slope. If the radar ray reaches the top of a tall feature before the base, the return signal receives the information from the bottom. As a result, the top of the feature is displaced towards the radar from its true position on the ground, and pose on top of the base of the feature. Layover areas are usually characterized by very high-intensity values. The foreshortening and layover can produce radar shadow. Radar shadow occurs when the radar beam is not able to illuminate the ground surface. The consequence of shadowing on the final image is the darkness on objects on the surface not backscattered.

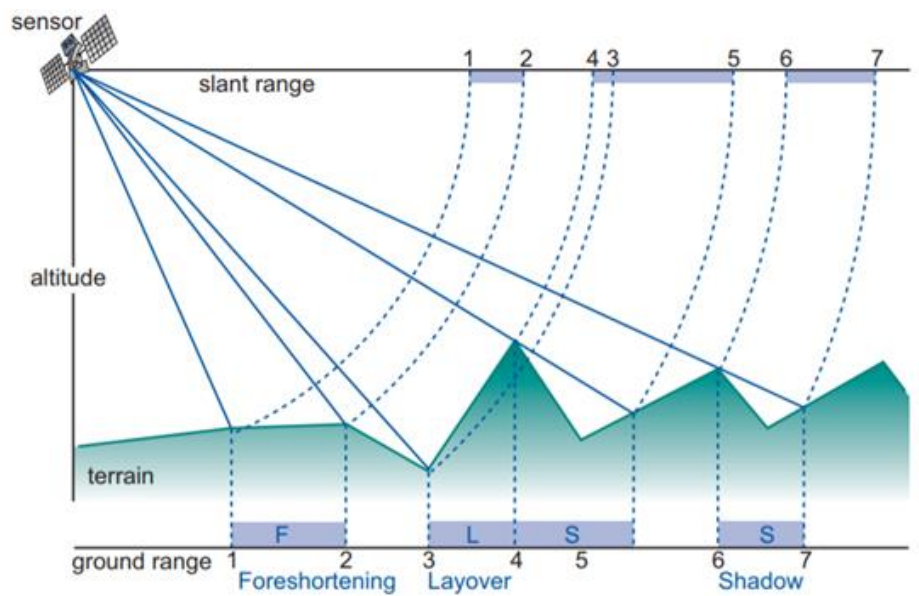


Figure 2.4. Geometric distortions in SAR imagery due to topography (Tempfli et al., 2009).

Among the main spaceborne SAR satellites, the ERS-1, and ERS-2 (European Remote Sensing Satellites) were launched in 1991 and 1995, respectively. These, in C-band and with an incidence angle of 23° and a resolution of $20\text{m} \times 4\text{m}$, were in charge of collecting data associated with the land surface, ocean, polar caps, and

natural disasters. The satellites were deactivated in 2000 (ERS-1) and 2011 (ERS-2). The Advanced Synthetic Aperture Radar (ASAR) on the ENVISAT satellite is an improved version of the sensors occurring on ERS. With a moderate resolution of 20 m, ENVISAT has been used for extracting information from local to global, on the management of Earth's resources, including insights into factors contributing to climate changes. The ENVISAT mission ended in 2012. More recently, several SAR sensors are operating at radar wavelengths L-band (23 cm), C-band (5 cm), and X-band (3 cm), such as RADARSAT-2 (RCM, C-band), Sentinel-1 (C-band), TerraSAR-X (X-band), COSMO-SkyMed (CSK1-4, X-band), ALOS (L-band), SAOCOM (L-Band) the satellites (Figure 2.1). In particular, the COSMO-SkyMed (CONstellation of small Satellites for Mediterranean basin Observation) is a satellite mission managed by the ASI (Italian Space Agency) and the Italian Ministry of Defense. The CSK system is made up of four satellites and it is equipped with High-Resolution SAR, in sun-synchronous polar orbits, phased in the same orbital plane. This results in varied intervals between the satellites along the same ground track of between 1 and 16 days. The Sentinel-1 mission is expected to deliver a wealth of data and imagery that are central to the Copernicus joint initiative of the European Commission (EC) and European Space Agency (ESA). As the first member of the constellation of two satellites, launched in 2014 and the second in 2016. Sentinel-1 includes C-band imaging Synthetic Aperture Radar (SAR) in four exclusive imaging modes: Interferometric Wide Swath Mode (IW), Wave-Mode(WM), Strip Map Mode (SM), and Extra-Wide Swath Mode (EW). With different resolutions (from 5m to 40m) and coverage (from 80 km to 400 km), the four modes can meet the demanding image quality and swath width requirements (More details about the spaceborne Sar missions and their applications: Schmullius et al. 1997, Musa et al. 2015, McNairn et al. 2016, Zakhvatkina et al. 2019, Baek et al. 2019, El Kamali et al. 2020, Ho Tong Minh et al. 2020)

2.2.1. Interferometric SAR (InSAR)

The Interferometric Synthetic Aperture Radar (InSAR – Gabriel et al., 1989) is a method largely used to study deformations caused by earthquakes, volcanic eruptions, glacier movements, landslides, and subsidence to a precision of a few centimeters or less (Massonnet et al., 1998; Franceschetti et al., 1999; Bürgmann et al., 2000; Madsen et al., 2000; Sansosti et al., 2006; Bozzano et al., 2011; Carlà et al., 2019; Meng et al., 2020). The interferometry technique uses two SAR images of the same area acquired at different times and processes them, resulting in maps called interferograms that show ground-surface displacement between the two time periods. The interferometric images are processed in such a way that both amplitude and phase information is preserved for each pixel. Where the amplitude identifies the portion of the electromagnetic field incident on all objects of the ground resolution cell and backscattered towards the sensor. The phase values are the basic information for all interferometric techniques, summarised in the following equation:

$$\Phi = \psi + \frac{4\pi}{\lambda}r + \alpha + n$$

Where ψ represents the target reflectivity, λ is the radar wavelength used, α is the atmospheric factor, r is the distance between the sensor and the target, n is the noise due to Earth's curvature, the signal-to-noise ratio (SNR) and the instrument noise. The interferometric phase difference between the two observations, corresponding to the path difference between two acquisitions, is proportional to the relationship between a complete phase cycle in radians and the wavelength λ , which is the distance between the two following points, all multiplied for Δr (Ferretti et al., 2007). The phase can be influenced by different factors, due to the interferometry or by instrumental sources. Geometrical decorrelation and temporal decorrelation belong to the first category, mean-while in the second group instability of radar frequency and thermic instrumental noises can be mentioned. The map describing the phase difference between two SAR images is the so-called interferogram where the phase is highly correlated to the terrain topography and deformation patterns can be mapped.

2.2.2. Differential Sar Interferometry (DInSAR)

The DInSAR is the combining the phase using multi-temporal SAR images where the phase shift related to topography is removed from the interferograms and the difference between the resulting products will show surface deformation patterns that occurred between the different acquisition dates. Through the development of more advanced techniques, the deformation velocity is calculated as a weighted average computed from the single interferograms, allowing then to retrieve the mean deformation rate of the investigated area. There are three processing approaches grouped into categories: Persistent Scatterers (PS) (Ferretti et al., 2000; Costantini et al., 2000; Werner et al., 2003; Crosetto et al., 2008), Small Baselines Subset (SBAS) (Berardino et al., 2002; Mora et al., 2003; Samsonov & d'Oreye, 2012) and methods that combine PS and SBAS as SqueeSAR (Ferretti et al., 2011). The first so-called Permanent Scatterers Interferometry SAR (PSInSAR, Ferretti, et al., 2001) is one of the basic algorithms belonging to the PS category. Phase and amplitude are the main parameters exploited by the PSInSAR method: Amplitude gives information about the reflectivity of the target, while the phase indicates the sensor-target distance; therefore, amplitude allows to individuate PS and phase to estimate the movement of the PS. Persistent Scatterers (PS) are targets that keep stable the electromagnetic signal (hence, their reflectivity property) during the period of acquisition of the image. Usually, PSs correspond to man-made structures (i.e. buildings, dams, infrastructures, etc.) or to rocky outcrops, while vegetated areas, due to the frequent variation of their electromagnetic properties, cannot be considered as good scatterers. The PS detection is based on the amplitude dispersion, which is calculated by dividing the temporal standard deviation of the amplitude by the temporal mean of the amplitude of a certain pixel in a stack of SAR images. The concept is that a pixel characterized by a high and more or less constant amplitude value is assumed to show a low phase dispersion (Ferretti et al., 2001). The result is a precise measurement of the movements along the SAR Line Of Sight (LOS velocities) of each PS, concerning an assumed reference point (regard as stable), in the time interval. While the SBAS approach is an algorithm capable of retrieving temporal series of deformation exploiting interferograms characterized by small temporal and spatial baseline. This algorithm aims to limit the spatial decorrelation taking into account the spatial and the temporal information from the SAR data (Berardino et al., 2002). These interferograms are used as inputs to calculate the unwrapping stage, from which the

estimation of the topographic contribution and the extraction of the Low Pass (LP) temporal deformation, which will be subtracted from the wrapped interferogram module 2π , is done. Therefore, the interferograms will be considered as residual phase and be unwrapped. Therefore, the spatial and temporal filters are applied to unwrapping the temporal deformation and the topographic phase residual. Finally, the inversion of the stack of interferograms is guaranteed using the singular value decomposition (SVD) method. The advantage of the SBAS technique is represented by the high coherence and the high spatial density of the final product, and the reduction of the errors due to the redundancy of the information (more interferograms for every image), although disadvantages are due to the high computational requests. The third approach is a hybrid methodology that uses the process PS and retrieving phase from many small targets with similar scattering, called distributed scatterers (DS).

DS is mainly over natural land covers and is affected by temporal and geometrical decorrelation. The mixed approach increases the spatial density of measurement points over areas characterized by DS, preserving the quality information obtained using the PS technique. SqueeSAR™ is the algorithm, mixed PS and DS process-based, that provides significantly increase coverage points, mainly in non-urban areas. In particular, starting to spatially average the data over statistically homogeneous areas, it is possible to increase the signal-to-noise ratio (SNR), obtain a high coherent of the point scatterers without the need to perform a time-consuming phase unwrapping procedures on hundreds of interferograms. The SqueeSAR advantages are an increase of the spatial density of valid pixels, and an achieve a larger coverage of the measurement. In addition, the mixed approach provides a high quality of the displacement time-series of the DS.

2.3. Multispectral imaging (MSI)

A multispectral image measures the Earth's reflected radiance in specific wavelength bandwidths or spectral bands, from visible and near-infrared (VNIR) to Short-wave infrared (SWIR). The MSI image of an object is acquired, registered, and calibrated in a series of spectral bands, and uploaded into the reflectance. The structure can be associated to a cube. This is characterized by the X and Y axes related to the pixels of each image, while the Z dimension symbolizes the reflectance information of spectral bands (Figure 2.5). From the cube, it is possible to reconstruct the reflectance spectrum for each pixel of the image. Typically the multispectral imaging measures light in a number of tens of spectral bands, from 3 to 15.

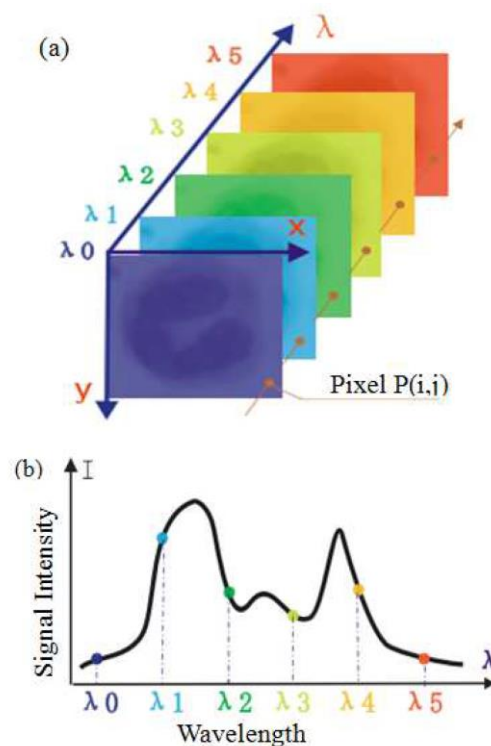


Figure 2.5. In the multispectral image cube, the λ is reflectance information (a). (b) Spectrum at pixel $P(I,j)$ (Wu et al., 2009).

Wavelengths can be separated by filters or using sensitive instruments to particular wavelengths, including light from frequencies beyond the range of visible light, infrared and ultraviolet. Spectral imaging can allow the extraction of additional information that the human eye cannot capture with its red, green, and blue receptors. The MSI sensors usually installed on mobile platforms (satellite or airborne), can collect and record the energy reflected or emitted from the surface, allowing to determine the characteristics of the material targeted. In principle, a material can be identified from its spectral reflectance signature if the sensing system has sufficient

spectral resolution to distinguish its spectrum from those of other materials. The percent reflectance values for each pixel of MSI image may be associated with features such as water, sand, roads, forests, etc. can be plotted and compared with each other (Fig.2.6).

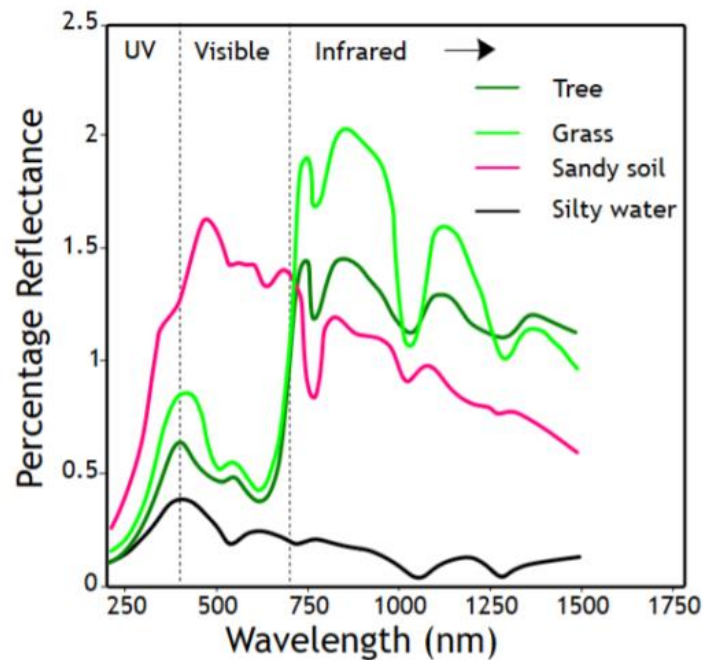


Figure 2.6. The main spectra reflectance (or curves) for distinct types of land cover (Pettorelli et al., 2014).

Such information is comprised in spectral response curves or spectral signatures. The more detailed the spectral information recorded by a sensor, the more information that can be extracted from the spectral signatures. Differences in spectral signatures are used to help classify remotely sensed images into classes of landscape features since the spectral signatures of like features have similar shapes. For instance, it is possible to recognize different groups of minerals and rocks, for example, hydroxides, carbonates, and some hydrothermal alteration minerals (Bedell, 2004; Roberts et al., 2019; Qiu et al., 2021).

2.3.1. Multispectral satellites

One of the first MSI satellite date back to 1967 with the Earth Resource Technology Satellite (ERTS) program (later Landsat). The satellite had a mid-resolution and allowed to study the land use, vegetation and agricultural developments, water and environmental quality, soils, geology. More recently, the main high-resolution MSI satellites with the best spatial and temporal resolution for the analysis of land cover changes are Landsat-8 and Sentinel-2. These satellites managed, respectively, by the United States Geological Survey and the European Space Agency allowed to obtain a temporal resolution of images every 3-5 days, and therefore, to develop products at higher spatial resolution (10-30 m). Landsat-8 offers moderate resolution (15 m–100 m, depending on spectral frequency) measurements of the Earth's terrestrial and polar regions in the visible, near-infrared, short wave infrared, and thermal infrared. The satellite is configured by two science instruments the Operational Land Imager (OLI) and the Thermal InfraRed Sensor (TIRS). These two sensors provide seasonal coverage of the global land at a spatial resolution of 30 meters (visible, NIR, SWIR), 100 meters (thermal), and 15 meters (panchromatic). The spectral coverage and radiometric performance are designed to detect and characterize the multi-decadal land cover change in concert with historic Landsat data. The scene size is 185 km cross-track by 180 km along the track. The satellite measures different ranges of frequencies along the electromagnetic spectrum in 11 bands. Landsat numbers its red, green, and blue sensors as 4, 3, and 2, so when we combine them we get a true-color image (Figure 2.7). The Sentinel-2 is a polar-orbiting, multispectral high-resolution imaging mission for land monitoring specifically designed for the operational needs of the Copernicus program managed by the ESA. The Sentinel-2 mission comprises a constellation of two polar-orbiting satellites (Sentinel-2A and Sentinel-2B) placed in the same orbit, phased at 180° to each other. It aims at monitoring variability in land surface conditions with a 5 day revisit time at the equator. Sentinel-2A was launched on 23 June 2015 and Sentinel-2B followed on 7 March 2017. The thirteen Sentinel-2 bands and their combinations the visible (Figure 2.7), Near-Infrared (NIR), and Short-wave Infrared (SWIR). The Global coverage of land is between 84° S and 84°N with the revisiting time of 5 days or 10 days. Multispectral image acquisition in 13 visible and infrared bands and the resolution depending on the spectrum band of 10, 20, and 60 meters. Sentinel-2 carries an innovative wide swath high-resolution multispectral imager with 13 spectral bands for a new perspective of our land and

vegetation. The combination of high resolution, novel spectral capabilities, a swath width of 290 km, and frequent revisit times provides unprecedented views of Earth.

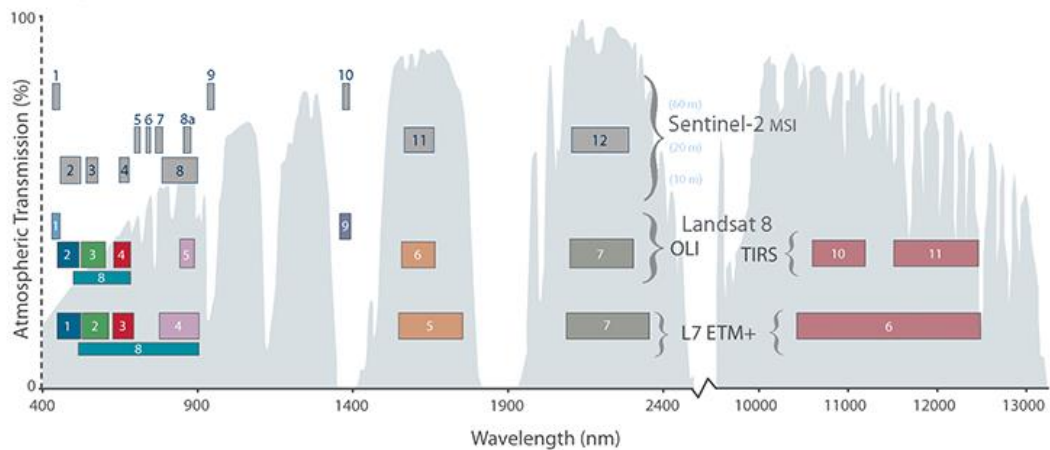


Figure 2.7. Comparison of Landsat 7 and 8 bands with Sentinel-2 (www.usgs.gov).

2.3.2. Sentinel-2 data

In this Ph.D. project, the Sentinel-2 MSI products have been used. There are several different types of MSI available products, which are distinguished as follows: Level-0, Level-1A, Level-1B, Level-1C, and Level-2A. Level-0 and Level-1A are not made available to common users. The least processed product type that is made available to all users is Level-1B. The product delivers radiometrically corrected Top of Atmosphere (TOA) reflectance. The latter is the measurement that provides the ratio of radiation reflected by the incident solar radiation on a given surface. The radiometric corrections that are applied to a Level-1B product are dark signal, pixel response non-uniformity, crosstalk correction, defective pixel interpolation, high spatial bands restoration, and binning for 60m bands (www.sentinel2.copernicus.eu). The Level-1C product consists of 100 km² images in UTM/WGS84 projection. This product is the result of using a DEM to project the image. The measurements are provided per pixel and it is necessary the TOA reflectance correction. This product also contains Land/Water and Cloud masks and data that contain information on the total column of ozone/water vapor and the mean sea level pressure. The Level-2A product is also divided into tiles of 100 km², which are projected in UTM/WGS84. This type of product contains Bottom-of-atmosphere (BOA) reflectance images, which are the actual reflectance of the areas on the surface of the Earth. The Level-1C and Level-2A product can be processed and examined by using the Sentinel-2 Toolbox.

The Sentinel-2 toolbox, available online is part of the Sentinel Application Platform (SNAP) (ESA), the common architecture for Sentinel-1, -2, and -3 made available by ESA. This software contains a lot of tools to exploit the data from the MSI instrument of the Sentinel-2 mission. It is also possible to use Landsat 8 (or MODIS) data with SNAP but the data is presented in individual bands. Sometimes it is necessary to use the Level-1C products and apply the TOA correction to convert them to a Level-2A product. The atmospheric correction is critical when comparing images acquired from different sensors. This is done by algorithms, which have been developed by DLR/Telespazio and can be run from the Sentinel-2 Toolbox. The module is called Sen2Cor and has to be installed manually and depending on the operating system available online (<http://step.esa.int>). The algorithm executes at the native resolution of the bands (either 10, 20, or 60m). The tool starts by processing with the data at a 60m resolution, followed by processing at 20m, and finally ending at a 10m resolution. After the TOA correction, it is possible to choose to process the data at 10, 20, and 60 m resolution for several applications. A useful function is Band Maths used to create new image sample values derived from existing bands, tie-point grids, and flags. The source data can originate from all currently open and spatially compatible input products. This can be combined with arbitrary mathematical expressions to generate the target data. By default, a new image view is automatically opened for the new sample values. This tool can be used to obtain the spectral indices developed based on the spectral properties of the object of interest. The indices are used to enhance particular land surface features or properties, e.g. vegetation, soil, water (<https://custom-scripts.sentinel-hub.com/custom-scripts/sentinel-2/indexdb>).

For instance, the spectral indices of vegetation are developed based on the principle that the healthy vegetation reflects strongly in the near-infrared (NIR) spectrum while absorbing strongly in the visible red (Asner, 1998; Xue et al., 2017). One of the most popular spectral indices is the Normalized Difference Vegetation Index (NDVI) (JARS, 1993), defined as

$$NDVI = \frac{NIR-red}{NIR+red}$$

NDVI values range from -1 to 1, where higher values demonstrate healthy vegetation, while non-vegetated areas show low values. Negative values of NDVI correspond to

water. Values close to zero (-0.1 to 0.1) generally correspond to barren areas of rock, sand, or snow (Figure 2.3.2.1).

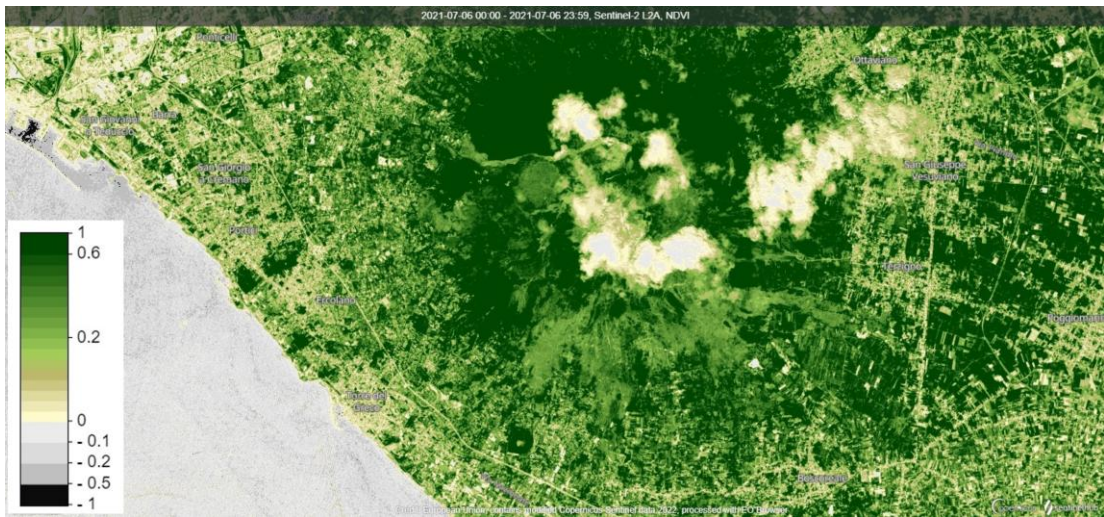


Figure 2.3.2.1. An example of NDVI maps in the Vesuvian area (Naples, Campania)

Another application is to display a Colour Composite of bands. Often, a combination is created of three individual monochrome images, in which each is assigned a given color. Color composites are usually expressed as R G B where: R is for red color, G stands for green color, and B for blue color. It is possible to assign whichever band information to RGB to the aim of the study. For instance, the RGB combination of the bands 7,3,2 corresponds to the “False Color” map (Figure 2.3.2.2) that uses near-infrared, red, and green bands common to assess plant density and health.

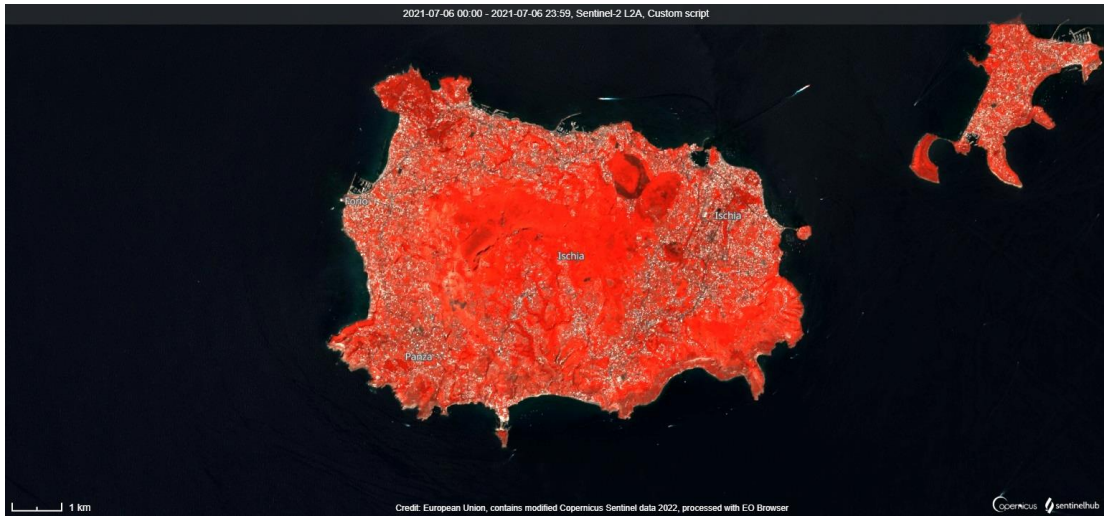


Figure 2.3.2.2. The 7,3,2 band compositive maps of Ischia and Procida (Naples, Campania)

Since the vegetation reflects more near-infrared than green, appears deep red. While the cities and exposed ground are gray and water appears blue or black (<https://earthobservatory.nasa.gov/features/FalseColor>).

3. Monitoring Land Surface Deformation Associated with Gold Artisanal Mining in the Zaruma City (Ecuador)

3.1. Abstract

Underground mining can produce subsidence phenomena, especially if orebodies are surficial or occur in soft rocks. In some countries, illegal mining is a big problem for environmental, social, and economic reasons. However, when unauthorized excavation is conducted underground, it is even more dangerous because it can produce unexpected surficial collapses in areas not adequately monitored. For this reason, it is important to find quick and economic techniques able to give information about the spatial and temporal development of uncontrolled underground activities in order to improve the risk management. In this work, the differential interferometric synthetic aperture radar (DInSAR) technique, implemented in the SUBSOFT software, has been used to study terrain deformation related to illegal artisanal mining in Ecuador. The study area is located in Zaruma (southeast of El Oro province), a remarkable site for Ecuadorian cultural heritage where, at the beginning of the 2017, a local school collapsed, due to sinkhole phenomena that occurred around the historical center. The school, named “Inmaculada Fe y Alegria”, was located in an area where mining activity was forbidden. For this study, the surface deformations that occurred in the Zaruma area from 2015 to 2019 were detected by using the Sentinel-1 data derived from the Europe Space Agency of the Copernicus Program. Deformations of the order of five centimeters were revealed both in correspondence of known exploitation tunnels, but also in areas where the presence of tunnels had not been verified. In conclusion, this study allowed to detect land surface movements related to underground mining activity, confirming that the DInSAR technique can be applied for monitoring mining-related subsidence.

3.2.Introduction

In several countries, mining activity is vital for social and economic development. Sometimes, the exploitation of deposits is related to resources of high economic value, increasing the interest both of mining companies and artisanal miners. Artisanal and small-scale mining (AMS) is recognized as a considerable source of revenue for millions of people in about 80 countries worldwide (www.gold.org). ASM takes place in several regions of the world, mostly in the global South—sub-Saharan Africa, Asia, Oceania, Central and South America. In 2017, about 40 million people worldwide were working in the artisanal mining sector and the industry had a significant impact on global mining (www.mining-technology.com). These small-scale operations, which are typically undertaken outside the law and without compliance with industry standards, can promise great rewards. However, violations of rules are quite common, and these activities can damage and pollute the territory environment. In certain environments, mining activity can produce subsidence phenomena (Bell et al., 2000, Gee et al., 2017) and can be even more dangerous if it is carried out illegally because it can produce unexpected sinkholes (Gutiérrez et al., 2014; Parise et al., 2015; Gee et al., 2017; Fazio et al., 2017) in areas not adequately monitored. Monitoring and parameterization of these dynamic processes are particularly relevant. Over the last years, several monitoring methods have been used, including remote sensing techniques. Remote sensing has proved to be highly suitable for these and for many other necessities, since it captures data covering vast study areas. Among the different types of remote sensing techniques, one that very well meets dynamic processes requirements is the differential interferometric synthetic aperture radar (DInSAR). In recent years, DInSAR techniques have been effectively used to measure surficial deformations related to subsidence phenomena (Fiaschi et al., 2017) and to monitor underground mining activity (Fan et al., 2015; Przylucka et al., 2015; Du et al., 2016; Pawluszek et al., 2020; Pawluszek et al., 2020). The hills of Zaruma and Portovelo (El Oro province, Ecuador) have been mined for gold and silver for centuries. The Incas were already extracting gold and silver in the area with hydraulic mining of the oxidized parts of veins. In 1549, Mercadillo, one of Pizarro's force, following upstream the Amarillo River encountered the Inca mine and founded the town of Zaruma (Billingsley 1926). Since then, legal and illegal mining has been the reality of the area, bringing many problems that range from poor land and city planification, to criminal and illegal

activities. In the last 10 to 15 years, a big concern in the city and its surroundings is represented by land subsidence related to the combination of geology, morphology and mining activity (Cando et al., 2020). In fact, one of the principal triggers of this phenomenon is considered the presence of old/new legal/illegal galleries, shafts and other underground excavations. In this work, we have studied surficial deformations that occurred in the Zaruma historical center, between 2015 and 2019, in order to compare such deformations, on one hand, to known tunnel mining and, on the other, to detect possible locations of unknown tunnels. To pursue this aim, we used SENTINEL-1 image processing derived from the Europe Space Agency of the Copernicus Program. The work is structured as follows: first the mining activity at the Zaruma site is described, then a geological setting of the area is performed. A brief description of the data and the interferometric technique are carried out. Finally, the results are reported, and conclusions are drawn on the application made and possible future developments.

3.3. Zaruma Geological Setting and Mining Activity

The city of Zaruma or “Villa del Cerro del Oro de San Antonio de Zaruma” is located in southwestern Ecuador. The geology of the study area is characterized by pre-Mesozoic metamorphic rocks, which comprise the Amotape-Tahuin (Ta) massif in the south, and the Chaucha metamorphic and volcanic rocks in the north (Pilatasig et al., 2015) overlaid by younger volcanic rocks. In the Zaruma area, the basement, called the El Oro metamorphic complex, is covered by calc-alkaline volcanic materials of the Saraguro formation (FmSa) (Figure 3.1 a,b). The FmSa is widespread all over southern Ecuador, characterized by variable lithology, comprising andesitic and andesitic basalt lavas, highly weathered andesitic tuffs and dacitic tuffs, and ignimbrites (Litherland, 1994; Pratt et al.,1997).

The pyroclastic rocks range from fine-grained tobaceous to agglomerated (tuffs and thick agglomerates with blocks of lava) and alternating porphyritic andesite lavas (Baldock, 1982; Pratt et al., 1997; Vikentyev et al.,2005). Another lithology occurring within the study area is represented by the Zaruma Urcu Rhyolite (RZU), mostly consisting of dyke stocks and other forms of rhyolitic intrusions (Van Thournout et al., 1996). Small occurrences of metamorphosed gray sandstones, interspersed with limolites and dark gray shales, likely corresponding to the Paleozoic Ta, can be locally observed (Baldock, 1982; Vikentyev et al., 2005).

According to the results of geological and geotechnical studies, the predominant volcanic rocks in the study area are characterized by a high weathering degree, very intense surficial reworking ranging from poor to very poor quality. These characteristics notably increase terrain instability. The epithermal gold orebodies mined at Zaruma are genetically associated with calc-alkaline Eocene to Late Miocene igneous complexes occurring in central and southwestern Ecuador (Van Thournout et al., 1996). Mineralization within the area is considered to be an intermediate to low-sulphidation epithermal to a mesothermal gold-silver-lead-zinc-copper system (Hedenquist et al., 2000; Chiaradia et al., 2004). In the Portovelo-Zaruma area, the gold-bearing quartz vein system shows a north–south trend, characterized by sub-parallel structures exclusively located within the Cretaceous semi-high altered andesitic rocks. Three main types of gold-bearing veins are present in the study area (Figure 3.1c): the quartz-pyrite zone: quartz veins with disseminated pyrite, minor chlorite strikes, bands and patches; the sulphide zone: quartz veins with high pyrite, chalcopyrite, galena and sphalerite in bands, patches and coarse disseminations; and the calcite zone: carbonate veins with coarse calcite and calcite-quartz, galena, sphalerite and chlorite in occasional nodules (Billingsley, 1926; Litherland, 1994; Pratt et al., ; 1997). These metallogenetic features make the Zaruma area enhanced with several gold mineralization. The city is well known because of gold mining as most of the population works or lives nearby and is in contact with mining zones (González et al., 2017). The mining activity of Zaruma started during the 16th century because of the presence of gold veins and big quantities of gold in the rivers, and the city took the name of “Asiento de Minas de Zaruma”. Recently, the mining industry in Zaruma has gone through different phases. In the early 20th century, the mining activity was first controlled by the company SADCO and then by CIMA corporation, but also by individuals carrying out artisanal activity, following the main gold vein called “Sweet Water” (Murillo, 2000). Later on, a lot of people working in the gold exploration and exploitation in Zaruma independently built their houses, causing a disordered and accelerated growth of the urban area (González et al., 2017). Contextually to the licensed mining activity, widespread illegal gold exploitation all around the city area has been developed and many tunnels and galleries were built there. The uncontrolled mining increased the environmental and economic dangers in Zaruma. One of the most relevant infrastructure problems that

occurred in Zaruma is the collapse of the school, named “Inmaculada Fe y Alegria”, in 2017.

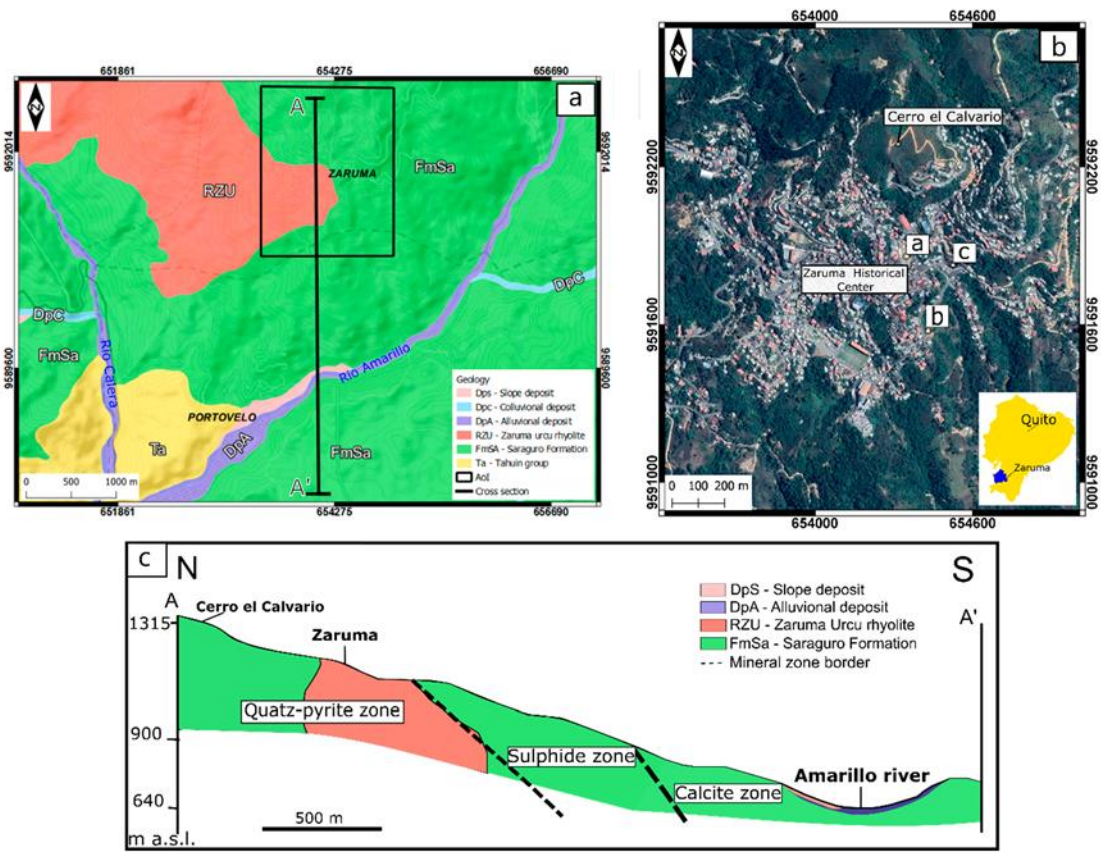


Figure 3.1. (a) Geological sketch map with Cross section (A–A’); (b) the study area with the location of pictures (a, b, c) in Figure 3.2; (c) Simplified cross-section of Portovelo-Zaruma field (modified from (Vikentyv et al., 2005)). Reference system: WGS84-UTM-17S.

The school collapsed into the ground after a big sinkhole episode (Figure 3.2a), and over the years other problems have occurred in the surrounding areas (Figure 3.2b,c). Most of the mentioned problems were related to illegal artisanal mining, carried out with low and poor technical standards and minimum control, along the old SADCO and CIMA galleries, which were built without any regulation



Figure 3.2. (a) Sinkhole near the school “Inmaculada Fe y Alegria” (GAD ZARUMA on Twitter); (b) subsidence in Zaruma (www.machalamovil.com);(c) tunnel under city patrimonial zone (www.elcomercio.com).

In order to manage problems of illegal mining that affect the cities of the El Oro province, the Ministry of Energy and Non-Renewable Natural Resources and the Risk Management Services (SGR) organized a plan called “Zaruma - Portovelo 2022” (www.controlminero.gob.ec). The project has several actions aimed at studying the deformation due to outlaw activity and restore the urban area. Among the first actions implemented by the SGR, geoelectrical surveys were carried out in the Zaruma historical center, which allowed a preliminary identification of some tunnels. Subsequently, other studies, carried out by the University of Cuenca Politecnica Salesiana, allowed to obtain an updated map of the tunnels (Ludizca et al., 2018) (Figure 3.3). It is worth to point out that these studies were certainly not exhaustive, as they were only limited to the historical part of the city.

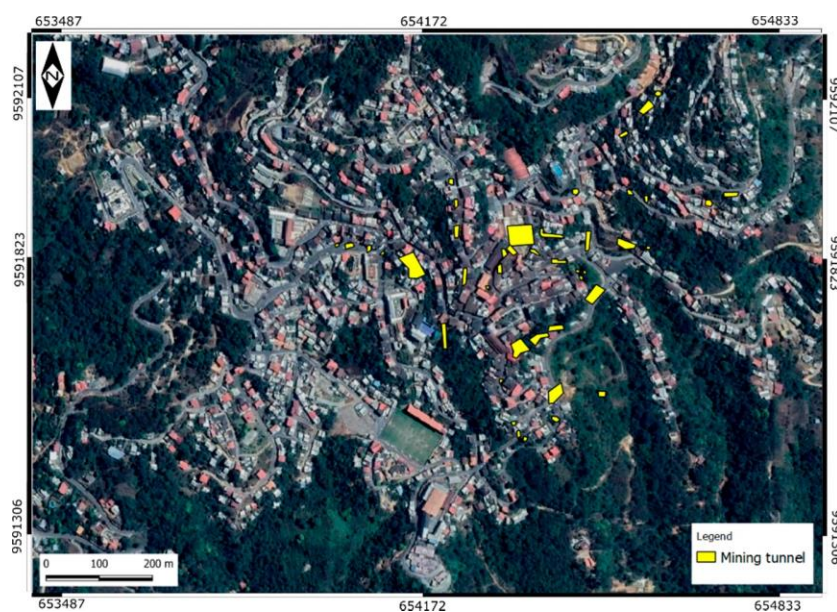


Figure 3.3. Mining tunnels in the Zaruma urban area (modified from (Ludizaca et al., 2018)).

3.4. Materials and Methods

It is now almost three decades (early 1990s) that the differential interferometry SAR technique (DInSAR) (Franceschetti et al. 1992) used for monitoring surface deformations has caught the attention of the scientific community. DInSAR, in fact, is a very effective technique for the accurate measurement of slow ground movements, structures and infrastructures due to subsidence, landslides, earthquakes and volcanic phenomena (Cigna et al., 2016; Pappalardo et al., 2018; Pastor et al., 2019; Pepe et al., 2019). By means of DInSAR, it is possible to measure ground displacements with sub-centimetric accuracy, starting from data acquired from satellites orbiting the earth at an average height of 600 km. The DInSAR approach is based on the analysis of phase difference in interferometric stacks of radar images: this technique operates at a full spatial resolution and identifies reliable scatterers (permanent scatterers—(Ferretti et al., 2001)) by measuring their multitemporal coherence related to the phase stability. In particular, DInSAR techniques allow to analyze long data series producing mean displacement rate maps and time series of deformations along the direction between the SAR sensor and the target (line of sights—LoS). In this work, TOPS IW Sentinel-1A and B ascending and descending mode images, obtained via the Sentinel Scientific Data Hub (ESA - www.scihub.copernicus.eu), acquired in the time span from June 2015 to June 2019 (Table 3.1), were processed by the SUBSOFT software, which uses the coherent pixel technique-temporal sublook coherence (CPT-TSC, more details in Appendix 1)

approach (Mora et al., 2003; Iglesias et al., 2015), and developed at the Remote Sensing Laboratory (RSLab) of the Universitat Politècnica de Catalunya of Barcelona.

Table 3.1. Synthetic aperture radar (SAR) data stacks analyzed in this study.

Satellite	Orbit	Period	Nr Scenes
Sentinel1 A/B	Ascending	17/01/2016–12/06/2019	89
Sentinel1 A/B	Descending	05/06/2015–23/09/2018	51

Specifically, the interferometric chain implemented in SUBSOFT is divided into the following main steps: the first is the generation and selection of interferograms, which consists of selecting a quality set of interferograms, considering the temporal and spatial thresholds, from all the possible combinations among available images. The second step is the pixel selection, named stable coherence scatterers (SCS—(Iglesias et al., 2015)), characterized by a reliable phase. In order to select SCS, a TSC estimator (Iglesias et al., 2015) has been used. The third one is the evaluation of the linear term of deformation to define the linear velocity and location of the targets; then the evaluation of the non-linear deformation component and atmospheric artifacts to assess the deformation evolution of selected pixels; and finally, the geocoding of the results in WGS84 and WGS84-UTM. Further details can be found in (Mora et al., 2003; Iglesias et al., 2015). After the processing step, the interferometric results were post-processed by the application of the kernel density estimation (KDE) algorithm (Silverman, 1986), which allowed to identify in a rapid way the unstable areas (UAs) affected by meaningful deformations (Lu et al., 2012; Bonì et al., 2016; Di Martire et al., 2016; Solari et al., 2018; Solari et al., 2019). Specifically, the “Heatmap” plugin in the Qgis software has been used. This creates a density map (heatmap) of an input point, using the following formula:

$$1) \quad KDE = \frac{1}{\text{Bandwidth}^2} \sum_{i=1}^n \left[\frac{3}{\pi} (w_i) \left(1 - \left(\frac{L_i}{\text{Bandwidth}} \right)^2 \right)^2 \right]$$

$$2) \quad \text{for } L_i < \text{Bandwidth}$$

where

- Bandwidth is the radius;

- w_i is the weight;
- L_i is the distance between point i and the (x, y) location.

The density is a function of the number of points, or the sum of the weight parameter. In fact, the use of this parameter allows to increase the influence that some points have on the resulting density map. In this study, the mean displacement rate is considered as a weight parameter. Heatmaps allow quick identification of “hotspots” of points. As for the kernel map, the first feature to set is the choice of bandwidth or the search radius. The bandwidth controls the smoothing of the results, larger values result in greater density, but smaller values may show finer details. Therefore, it is important to estimate the bandwidth starting from the presence data available in order to use the best radius value. In order to calculate the best radius that must be used in the kernel density, the formula of Silverman, 1986, has been adopted:

$$Bandwidth = 0.9 \times \min (SD, \sqrt{\frac{1}{\ln(2)} \times D_m}) \times n^{-0.2}$$

$$*SD = \sqrt{\frac{\sum_{i=1}^n w_i (y_i - X_w)^2}{\sum_{i=1}^n w_i} + \frac{\sum_{i=1}^n w_i (y_i - Y_w)^2}{\sum_{i=1}^n w_i}}$$

Where

- in is the minimum value between the two in the interlude;
- SD is the standard distance;
- D_m is the (weighted) median distance from (weighted) the mean center;
- n is the number of points;
- x_i, y_i are the coordinates;
- w_i is the weight.

The radius was calculated using Qgis tools: in detail, the centroid was considered through the Mean Coordinate tool and then the Raster Calculator was used to estimate the bandwidth for each satellite geometry. The values obtained were inserted in the Heatmap tool and the mean displacement rate as the weight field has been used (w_i) to increase the quality of the results.

Finally, thanks to the availability of images acquired in the two ascending and descending geometries, it has been possible to obtain the vertical (Z) and E–W

components of the displacements. This operation is possible (system resolution of 2 equations in 2 unknowns (Equation (5)) under the hypothesis that the motion component in the north–south direction is negligible (Colesanti et al., 2006; Cascini et al., 2010). This is an intrinsic limit of the acquisition system, since the north–south motion component is strongly underestimated since the SAR sensor’s direction of view is almost orthogonal to the north–south direction (the satellite travels along quasi-polar orbits with antennae oriented orthogonally to the flight direction) and is therefore not very sensitive to variations in this direction.

$$5. \quad D_a = D_x S_{xasc} \times D_y S_{yasc} \times D_z S_{zasc}$$

$$D_d = D_x S_{xdesc} \times D_y S_{ydesc} \times D_z S_{zdesc}$$

where D_a and D_d are, respectively, the displacement values in ascending and descending geometry, D_h and D_v are the displacement vector components along the horizontal (E–W) and vertical directions and S_{xasc} , S_{yasc} , S_{zasc} , S_{xdesc} , S_{ydesc} , and S_{zdesc} are the incidence angles in the two geometries.

3.5. Results

The datasets available from this study consist of 89 images acquired in ascending geometry with a time-revisiting variable between 12 and 36 days in the time span January 2016–June 2019, and 51 images acquired in descending geometry with a time-revisiting variable between 12 and 96 days in the time interval June 2015–September 2018. From all possible pairs of interferograms, only those characterized by spatial and temporal baseline thresholds of 50 m and 150 days, respectively, have been selected. In particular, 793 and 271 interferograms in ascending and descending orbits, respectively, have been identified (Figure 3.4).

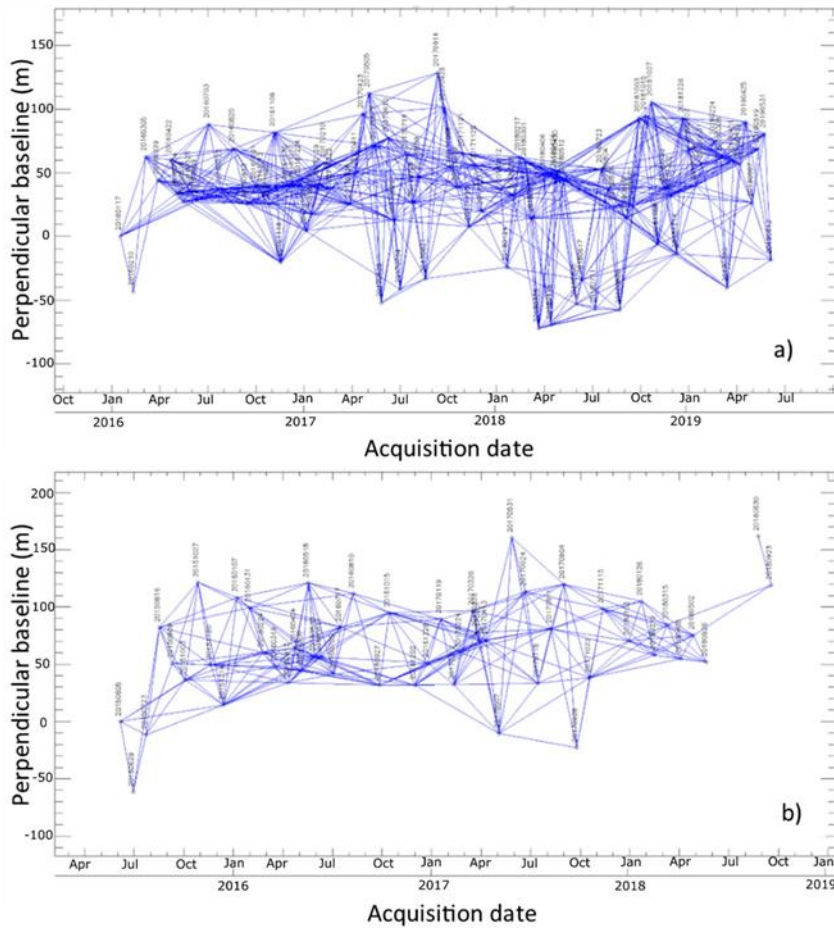


Figure 3.4. Interferograms distribution in (a) ascending; (b) descending.

The following step consisted of SCS selection. CPT-TSC allowed to select points in the detected area characterized by a phase quality higher than a threshold value set by the operator according to the error in the displacement evaluation considered acceptable (in this case less than 1.5 mm), which in turn is a function of the expected mean displacement rate. In this case, a TSC value equal to 0.65 has been set in both geometries (Figure 3.5) in order to obtain an acceptable displacement error, lower

than 1.5 mm, and to select an adequate number of points. Using the CPT-TSC approach, two mean displacement rate maps have been obtained, each for both acquisition geometries. In the El Oro province territory about twenty and twenty-one thousand targets (ascending and descending) located in the Portovelo, Piñas and Zaruma districts have been detected. Specifically, in the Zaruma town, about 4000 and 5200 targets have been detected, in ascending and descending orbits, respectively. The results allowed to evaluate the surface ground displacements in terms of mean displacement rate and time series of deformation along the LoS of the satellite. Figure 3.6 shows the mean displacement rate in terms of cm/year recorded in the time span 2015–2019. The maps have been represented using a color scale from red to blue, where the negative values conventionally indicate a movement of the target towards the satellite, while the positive values indicate movement far from the sensor, and the green color identifies stable areas.

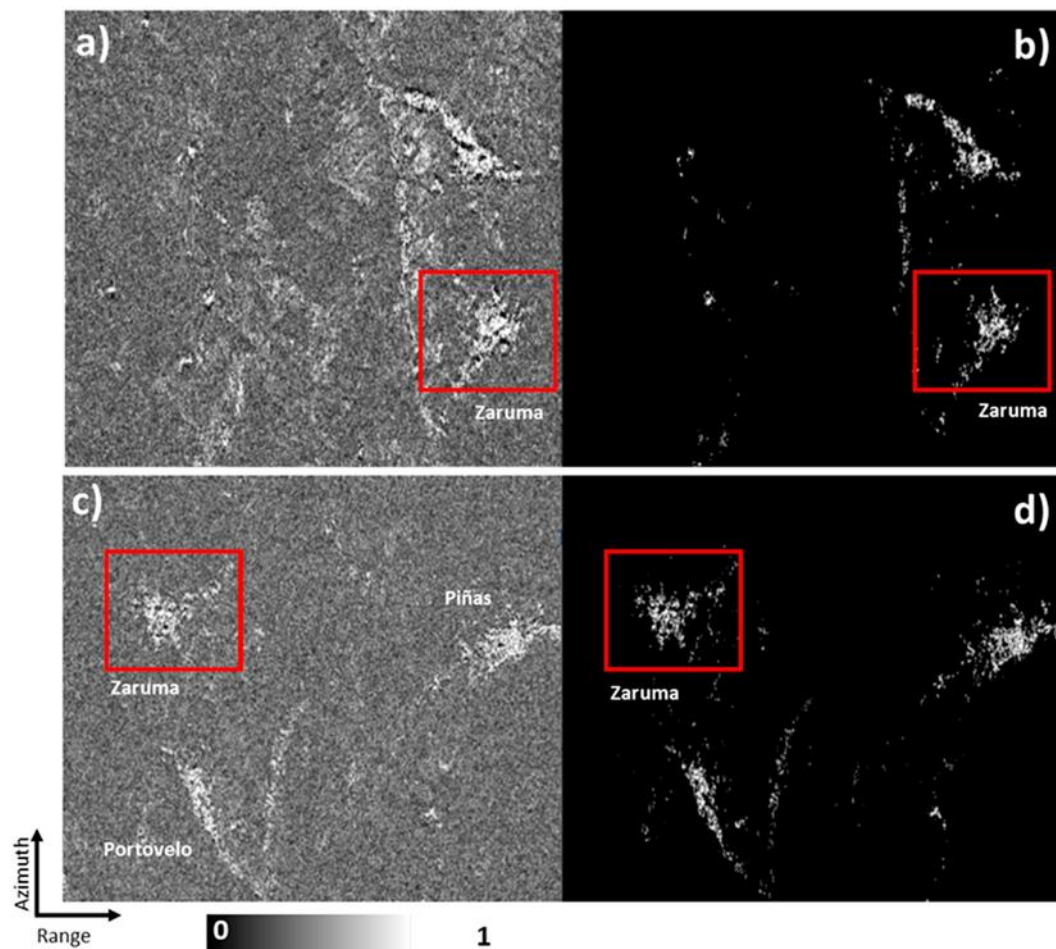


Figure 3.5. Temporal sublook coherence maps: ascending (a), and (c). Stable coherence scatterers (SCS) maps: (b) ascending, (d) descending.

In order to identify the displacement rate threshold for which areas should be considered stable, a coefficient of variation, given by the ratio between the standard deviation and the velocity average module, for all selected SCS, has been evaluated. The threshold value obtained is about 0.3 cm/year, corresponding to a value for which standard deviation is higher than the mean displacement rate value (Colesanti et al., 2006). To detect the presence of UAs in the urban area of Zaruma, the KDE algorithm was applied to both analyzed datasets (Figure 3.7). Such a figure shows the hotmaps in the area of the Zaruma historical center displaying the density of targets weighted on mean displacement rate values during the covering period for each satellite orbit. Both blue and red hotmaps highlight where surface deformations are present. As already described above, the color blue indicates movements far from the satellite, while red movements are towards the satellite. Moreover, the intensity of the color gives information on the magnitude of the deformations, while the radius indicates the potential extension of the phenomenon.

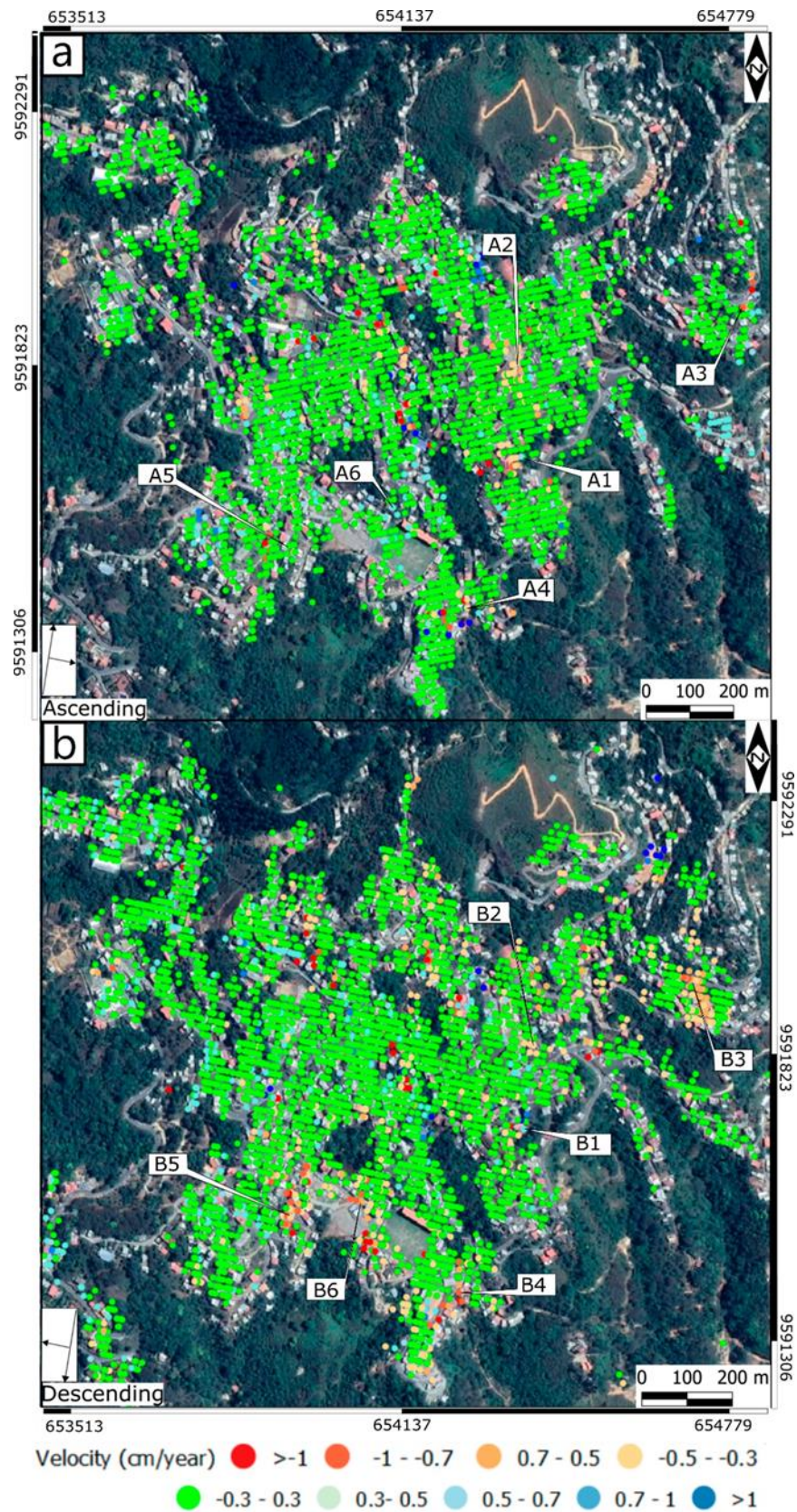


Figure 3.6. Mean displacement rate map: (a) ascending orbit; (b) descending orbit. A1–6 and D1–6, ascending and descending, respectively, are points for which vertical and horizontal components have been calculated (see Discussion section).

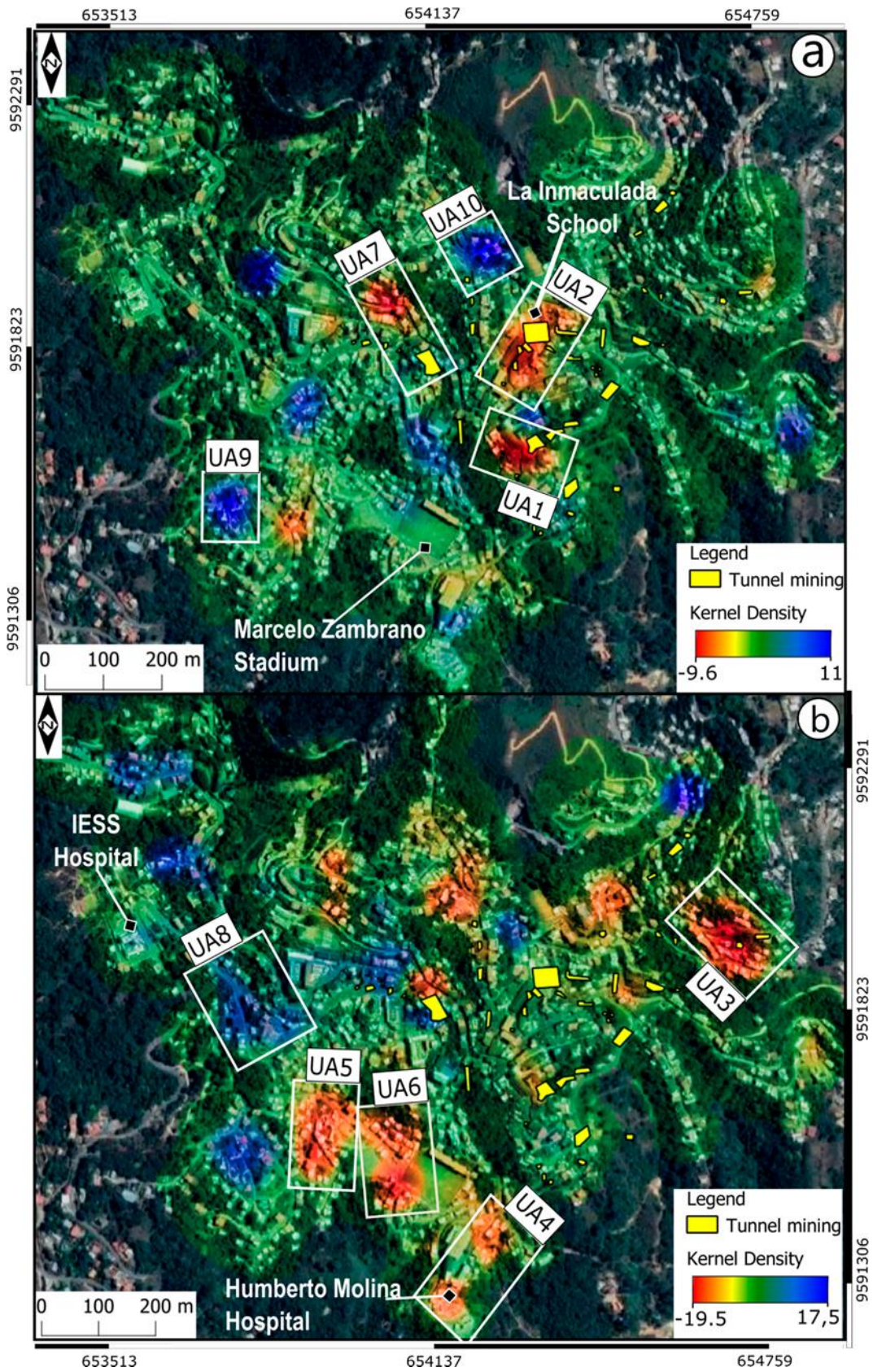


Figure 3.7. Kernel density map: (a) ascending orbits; (b) descending orbits.

In detail, the detected UAs are distributed as reported in Table 3.2: (a) south of the Inmaculada school (UA1), where displacement rates of about 3 cm/year have been recorded and where tunnels are known; (b) around the school (UA2), which collapsed in 2017, where significant deformation rates can still be observed (about 1 cm/year). It is worth to point out that probably higher displacements affected the school during the 2017 event. Such displacements were not detected, related to their extreme rapidity in a short time span, not allowing the interferometric technique to detect a coherent signal because of its inability to analyze such rapid deformations (Colesanti et al., 2006). Meanwhile, it was possible to verify that the subsidence phenomenon affecting the area was already in place before the collapse; (c) on the eastern hill of the inhabited center (Mirador La Colina—UA3), with mean displacement rates of the order of 1 cm/year, where tunnels have been mapped; (d) UA4 has been identified to the south, in correspondence of the Humberto Molina Hospital with rates of the order of 1 cm/year. In this case, due to the absence of known tunnels and the morphology of the site, these displacement rates could be caused by landslides (rotational slide) which affect the slope or subsidence induced by the presence of lawless activities; (e) as for UA4 and the UA5, located on the west side of the Marcelo Zambrano Stadium, they can be associated with a landslide phenomenon (rotational slide), due to the presence of a steepness slope or lawless activities; (f) UA6, located in correspondence of the Marcelo Zambrano Stadium, is characterized by null slopes, and by the absence of reported tunnels. Therefore, these peculiarities lead to the interpretation of recorded deformation rates due to the presence of illegal activities; and finally, (g) UAs 7 and 10, in the northern sector of the town and UAs 8 and 9, in the westernmost sector of Zaruma (near the IESS Hospital), showed mean displacement rates of the order of 1–2 cm/year, even though there are no tunnels in the official inventory. It was not possible to validate the results by comparing them with in situ measurements, due to the absence of the latter, but only by consulting several newspaper articles and scientific papers (Cando et al., 2020; www.twitter.com/gadzaruma; www.machamovil.com; www.elcommercio.com; Ludizaca et al., 2018).

Table 3.2. List of unstable areas (UAs) and probable cause of the observed SAR displacement rates.

Unstable Area	Probable Cause
UA1	Reported tunnels
UA2	Reported tunnels
UA3	Reported tunnels
UA4	Unknown tunnels/Landslide
UA5	Unknown tunnels/Landslide
UA6	Unknown tunnels
UA7	Reported and unknown tunnels
UA8	Unknown tunnels
UA9	Unknown tunnels
UA10	Unknown tunnels

Finally, a comparison between UAs and reported mining tunnels have been carried out, highlighting that out among the 10 UAs identified, 40% of these have at least one tunnel mapped in the official inventory, while for the remaining 60% there are no reported tunnels, so the presence of lawless activities could be assumed.

3.6. Discussion

The results obtained in this work have, on the one hand, confirmed the phenomena of instability, induced by the presence of underground activities, legal and illegal, which affect a large part of the urban center of Zaruma, and on the other, highlighted the need to implement a deformation monitoring system in order to mitigate the risks present. Actually, the aim of this paper was to evaluate the capability of Sentinel-1 data to detect and characterize the possible deformations due to mining activity. The processing of interferometric data by means of the DInSAR technique and the subsequent interpretation (kernel density) allowed to identify unstable areas (UAs) affected by subsidence and other gravitational phenomena. The use of the interferometric technique to monitor mining areas affected by subsidence phenomena which induce damage to structures has been carried out in several works. Many papers focus on areas where mining activities are known and often where in situ monitoring systems are implemented (Pawluszek et al., 2020). The most complex situation is that of unauthorized mining areas. In this case, the main purpose is the identification of areas potentially subject to subsidence and then the deformation rate. An example is a recent work (Cando et al., 2020), implemented in Zaruma, where the authors, by processing a limited number of images only in ascending orbit, have identified potential unstable areas, for an extension of about 40% of the urban center, but without evaluating their temporal evolution. Unlike what (Cando et al., 2020)

carried out, in this work, the images in both acquisition geometries (ascending and descending) were processed for a longer time interval (2015–2019). Moreover, a post-processing phase, using the kernel density algorithm, has been implemented, in order to identify about 0.45 km² of unstable areas. Finally, thanks to the availability of ascending and descending results, the time series of deformations of horizontal and vertical components have been obtained using the selected points reported in Figure 3.6. Within all the UAs identified, six have been selected, based on the highest values of displacement rates, which can be divided into three categories (reported, unknown tunnels and landslides) as shown in Table 3.2. In order to reconstruct the kinematic of the deformation, vertical and horizontal components have been calculated (Table 3.3) by means of the composition of ascending and descending data for the time span when both acquisitions were present (from January 2016 to September 2018) (Figure 3.8).

Table 3.3. Line of sights (LoS), vertical and horizontal displacement components for ascending and descending orbits. (Incident angle: 34° ascending; 43° descending).

	D_{LoS} Ascending (cm)	D_{LoS} Descending (cm)	D_{vertical} (cm)	D_{horizontal} (cm)
UA1	5.0	3.0	4.0	2.0
UA2	2.5	2.0	2.0	0.2
UA3	3.0	2.0	2.5	0.5
UA4	3.5	6.0	6.0	3.0
UA5	2.0	2.5	2.5	0.2
UA6	1.5	2.5	2.5	1.5

Specifically, the cumulated LoS displacements for the A1/D1, A2/D2 and A3/D3 are about 5.0/–3.0, 2.5/2.0 and 2.5/2.0 cm. The composition of the ascending and descending data made it possible to evaluate the horizontal and vertical components, highlighting in all three cases how the vertical component is always the predominant one, varying between 2.0 and 4.0 cm. This result, combined with the morphology of the sites (flat areas), allows us to state that a subsidence phenomenon is taking place in the area. Moreover, as far as UA2 concerns where the “Inmaculada Fe y Alegria” school was located, it is possible to highlight that the subsidence was already active before the event occurred in 2017 and nowadays it seems to move southward (Mojeron et al., 2019). In the second categories, UA4 and UA5, cumulated LoS displacements are about 3.5 and 2.0 cm in ascending and 6.0 and 2.5 cm for the descending orbit, respectively. Therefore, as previously done, the horizontal and

vertical components have been calculated (Table 3.3). In this case, the vertical components recorded higher values than the horizontal ones, varying between 2.5 and 6.0 cm, but unlike the first three UAs, it can be assumed that rotational landslides are taking place, due to the morphology of the sites (steep slopes). These results are also confirmed by ARCOM (www.elcomercio.com), which reported an increase in damage to structures in the area after the 2017 earthquake.

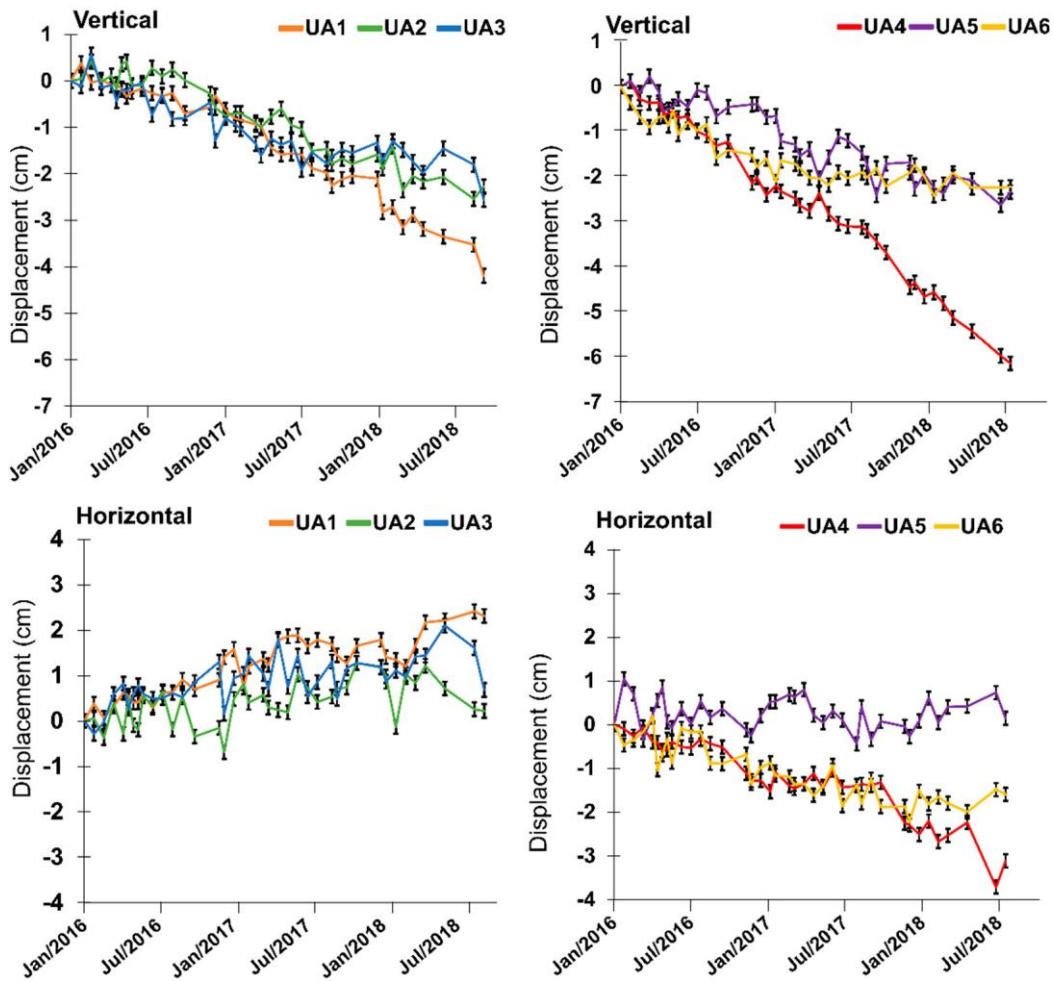


Figure 3.8. The time series of cumulated vertical and horizontal components. Displacement standard deviation, for each differential interferometric synthetic aperture radar (DInSAR) measurement, are also reported (black).

Finally, in the last category (UA6), displacements along the LoS of about 1.5 cm in ascending and 2.5 cm in descending, respectively, were recorded. In this case, the vertical component was higher than the horizontal one (Table 3.3), 2.5 with respect to 1.5 cm, confirming the subsidence phenomenon of the area, even in the absence of reported tunnels.

3.7. Conclusions

The Zaruma town has been known for ages for gold mineralization and for its mining activity which were considered the main sources of the country economy from the beginning of the 20th century. The activity was divided between small mining concessions released to private local miners, as well as to a few foreign companies. However, simultaneously with the licensed mining activity, a widespread illegal gold exploitation also developed in areas outside the allowed concessions. The forbidden mining area created in 1992, covering 0.7 Km² of the Zaruma urban area, recently has been expanded to 1.73 Km² due to the development of illegal mining activity.

Nowadays, numerous subsidence events occurred in the city, sometimes caused by the mining activities, as the sinkhole generated near the “La Immaculada de fe y alegría” school. Ecuador’s Agency for Mining Control and Regulation (ARCOM) detected in the country about 65 km of tunnel mining, where an unquantified number of illegal miners work, and open, new mines beneath from about 10 to 20 m (www.controlminero.gob.ec) have been reported. Considering the extension of the underground tunnels, it is difficult to carry out internal controls. According to the Undersecretary of Zaruma Risk Management, the ground surface vulnerability is probably due either to the illegal underground mining or to incorrect urban planning (www.elcomercio.com).

Thus, it is essential not to underestimate the potential effects of ground surface displacements and it is useful to monitor these to minimize negative environmental and social impacts. Several studies affirmed that in order to decrease the damage due to anthropogenic subsidence phenomena, it is important to identify and to map them (Sunwoo et al., 2010; Taheri et al., 2019). Recently, the management of terrain deformation has increased in importance and several monitoring techniques have been implemented, among which is the differential interferometric synthetic aperture radar (DInSAR) technique.

The DInSAR technique has proved effective in identifying areas subject to subsidence in the Zaruma town, making it possible to recognize critical zones both in areas where the presence of tunnels is known, but especially in those areas where tunnels have never been identified. The latter, which represent a serious problem for the city of Zaruma, as highlighted by several newspaper articles and as the intervention of the Ecuadorian authorities testified, was the main goal and novelty of

this work. This result will certainly be very useful to forecast the occurrence of events such as the one recorded in 2017 in the “La Immaculada de fe y alegría” school and in order to help the authorities that have to manage the territory through the identification of the most appropriate risk mitigation actions.

Finally, this result has a double value: on one hand, it will be possible to keep the ground deformation rates under control, in correspondence to the already known tunnels, by carrying out continuous monitoring and integrating it with in situ measurements, thanks to the availability of images of the SENTINEL-1 constellation which have a revisiting time of 12 days; on the other hand, it will be possible to carry out a validation through field detection by focusing attention directly on the areas where anomalous displacement rates have been identified, but where, up to now, there is no certainty of the presence of reported tunnels. Updating the tunnel map, by means of the integration of remote sensing and fields surveys, will therefore be fundamental to subsequently carry out a sinkhole hazard study (Pellicani et al., 2017; Parise et al., 2013; Ardau et al., 2007; Intrietti et al., 2018; Todd et al., 2020;), which will allow the authorities in charge of land management to implement risk mitigation actions.

4. Semi-real time systems for subsidence monitoring in areas affected by underground mining: the example of the Nuraxi-Figus coal district (Sardinia, Italy)

4.1. Abstract

Underground mining can produce subsidence, which can be coincident with mining activities or delayed in response to the time-dependent deformation of the rocks. Therefore, in these cases, it is essential to effectively monitoring the soils deformations at different times during and after mining activity. In the present work, an integrated approach based on geotechnical numerical modeling and Advanced Differential Interferometric Synthetic Aperture Radar (A-DInSAR) method was applied to detect, study and monitor the subsidence related to mining activity in the Nuraxi Figus coal district (Sardinia, Italy). Two datasets of high-resolution COSMO-SkyMed (CSK) images were acquired, respectively in two covering periods: from 2011 and 2014, and from 2013 to 2020. The A-DInSAR results show that the predominant displacement rates are located in correspondence with the panels. The cumulated satellite-based LoS displacements vary in the first period between -130 and $+28$ mm and -293 and $+28.4$ mm, while, during the second period between -6.9 and $+1.6$ mm and -8.72 and $+4.33$ mm in ascending and descending geometries, respectively. The geotechnical numerical model allowed to obtain a ground displacement threshold. By using the vertical and horizontal components it was possible to reconstruct the kinematics of the deformation considering three phases: pre-mining, syn-mining activity, and post-mining activity. The temporal evolution of displacements started during the mining extraction in 2011, achieved the major values in correspondence of post-mining operations, during the period 2013 to 2014 and continued slowly until 2020. The near real-time monitoring system applied in this study proved to be very useful for detecting subsidence during the mining activity and in the post-mining period.

4.2. Introduction

Mining and mineral extraction is useful for human development, social progression, and material prosperity. However, these activities strongly interact with surrounding environments and could produce significant negative effects, on atmosphere, soil, and water (Bell et al., 2000). One of the main issues in many parts of the world is represented by the subsidence induced by underground mining (Villegas et al., 2011, Zhou et al., 2015, Przyłucka M. et al., 2015, Vu Khac et al., 2021). Such effects are more harmful when the activities legal or not authorized are in correspondence or nearby urban areas (Bell et al. 2005, Prakash et al. 2010, Ji et al. 2011, Villegas et al. 2011, Marschalko et al. 2012). Subsidence can either coincide with mining activities or be delayed in response to the time-dependent deformation of rocks. Several studies determined the rate of expected subsidence by means of physical or numerical modeling and analysis (Whittaker 1989, Singh et al. 1998, Al Heib et al. 2001, Ye et al. 2016, Xie et al. 2020, Gazzola et al. 2021). In any case, to avoid possible environmental harms it is important monitoring areas subjected to underground mining activity. Mining-related subsidence can be analyzed with piezometers, useful to register pore pressure variations of the overburden strata (Guo et al. 2012). Monitoring can be also conducted by using extensometers installed at different heights in boreholes located above the exploited panels: in this way, displacements are measured (Holla et al. 2000). In addition to the above-mentioned conventional survey methods, remote sensing can be a convenient technique. Specifically, among the different types of remote sensing techniques, the Advanced Differential Interferometric Synthetic Aperture Radar (A-DInSAR – Franceschetti et al., 1992) proved to be a very powerful tool, being sensitive to sub-centimetric ground movements (Colesanti et al., 2006) and/or terrain displacements, induced by landslides (Wasowski and Bovenga 2022, Scifoni et al., 2016, Pappalardo et al., 2018, Giardina et al., 2019, Guerriero et al., 2019), earthquakes (De Novellis et al., 2018, Zhao et al., 2021), volcanoes (Foumelis et al., 2016, Casu et al., 2019) and valid to detect harms to structures and infrastructures (Milillo et al., 2018, Ullo et al., 2019, Pastor et al., 2019, Miano et al., 2021). In the last three decades, A-DinSAR has been applied also in mining areas to detect the subsidence due to underground activity (Yue et al., 2011, Du et al. 2016, Ammirati et al., 2020, Pawluszek et al., 2020, Chen et al. 2021), monitoring the stability of tailings dam (Necsoiu et al., 2015, Gama et al., 2019, Ammirati et al., 2021), and to identify surface movements in open-

pit mines (Paradella et al., 2015, Carlà et al., 2018). The scientific community has studied many cases of mining subsidence in coal districts (Salmi et al., 2017, Jing et al., 2018, Zingano et al., 2019). In these areas, A-DinSAR resulted to be an effective technique for ground movement survey (Dong et al., 2013, Xu et al., 2020). In several studies, the subsidence maps generated from satellite images proved to be consistent with field observations (Ismaya et al., 2012, Samsonov et al., 2013, Pawluszek et al., 2020). In this work, an integrated approach based on geotechnical numerical modelling and A-DInSAR method was applied for investigating subsidence phenomena occurred in a coal mining area interested by underground exploitation. The study area is represented by an historic coal mining district located in south-west Sardinia, Italy, in the municipality of Nuraxi Figus (Carbonia-Iglesias province). The study area occurs in the Carbosulcis S.p.A. mining concession called “Monte Sinni” (total extension of about 0.6 Km²), where a subsidence phenomenon occurred between the years 2011 to 2014 (Tessitore et al., 2018). In the present study we analyzed the remote sensing data to correlate the 2011-2014 subsidence phenomenon with the underground mining activity and the excavation development, also using numerical modeling to reconstruct the kinematic evolution of ground displacements. Moreover, radar satellite data, derived from COSMO-SkyMed (CSK) datasets, were acquired and processed by SUBSIDENCE software, which implements the Coherent Pixels Technique algorithm (Mora et al., 2003, Iglesias et al., 2015), for the period from 2013 to 2020, to understand the temporal evolution of ground surface deformation. The study allowed to understand the cause-effect mechanism between extraction and ground deformation and confirmed that ground surface deformations can continue at lower rates a few years after completion of mining activities.

4.3. History of the mining activity in the Sulcis coal basin

In the Sulcis coal district, the mining activity started around 1850 through the exploitation of productive coal outcrops occurring in the sedimentary rocks of the Lignifero Formation (Figure 4.1). During this period, the coal became the primary national resource and was mostly exploited in open-pits. In the Sulcis district, the underground mining activity started in 1950 in association with increasing economic necessities of the country and thanks to the discovery of new exploitation techniques. In 1956, the coal exploitation started in the underground Seruci mine, located in center of Sulcis basin.

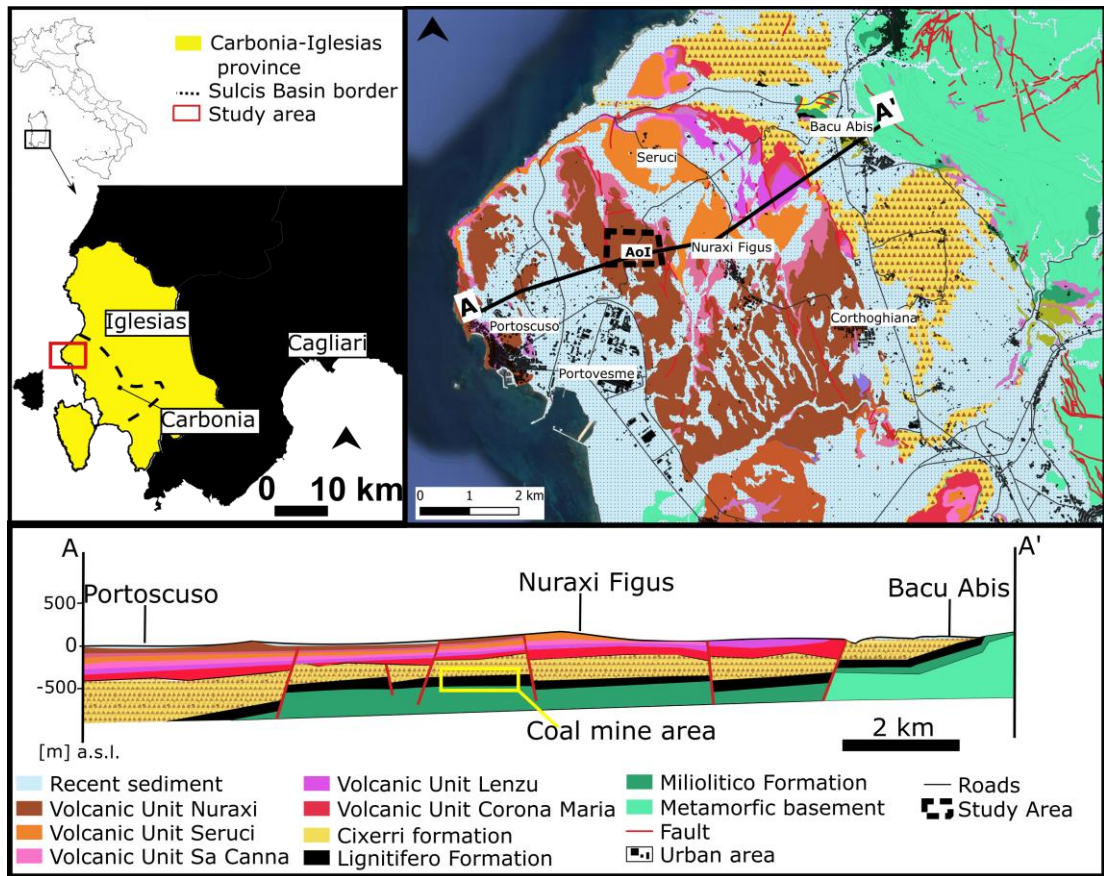


Figure 4.1. Study area red box. Geological sketch map on right. Below the geological cross-section

At that time, the Seruci mine represented one of the most advanced and modern mines in Europe, exploiting coal seams occurring at a depth between 200 to 500 m below ground level. Since 1976, Carbosulcis S.p.A., which is the current owner of the mining licenses in the Sulcis district, started mining activity south of Seruci, in the Monte Sinni area, nearby the Nuraxi Figus village (Fadda et al. 1994). The Monte Sinni coal panels are located at a depth of about 400 m b.g.l., extend for an area of 55 km² and are mined through 30 km of tunnels (15 km of which correspond to permanent infrastructures). Mining activity was conducted in correspondence of some exploitation panels, called W1, W2, W3, etc., with average dimensions of 300 m x 600 m (width x length) and a height of about 3 m. In the initial period of activity, mining was developed through room and pillars method, whereas from the 1980s coal extraction was carried out with a different method, called “longwall cutting in retreat”. The latter is based on the continuous extraction of the coal panel by means of a shearer that digs along the coal face, while a transporter belt carries away the grained coal. When the shearer moves on, the roof of the gallery at the back of the active face collapses. The Carbosulcis S.p.A. used the longwall method to extract the W3 and W4 panels, in the periods between from 2008 to 2010 and from 2011 to

2012, respectively. In 2018, following the progress of environmental regulations on the cessation of the use of coal, the Company started the closure plan that progressively will bring to reclaim all the areas by 2027 (Figure 4.2).

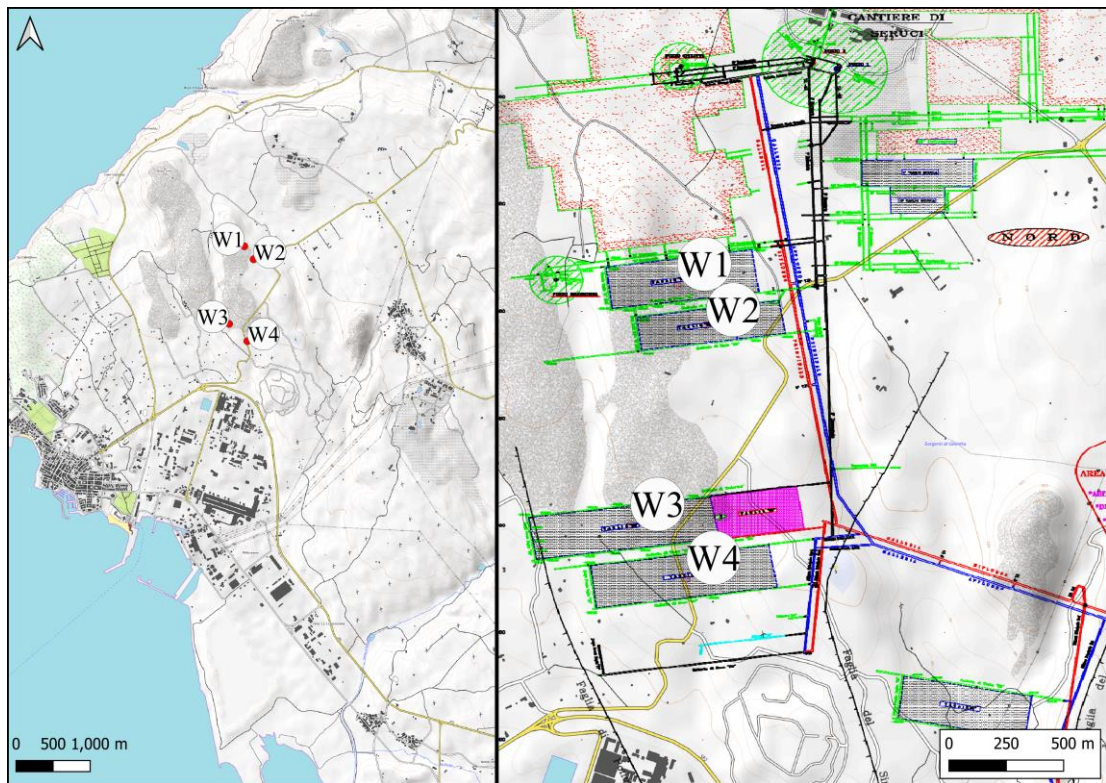


Figure 4.2. Location of exploitation panels, W1, W2, W3, W4. On right the maps of underground tunnels and excavation areas.

4.4. Geology of the Sulcis district

Geology of the Sulcis district is characterized by Cenozoic sedimentary and volcanic rocks, unconformably overlaying a Paleozoic basement. The Cenozoic sedimentary rocks, deposited in extensional basins, which were filled by a sedimentary succession consisting of limestones, sandstones, conglomerates, marls, and silty clays, have been subdivided in four stratigraphic formations. Proceeding from the bottom of the Cenozoic succession, the oldest rocks are represented by the limestones of the Macroforaminifera Formation, which are covered by the sandstones, marls and limestones of the Miliolitico Formation (20–70 m thick; Lower Eocene age). The following stratigraphic interval is represented by clays, marly limestones, bituminous limestones, marls, and conglomerates of the Lignitifero Formation (70–150 m thick; Lower-Middle Eocene age). This formation hosts various coal horizons. Coal seams commonly are 10 cm thick, rarely reaching 30–50 cm, and are interbedded with clays (Assorgia et al. 1992a and b). The Lignitifero Formation is covered by about 300 meters of sandstones, conglomerates, and marls of the Cixerri Formation (Eocene-

Oligocene; Pasci et al. 2012). This sedimentary succession is in turn covered by volcanic rocks, represented by twelve andesitic, dacitic to rhyolitic ignimbrite plateaus belonging to several stages of explosive volcanic activity of Oligo-Miocene age (Morra et al., 1994). The distinct plateaus are separated by paleosoils, indicating periods of volcanic inactivity (Assorgia et al., 1990), which allow recognition of the twelve units (Assorgia et al. 1992a and b). The youngest unit, called Nuraxi ignimbrite (NU), has an average thickness of 20 m and covers as a mantle most of the study area. The whole district has been dislocated by normal faults, which lower the sedimentary succession to various hundred meters of depths within the basin (Barca et al. 2000). These geological features allow the existence in the area of two types of aquifers: one occurring in the volcanic rocks and a second one in the Miliolitico Formation, which have been both dewatered by Carbosulcis S.p.A. before the start of the underground mining activity. From a geotechnical point of view, the Rock Mass Rating (RMR) (Bieniawski 1989) was used to numerically define the characteristics of the rocks, by means of "RMR value" which allows defining five quality classes (from very poor to very good). In particular, 89% of the volcanic rocks correspond to the fair class (III), whereas the sedimentary Formations are characterized by 57% to the fair class (III), 28% to the poor class (IV) and 10% to the good class (II) (Fadda et al. 1994). Such geotechnical features evidence that the Cixerri Formation has a heterogeneous structure, where conglomerate and marls layers belong to the lowest classes, while sandstones are characterized by the best performance.

4.5. Materials and methods

For the present study, as summarized in the flow chart of Figure 4.3, satellite data and mining information were used to create a near-real time monitoring system. Satellite data were collected in ascending and descending orbits covering the time span 2011-2020, to study subsidence by the vertical deformation maps and the displacement time series. Two datasets composed of the high-resolution COSMO-SkyMed (CSK) images have been used and two distinct A-DInSAR algorithms were applied to the CSK in two periods of time:

- Satellite data 1 (SD1): PSP-IFSAR algorithm (Costantini et al., 2008), time span 2011-2014, obtained in the framework of Not-Ordinary Plan of Environmental Remote Sensing (Piano Straordinario di Telerilevamento Ambientale – in italian),

funded by the Italian Ministry of Environment (Costantini et al., 2017, Di Martire et al., 2017).

- Satellite data 2 (SD2): SUBSIDENCE software (Mora et al., 2003; Iglesias et al., 2015), covering the period 2013 – 2020.

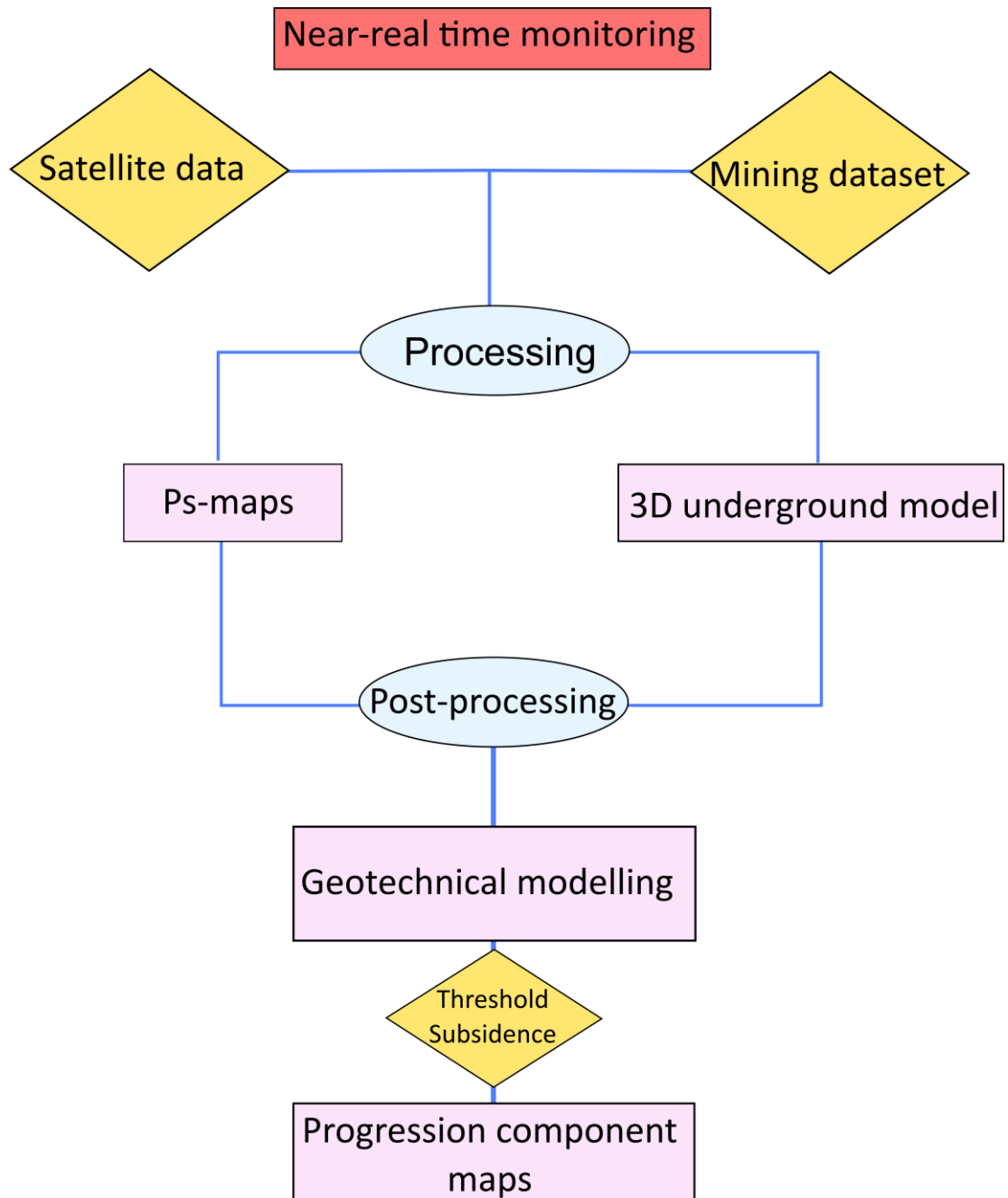


Figure 4.3. Materials and methods summarized in the flow chart.

SD1 consist of 41 images acquired in ascending geometry and 58 images acquired in descending geometry in the time interval May 2011– March 2014. SD2 contain 102 and 116 images in ascending and descending orbit, respectively related to the time span October 2013 to July 2020. First data set derived from the interferometric

processing within the framework of the third stage of the PST-A project (Not-Ordinary Plan of Environmental Remote Sensing) funded by the Ministry for the Environment and Protection of the Territory and the Sea (Italian National Geoportal, www.pcn.minambiente.it). The second dataset was obtained by the processing of SD2 by means of SUBSIDENCE software, which implements the Coherent Pixels Technique (CPT) algorithm, developed at the Remote Sensing Laboratory (RSLab) of the Universitat Politècnica de Catalunya of Barcelona. SUBSIDENCE uses the CPT-Temporal Phase Coherence (CPT-TPC) approach to extract from a stack of differential interferograms the deformation evolution over wide areas during large time spans (Mora et al., 2003, Iglesias et al., 2015). The processing is structured in three main phases:

- 1) Interferogram generation: the generation of the best interferogram set among all the available images of the zone under study;
- 2) The Stable Coherence Scatterers (SCS) selection: the points in the detected area characterized by signal stability and higher than the threshold in a specific percentage of interferograms. To get enough SCS's a coherence limit of 0.6 was considered, assuming an error in mean displacement rate lower than 1.5 mm;
- 3) Linear velocity of deformation (Iglesias et al., 2015): linear deformation time series (TS) were calculated starting from phase analysis. The Delaunay triangulation was used to check an offset among the different interferograms. Then, it was applied a filtering process to assess the deformation evolution of selected pixels (SCS) (Blanco et al., 2008); the geocoding of the results was carried out in WGS84-UTM.

This process allowed to elaborate PS (Permanent Scatterers) maps for each acquisition geometry in terms of mean displacement rate and time series of deformation, along the Line of Sight (LoS) of the satellite. After this, by using images acquired in ascending and descending geometries the vertical displacement component was calculated (Cascini et al., 2010; Di Martire et al., 2013). Subsequently, to improve the analysis of the Nuraxi Figus subsidence, satellite datasets were integrated with the following information, provided by Carbosulcis S.p.A.: stratigraphic logs of 9 drillholes, geotechnical parameters of country rocks, mining reports regarding the exploitation of panels W3 and W4, and maps of underground tunnels and excavation areas. Spatial migration in time of the excavation front within the mining panels W3 and W4 was compared with the evolution of vertical ground displacements detected

with the satellite data during the mining activity. The 3D geological model of subsurface was elaborated by using lithostratigraphic data from 7 boreholes through the software Rockworks® (Figure 4.4). The model allowed to determine the thickness of the overburden strata in the various parts of the study area. A stratigraphic section perpendicular to the W3 and W4 exploitation panels was extracted from the 3D geological model to produce a numerical subsoil model through the Plaxis® 2D software (Brinkgreve et al., 2008). The finite element numerical model allowed to model the excavation process in two-dimensions in order to quantify the subsidence induced at surface level. The characteristic values of geotechnical rock parameters used for modelling (Table 4.1) were obtained by Carbosulcis S.p.A.

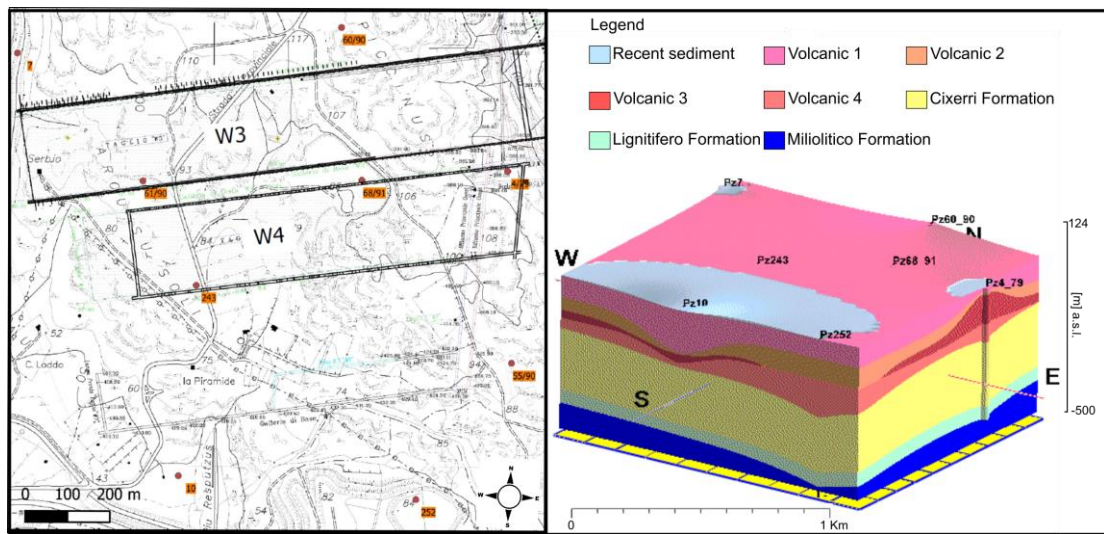


Figure 4.4. Location of stratigraphic logs used to elaborate 3D geological model of subsurface (on right).

Geology layer	Unit weight	Young's modulus	Poisson's ratio
	γ	E	ν
	kN/m ³	[kN/m ²]	[-]
Volcanic 1	22	2.60 x 10 ⁷	0.25
Volcanic 2	14	1.94 x 10 ⁶	0.25
Volcanic 3	22	2.00 x 10 ⁷	0.21
Volcanic 4	23	1.06 x 10 ⁷	0.12
Conglomeratic Cixerri Fm.	22	1.00 x 10 ⁶	0.40
Cixerri Fm.	24	9.00 x 10 ⁶	0.30
Lignitifero Fm.	13	1.00 x 10 ⁵	0.28
Miliolítico Fm.	26	1.50 x 10 ¹⁰	0.30

Table 4.1. Geotechnical parameters used for modelling. The volcano-pyroclastic rocks and ignimbrites are named Volcanic 1 to 4. The Cixerri Fm. is subdivided into two patterns.

As reported in Table 4.1, due to similar geotechnical parameters, the twelve ignimbrite plateaus overlying the sedimentary units were grouped in four geotechnical layers. Cross sections (width = 200 m, height = 3 m) of panels W3 and W4 were considered into the 2D model at the depth of 400 m. Each rock layer has been considered in the numerical model as linear elastic, with Young modulus E and Poisson ratio ν as reported in Table 1. Evaluation of the overall subsidence (total vertical displacements of the surface) has been performed at the end of the following calculation steps: 1) initial in situ stresses (geostatic stresses), 2) excavation of W4 panel, and 3) excavation of W3 panel.

4.6. Results

4.6.1. Processing phase

Starting from two satellite datasets, four PS-displacement rate maps for both acquisition geometries (ascending, descending) have been created. The PSs obtained were imported into GIS platform and subsequently made visible according to a colour scale: negative values conventionally indicate a movement of the target away from the satellite (LoS), while positive values indicate movement towards the sensor; stable areas are shown by using the green color. The maps represent the average velocity recorded during the period covered by the acquisitions (Figure 4.5). The results of both ascending and descending geometries show that the predominant

displacement rates are located in correspondence of the panels. In the central part of the monitored area, in the first period considered (2011-2014), PS-deformation velocities exceed the detection limits (Colesanti et al., 2006), and no satellite-based measurements are available. On the contrary, in the second period analyzed (2013-2020), the same zone is covered by PS-measurements.

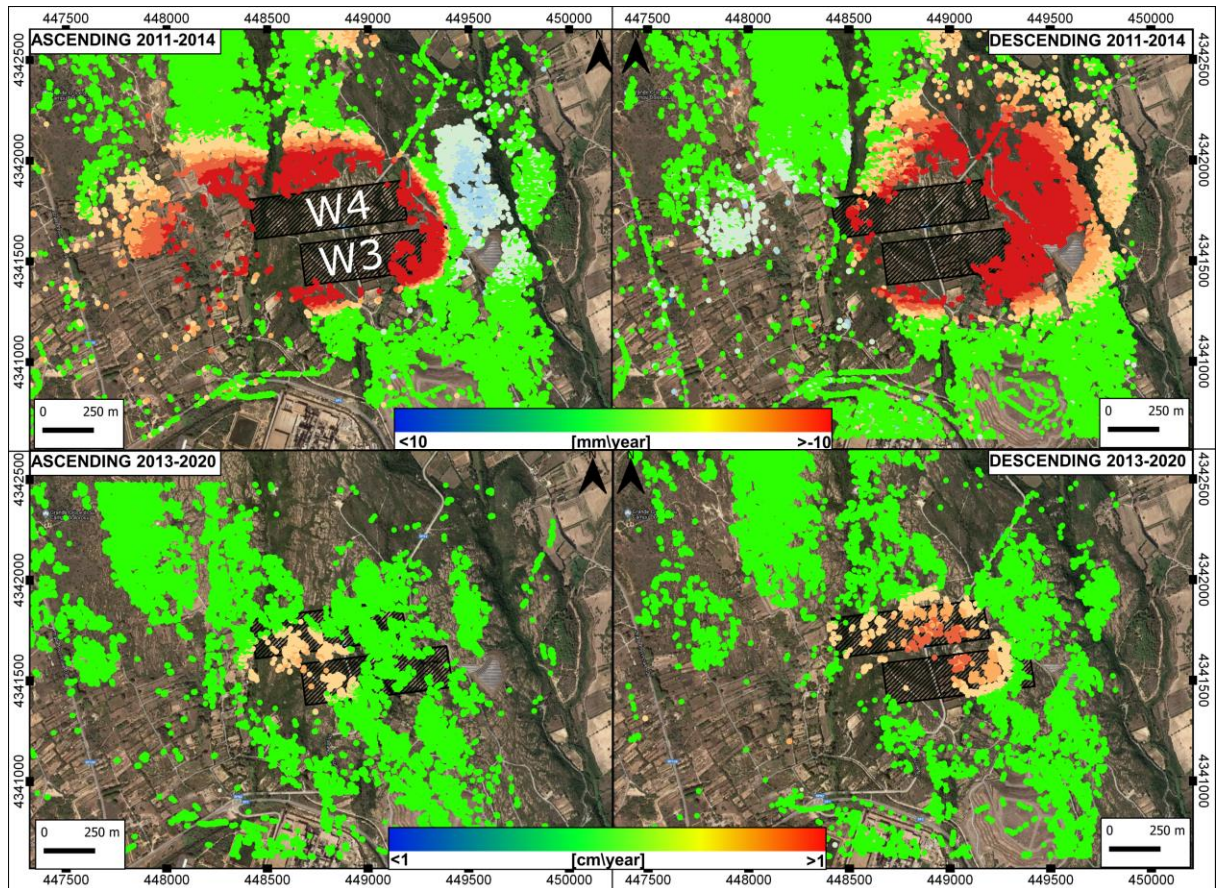


Figure 4.5. Mean displacement rate map in ascending and descending orbit.

This fact is likely related to the decrease of displacement velocities. Indeed, the cumulated satellite-based LoS displacements vary between -130 and $+28$ mm (until January 2014), -293 and $+28.4$ mm (until March 2014) and between -6.9 and $+1.6$ mm (until March 2020), -8.72 and $+4.33$ mm (until March 2020) in ascending and descending geometries, respectively.

4.6.2. Post-processing phase

The numerical model produced a simulation of the subsidence induced at the surface by the two mined panels. The model was produced along a N-S section crossing both the W3 and W4 panels (Figure 4.4). In order to reproduce the chronology of the events and analyzing if the differential exploitation of the two panels influenced the total measured subsidence, two calculation steps were performed. The first was

related to the sole exploitation of the panel W4 (occurred from 2008 to 2010), whereas the second was related to the excavation of W3 panel (occurred from 2010 to 2012). The Figure 4.6 shows that vertical displacements reach a maximum value of 32 cm. The lateral extent of the subsidence covers a horizontal length of about 1100 m, that is quite wider than the mined panel size. At the surface, the expected vertical displacement reaches a maximum value of 18 cm.

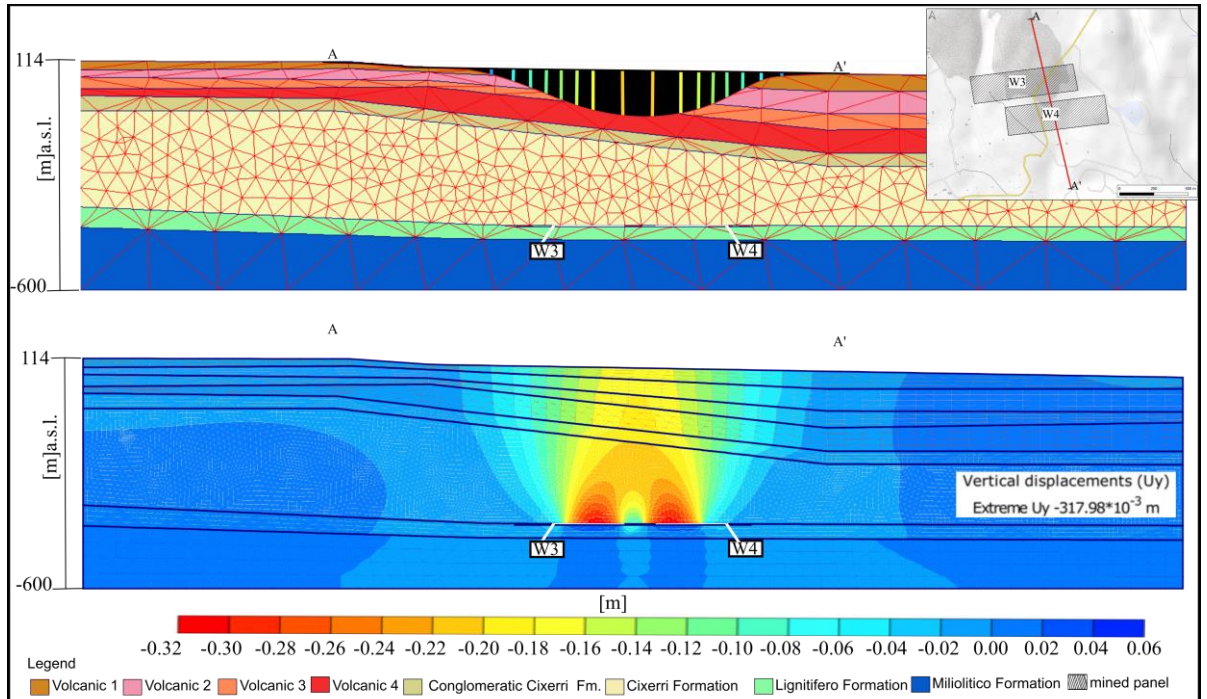


Figure 4.6. Vertical displacements were obtained with the geotechnical numerical model. On top subsidence profile related to the section AA'.

The availability of both ascending and descending datasets allowed to reconstruct the kinematics of the deformation by means of the displacement vector decomposition (Figures 4.7 and 4.8). The results, as shown in Figures 4.7 and 4.8, are maps of vertical (VC) and horizontal (HC) components, with the total amount of displacement calculated in the time span 2011-2020. Considering a x, y, z Cartesian coordinate system, HC maps coincide with the horizontal E-W and the VC maps with the vertical components. VC and HC were calculated considering three phases: pre-mining, syn-mining and post-mining activity. The availability of satellite dataset allowed to obtain one map during the pre-mining activity related to September 2011, where no displacement has been detected. During the W3 panel extraction carried out in the period 2011-2012 the displacement vector components were analyzed every two months. To understand the temporal evolution of displacements the progress of

mining exploitation (i.e. the position of the exploitation front) has been integrated to the vector maps.

The post-mining activity was investigated every year from January 2013 onward. It is important to note that during the extraction of W3 panel, between November 2011 and October 2012, only slight deformations can be identified. In detail, displacements started in November 2011 and developed until October 2012 with maximum cumulated vertical displacements of ca. 11 cm and horizontal ones between -14 cm and 4 cm. On the contrary, the largest deformations were detected in correspondence of post-mining operations, during the time span January 2013 to January 2014. Subsequently, subsidence continued slowly until January 2020 with maximum cumulated vertical displacements of ca. 26 cm and horizontal ones between -24 cm and 7 cm, with a variability of 1.5 - 6 cm.

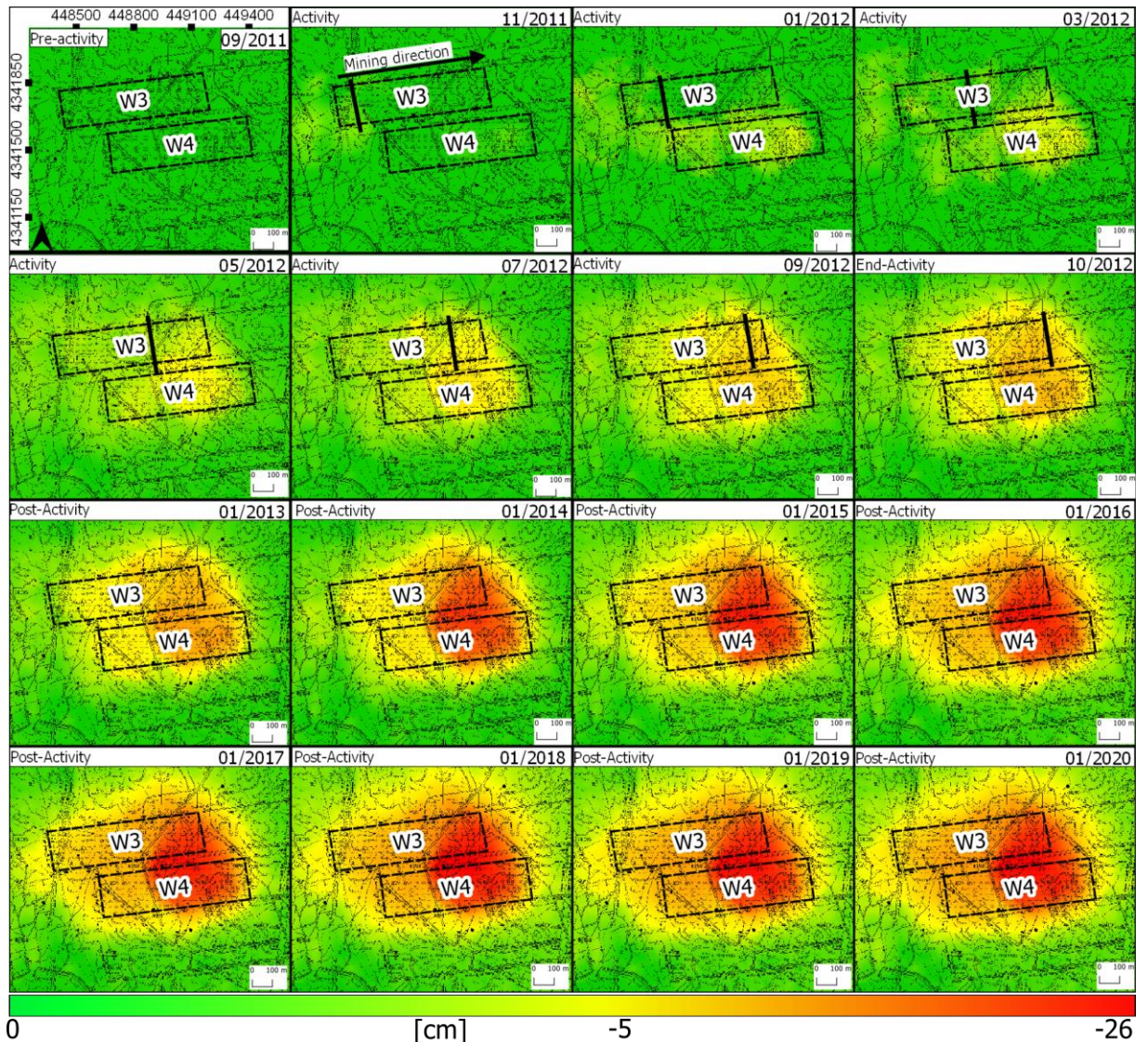


Figure 4.7. Vertical deformation maps pre-mining, syn-mining, and post-mining activity. Black dashed lines in the figure represent the mining panels.

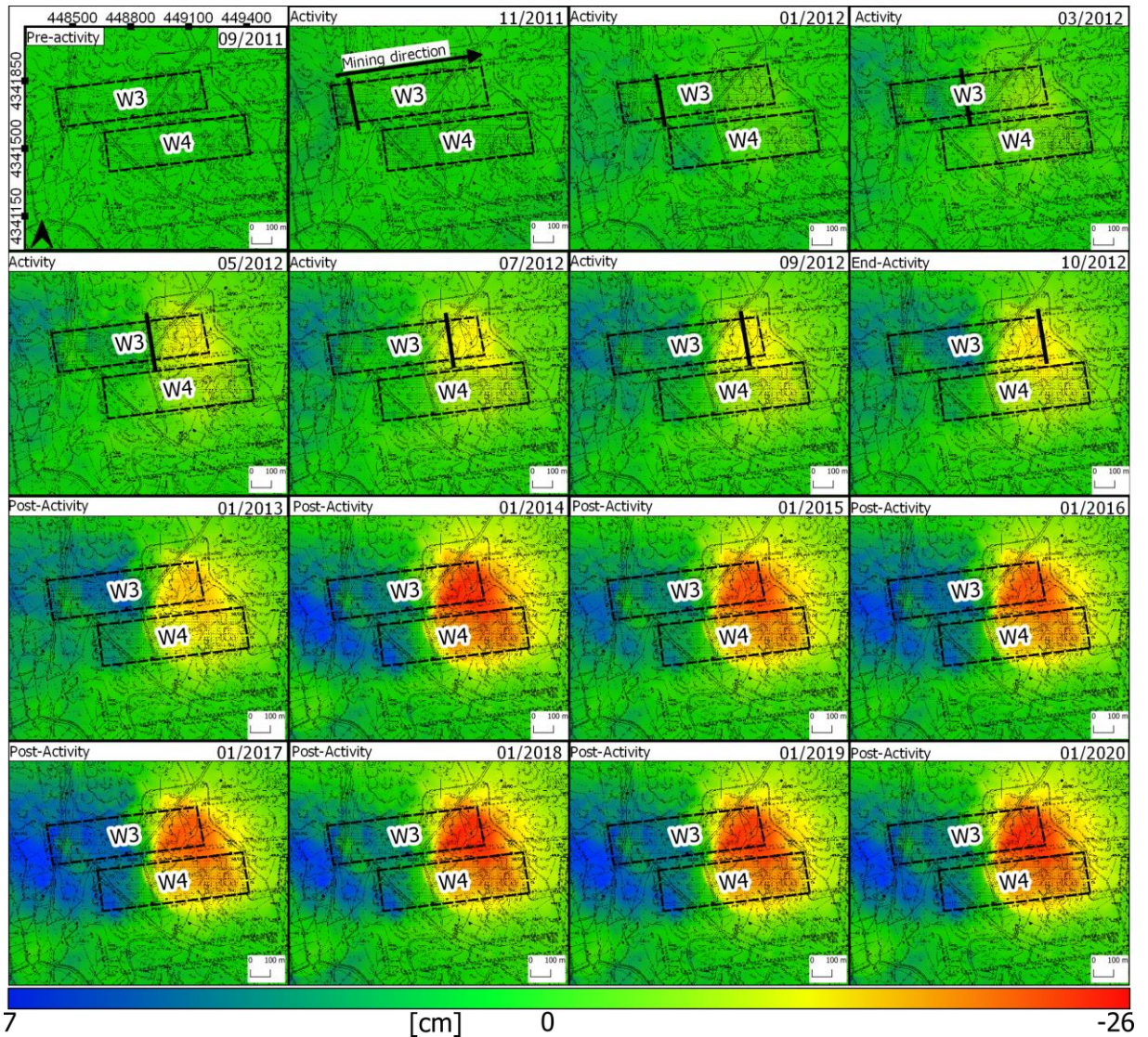


Figure 4.8. Horizontal deformation maps pre-mining, syn-mining, and post-mining activity. Black dashed lines in the figure represent the mining panels.

4.7. Discussion

The aim of this work is to create a near-real time system for monitoring mining activity starting from PS-maps and using a subsurface3D geological model. The threshold subsidence was defined in the geotechnical numerical model of the rocks overlaying the two mining panels W4 and W3. Subsequently, the temporal vertical and horizontal component maps were created for monitoring the mining area during the exploitation and post-exploitation activity. Figure 4.9 shows the temporal evolution of vertical displacements along the N-S oriented profile cross-cutting the mined panels, compared with the expected subsidence along with the same profile, as it was generated by the numerical model. The deformation started in November 2011, in correspondence with the W4 panel, and developed and extended until 2020, with maximum cumulated vertical displacements of ca. 26 cm located in the centre of two

panels. It is important to note that most of the subsidence was temporally delayed respect to the coal exploitation.

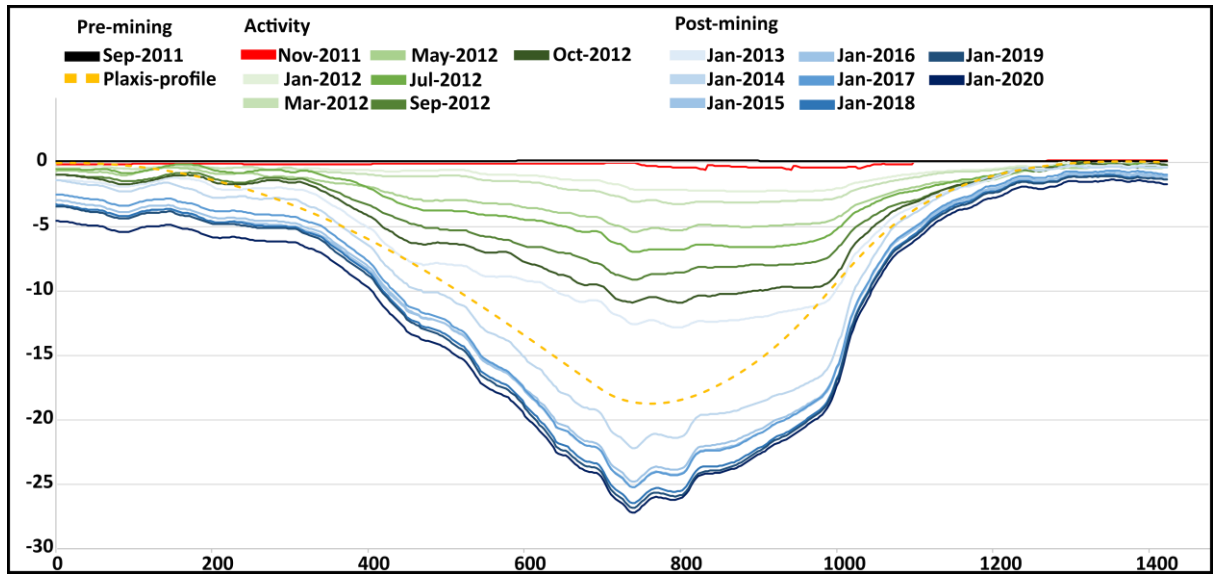


Figure 4.9. Cumulated vertical deformation profiles during the pre-mining, syn-mining, and post-mining activity. Yellow dashed lines in the figure represent the subsidence threshold

In fact, during the mining activity the subsidence threshold was not exceeded, whereas the maximum deformation occurred during the post-mining operations. The delayed occurrence of the maximum deformation depends on several factors: peculiar features of the overburden geology, thickness of the panels, depth of the excavation area, and characteristics of the mining method. Several coal mining districts located in different countries, characterized by variable geological settings, show temporal delays in the occurrence of maximum surface deformations. This particular subsidence phenomenon, that is called residual subsidence (Al Heib et al., 2005), continues after the extraction and in some cases can occur some months or years after the end of the underground mining activity (Huang et al., 2020, Cui et al., 2020, Modeste et al., 2021). Sometimes the residual surface deformation could be also characterized by uplift phenomena (Vervoort 2020). To understand the surface displacement, in Table 6.2 maximum horizontal (E-W direction) and vertical components are compared with mining progress. During the extraction in 2011-2012, the major displacement reported showed a horizontal component. This was likely due to the position of the new mined zone. Subsequently, it is possible to note that the vertical displacement increases respect to the horizontal one. After the conclusion of mining activity, the deformation is concentrated between the two panels in the area characterized by the greatest geotechnical weakness (Table 6.2). This confirms that

the observed displacements are related to the excavation development. W3 panel was mined from 2011 to 2012 and the highest deformation increment was detected in January 2013, with differential vertical displacements of ca. 10 cm. In later times, the increment is of a few centimeters per year, with values decreasing with time until now.

Date	Mining Progress (m)	Vertical displacement max (cm)	Horizontal displacement max (E-W, cm)	Horizontal displacement max (W-E, cm)
Nov-11	95	-1.00	-1.40	1.00
Jan-12	102	-2.60	-3.20	1.90
Mar-12	160	-3.30	-5.80	3.00
May-12	120	-5.40	-9.60	3.50
Jul-12	118	-6.80	-10.70	3.70
Sep-12	78	-8.90	-10.40	4.22
Oct-12	37	-11.25	-14.50	4.33
Jan-13	/	-13.00	-14.48	5.32
Jan-14	/	-22.21	-19.21	6.15
Jan-15	/	-24.80	-22.30	5.29
Jan-16	/	-25.18	-21.50	6.70
Jan-17	/	-25.20	-21.20	7.50
Jan-18	/	-26.20	-24.60	6.00
Jan-19	/	-26.30	-23.48	7.37
Jan-20	/	-26.40	-24.30	7.23

Table 6.2. Maximum vertical and horizontal displacements related to mining progress.

According to several authors (Cui et al. 2000, Al Heib et al. 2005, Cui et al. 2020, Tajduś et al. 2021), subsidence due to longwall mining is structured into three intervals. The first called initial subsidence is the period when the surface movement lightly starts with low velocity. The second phase, called “principal”, is considered when displacements increase, generally up to 80 to 90 % of final subsidence. The final phase, named “delayed” or “residual” period, is associated with surface

subsidence that continues after the end of mining activity, and can be characterized by 10 to 15 % of final subsidence. This “delayed” period can start around 12 to 18 months, or also around 3 to 4 months after the end of the underground excavation, depending on the high or low geotechnical quality of the overburden strata, respectively. In the Nuraxi-Figus study case, the second subsidence phase ends one year after the end extraction (Figure 6.10), when the vertical displacement achieves about 84% of final subsidence. The delayed subsidence starts in January 2015 and develops slowly with a rate of about 20 mm/a (7% of final subsidence).

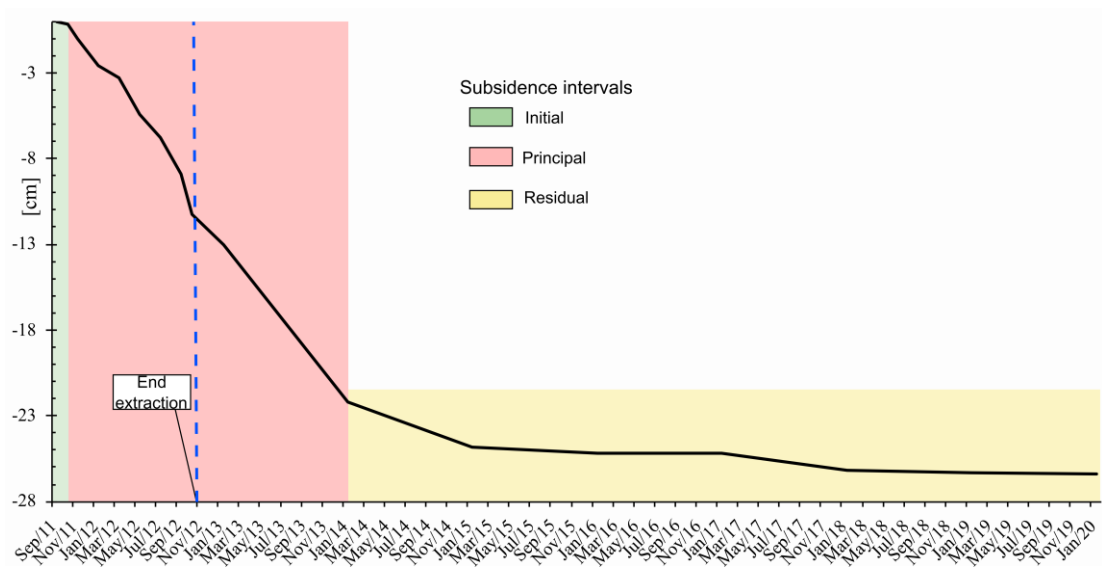


Figure 6.10. Profile of vertical cumulated displacement max. The three subsidence phases: initial (green), principal (red), residual (yellow).

In the initial stages of underground mining, the caving zone is characterized by elastic deformations that recede if the overburden forces are deleted. If extraction continues after a certain threshold, deformations become permanent. In this case, the pressure on the exploited areas increases, the sides move inward, the floor is subjected to uplift and the roof slides down (National Coal Board book 1975; Shadbolt et al.1978). According to Whittaker (1989), deformation occurring above a mining goaf depends on the following factors: depth of the cover, properties of overburden strata, seam thickness, geometry of the extraction panel, surficial topography, and extraction techniques. Specifically, in the underground mining four zones can be identified in the rock pile occurring above the extraction area. Starting from the bottom to the top there are: I - the zone immediately above the extraction area (caving zone), II - the fractured zone where the major cracks are present; III - the deformation zone, and IV – the surficial zone where subsidence could occur (Peng

1992). According to Mills (1998), the maximum subsidence (S_m) expected in an underground mining area is related to the width of the extraction panel (W), and height of cover strata (H). By using these parameters, it is possible to identify three types of excavation areas (Whittaker et al. 1989; Mills 2009):

- Supercritical ($W/H > 1.6$): S_m could be between 55% and 65% of the mined seam thickness;
- Critical W/H (from 0.6 to 1.6): S_m could be about 10% of the mined seam thickness, depending on changes in panel geometries, on the overburden depth and the composition and geotechnical properties of the strata;
- Subcritical ($W/H < 0.6$): S_m is negligible.

Applying the above subsidence model to the study area, it is possible to say that the caving zone should be completely included in the Lignifero formation, whereas the fractured zone should affect the lower part of the Cixerri formation. The residual overlaying part of Cixerri formation and the volcanic rocks should belong to the bending zone. In the geotechnical numerical model it is possible to note that the maximum displacement is related to the Cixerri Formation. This is probably due to pre-existing structural discontinuities (fractures and faults), occurring in this Formation (Fadda et al., 1994). The surface zone is instead characterized by slight surface movements.

4.8. Conclusion

In this study, an integrated approach for near-real time mining monitoring was presented. Indeed, the method allowed to detect a subsidence phenomenon that occurred during the mining activity and continued also for a few years after the completion of mining work. The study confirms that ground surface deformations can occur also in areas subjected to very deep underground mining and that the DinSAR techniques produce reliable results in terms of monitoring in a certain time span. The geotechnical numerical method can be used as subsidence forecasting model allowing to obtain a ground displacement threshold. In underground mining areas, it is important to use monitoring techniques that can provide cost-effective regional perspectives for preventing possible negative environmental effects. The near real-time monitoring system applied in this study proved to be very useful for detecting subsidence during the mining activity and in the post-mining period. Therefore it can be used for planning environmental remediation plans. However, to support the previous analysis and better investigate the subsidence-related cause-effect mechanism, as effectively as possible, might be necessary to also acquire additional external data (i.e. leveling surveys, extensometers).

5. Sentinel-1 data for monitoring a pre-failure event of tailings dam

5.1. Abstract

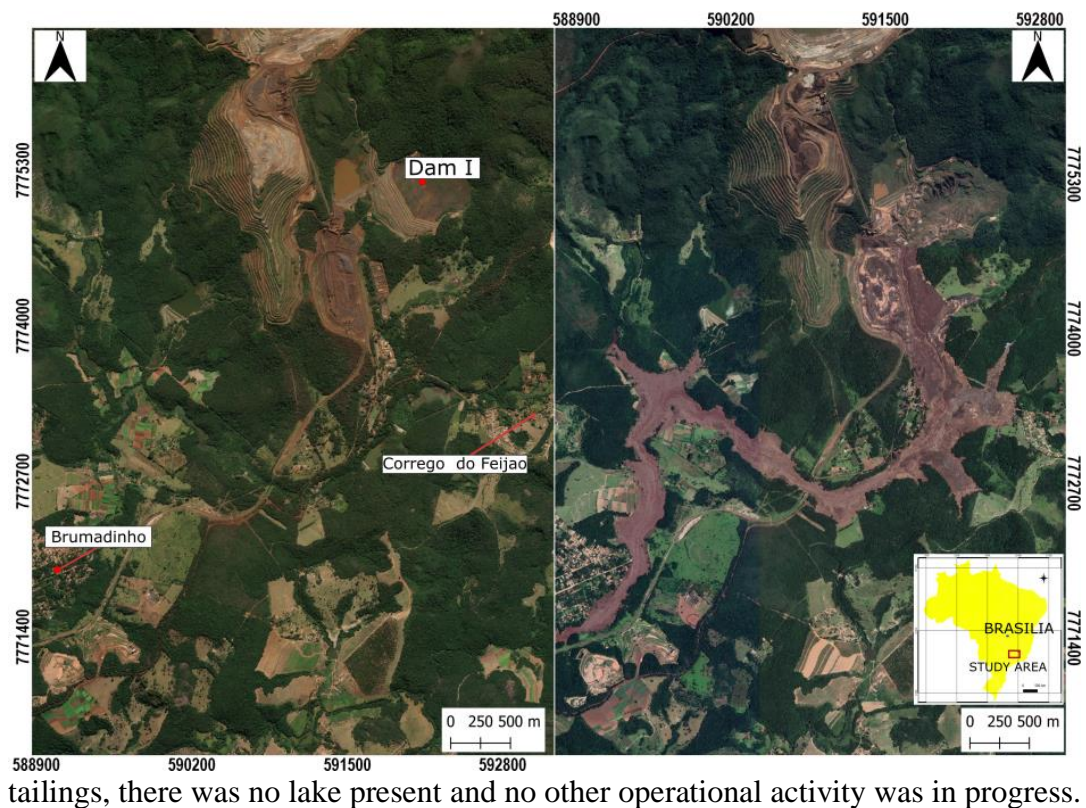
In the present work, an advanced differential interferometric synthetic aperture radar (A-DInSAR) technique has been used to detect the displacements of the upstream tailing dam of Vale's Córrego do Feijão. The study area is located to 9 km east of Brumadinho, Minas Gerais, Brazil, where on 25 January 2019 the dam was affected by a catastrophic failure causing a huge flood that destroyed the mining officers, houses, roads and 257 people died as a result of the collapse. The dam was built in 1976 by Ferteco Mineração using the upstream heightening method, the latter consists to build the dam body using the deposited tailings. The vale's dam height was 86 meters and its crest length was 720 meters. The tailings occupied an area of 249.5 thousand square meters and the disposed volume was 11.7 million cubic meters. The study has been carried out using the 64 descending satellite images acquired as single look complex (SLC) from Europe space agency of the Copernicus programme. The data have been processed by means of coherent pixels technique (CPT) algorithm. The result consisted of a map of displacements on the body dam from the 2016 to 2019, in the period before the collapse. Furthermore, the study of the time series of displacements allowed to assess the evolution of dam structure deformations. The study confirms that the A-DInSAR technique could be very useful tool for monitoring tailings dam and to reduce the risks.

5.2.Introduction

Nowadays the increase mining activity is aimed to obtain a huge variety of mineral resources, which are used to satisfy the diverse needs of men, as energy, construction, etc. Such growth, indirectly, generates a large production of residues that must be treated and managed to improve the economic efficiency and the environmental sustainability. There are several kinds of mining waste management, but a lot of companies use the tailings dam. The latter have many features in common with embankment dams, but are built to retain impoundments of tailings, and when possible, mining material extracted is used in their construction. The tailings dams can have several structural problems derived from hydraulic or foundation stability and sometimes they can collapse (Azam et al. 2010; Kossoff et al. 2014) In order to forecast the effects that a potential breach could induce, it is necessary to implement the most effective monitoring techniques. Among them, the Advanced Differential Interferometric Synthetic Aperture Radar (A-DInSAR) technique has proved to be among the most cost-effective and reliable, allowing, on one hand, to identify a "natural" network of targets over wide areas and, on the other hand, to obtain a sub-centimetric accuracy in the measurement of displacements. As regards the application of this technology to the monitoring of artificial barriers, different fields of application can be distinguished (Fan et al. 2015; Przyłucka et al. 2015; Ammirati et al., 2020); to asset the displacement to dam structure (Di Martire et al., 2014; Milillo et al. 2016; Mura et al., 2018; Ullo et al. 2019; Du et al. 2020). In this work, it has been investigated surficial displacements, which occurred between 2016 and 2019, in association with a tailing dam located in Brumadinho area (Minas Gerais region, Brazil). The latter on 25 January 2019 collapsed, releasing almost of 12 million cubic meters of tailings. In particular, the displacements have been investigated in the period immediately before the dam breakage and compared with the rainfall data recorded in the same period, in order to assess a possible cause/effect relationship. To pursue this aim, Sentinel-1 data derived from Europe Space Agency of the Copernicus Programme and the rainfall report acquired from Cemaden website (www.cemaden.gov.br) have been used. Rainfall data were acquired in order to verify the cause-and-effect relationship with the break-age of the dam in 2019.

5.3. Study Area

The study area is in Brumadinho district about 65 km from Belo Horizonte city, in Minas Gerais region of Brazil (Figure 5.1). The area is identified for several mineralization that have been exploited when the mining industry diversified intensely, and the country became one of the six largest mineral producers in the world. Specifically, the study area is also known for numerous occurrences of iron mineralization. In the last years, the mining licenses have been owned by Vale Company, which mined the iron ore in several sectors of the Córrego do Feijão mine. The company exploited the ore, mainly with open pit mining, storing tailings in a dam, called Dam I. The structure was built in 1976 by Ferteco Mineração S.A. company, later acquired by Vale on 2001. The dam height was 86 meters and its crest length was 720 meters. The tailings occupied an area of 249.5 thousand square meters and the disposed volume was 11.7 million cubic meters. After the 2015, the dam has been inactive and according with Vale company the structure was no longer receiving



tailings, there was no lake present and no other operational activity was in progress.

Figure 5.1. Study area. On left pre-event; on right post collapse.

In detail, the Dam I that was collapsed in January is an upstream dam type. According with Vick (1990) this type of dam is the oldest and most economical method.

The construction of an upstream starts with a pervious dike at the down-stream toe should be capable of passing seepage water. Later, the tailings are discharged from the crest of the starter dam generating a new level that becomes the foundation of the next dam. Before the next stage, a mechanical compaction of the dike is conducted. The upstream dams are of wide area and are composed of coarse material.

5.4.Dataset

In order to assess the displacements occurred at the Dam I, two types of data have been used. Firstly, we used the Sentinel-1 images consisting in 64 radar images, covering the temporal span from 23th October 2016 to 17th January 2019, acquired as Single Look Complex (SLC) in descending orbit. Secondly, we also considered rainfall data existing in the Minas de Gerais. The daily rainfall data were acquired for the period 2016-2019, in three stations: Alberto Flores, Distrito Casa Branca and Córrego do Feijão (Figure 5.1). The Coherent Pixels technique (CPT – Mora et al., 2003; Iglesias et al., 2015) algorithm has applied to satellite images using the SUBSOFT software, developed by the Remote Sensing Laboratory (RSLab) group from the Universidad Politècnica de Catalunya (UPC). A-DInSAR results consist of LoS-projected mean displacement rate map and time series of deformations. The database reports the qualitative information on the data, the value of LoS displacements and the mean displacement rate relative to the entire data processing interval. Using Qgis software, the A-DInSAR data has been showed like a point vector map (Figure 5.3).

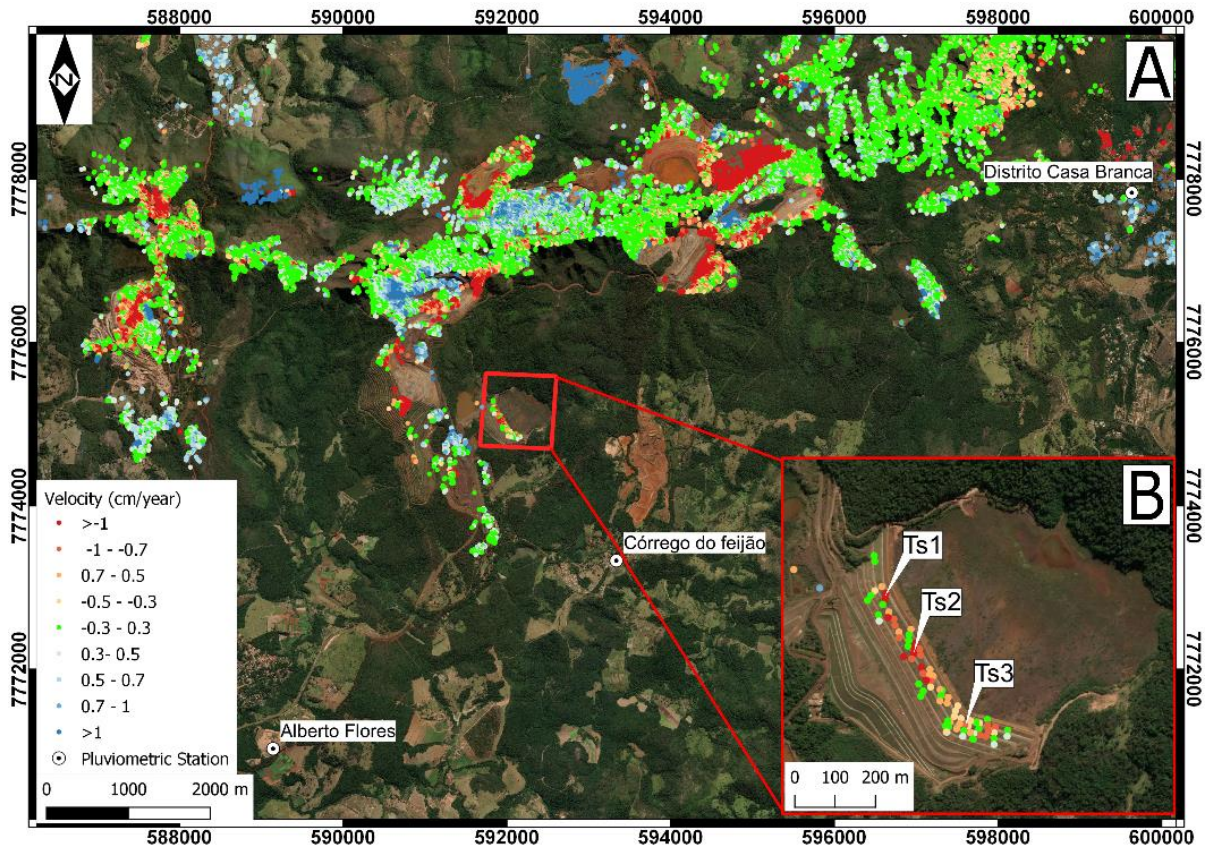


Figure 5.2. A) mean displacement rate map in descending orbit, ts1-3 are points for time series profiles. B) the selected area.

In Minas Gerais area we detected about 37 thousand targets in descending orbit. In order to monitoring the Dam I, the interferometric information have been extracted in its body. By means of a Qgis function, in the dam area about 100 targets have been identified. From the rainfall report it was possible to obtain information related to precipitation during the period also covered by the Sentinel-1 data. The dataset was obtained from Cemaden website (Centro Nacional de Monitoramento e Alertas de Desastres Naturais, <http://www.cemaden.gov.br>), covering the period from March 2016 to January 2019. The data report the information of the rainfall measurements monthly cumulative (mm) (Table 5.1). In particular, data derived from three meteorological stations located near the Dam I have been used (Figure 5.2).

Table 5.1. Rainfall dataset. / = not available

	Alberto Flores (1)	Distrito Casa Branca (2)	Córrego do feijão (3)
	[mm]	[mm]	[mm]
03/2016	142.15	0.2	266.47
04/2016	28.33	/	37.19
05/2016	2.6	/	0.8
06/2016	55.47	/	77.69
07/2016	1.2	/	45.06
08/2016	2.58	/	34.22
09/2016	62.71	/	89.5
10/2016	105.56	0.42	69.47
11/2016	184.29	258.5	170.22
12/2016	296.19	291.97	347.79
01/2017	133.11	134.24	159.47
02/2017	147.18	206.12	109.69
03/2017	122.39	92.41	/
04/2017	23.03	27.2	/
05/2017	23.2	21.67	/
06/2017	10.66	27.27	/
07/2017	0.2	0	/
08/2017	0	0	/
09/2017	13.43	29.19	/
10/2017	126.62	29.19	/
11/2017	118.08	129.73	/
12/2017	262.62	228.69	/
01/2018	226.51	132.71	/
02/2018	247.32	192.4	/
03/2018	243.15	163.39	/
04/2018	19.34	19.58	/
05/2018	6.13	29.19	/
06/2018	4.54	0	/
07/2018	0.4	13.95	0.79
08/2018	44.56	173.51	58.7
09/2018	110.06	83.52	141.87
10/2018	116.05	114.56	128.21
11/2018	210.33	241.23	225.67
12/2018	174.17	193.18	226.55
01/2019	41.61	72.52	74.01
02/2019	170.93	326.55	255.16
03/2019	100.72	92.7	147.75

5.5. Results and discussion

The results allowed to determine the surface ground displacements in terms of mean displacement rate map and time series of deformation, along the LoS of the satellite. In order to study the displacement occurred on the Dam I, the cumulative displacement values in correspondence to structure were interpolated using Kriging algorithm (Fig. 5.3).

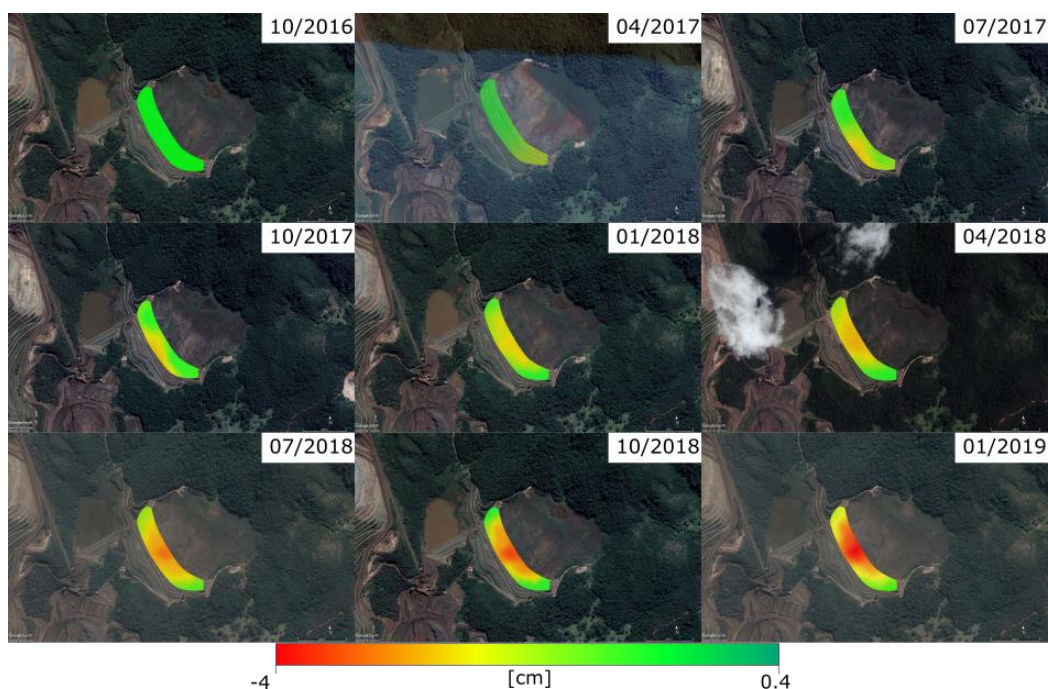


Figure 5.3. Interpolated Los displacement maps.

The maps describe the displacement, in cm, recorded during the period covered by the acquisitions. The visualization factor is made by using a color scale from red to dark green, respectively the negative values conventionally indicate a movement of the target away from the satellite, while the positive values indicate movement towards the sensor, the light green color identifies the stable area. The figure shows the temporal evolution of surface displacements every three months. It is possible to note how the ground surface phenomena starts in April 2017 and develops until January 2019 eight days before the disaster, with maximum LoS cumulated displacement of -3.66 cm. It is important to note that the maximum deformation was detected in correspondence with the center of the embankment. In order to analyze the possible trigger, we studied the time series selecting three targets, located one in the center (Ts2) and the other two in the sides (Ts1, Ts3) of Dam I. Later the results have been integrated with the rainfall data. The monthly cumulated rainfall plotted in Figure 5.4 show the rain variation during the seasons, with the lowest values for the summer and the highest values occurring during wintertime. By comparing the time series of deformations for some points on the top of the embankment (see Figure 5.2), some considerations can be made with the accumulated monthly rainfall. It is worth to point out that among the three available stations, the Corrego do Feijao station did not acquire in the period March 2017 - July 2018. The TS1 point would seem to increase the displacement rate around March 2017 (blue arrow) and then show a quasi-linear trend for the remaining period. The TS2 and TS3 points show a different

behaviour. Both seem to accelerate in June 2017 (black arrow) with almost similar rates until September 2018. In fact, at this date a further increase was only recorded at point TS2 (central sector of the dam - red arrow). Confirming how The TS1 point would seem to increase the displacement rate around March 2017 (blue arrow) and then show a quasi-linear trend for the remaining period. The TS2 and TS3 points show a different behaviour. Both seem to accelerate in June 2017 (black arrow) with almost similar rates until September 2018. In fact, at this date a further increase was only recorded at point TS2 (central sector of the dam - red arrow). Confirming how this was the most stressed sector of the dam. This stress was probably related to an anomalous water load present behind the dam. In fact, looking at the graph of rainfall data, it is possible to notice that in 2018 the rainy season would seem to have started already in August 2018, about 2 months earlier than in previous years.

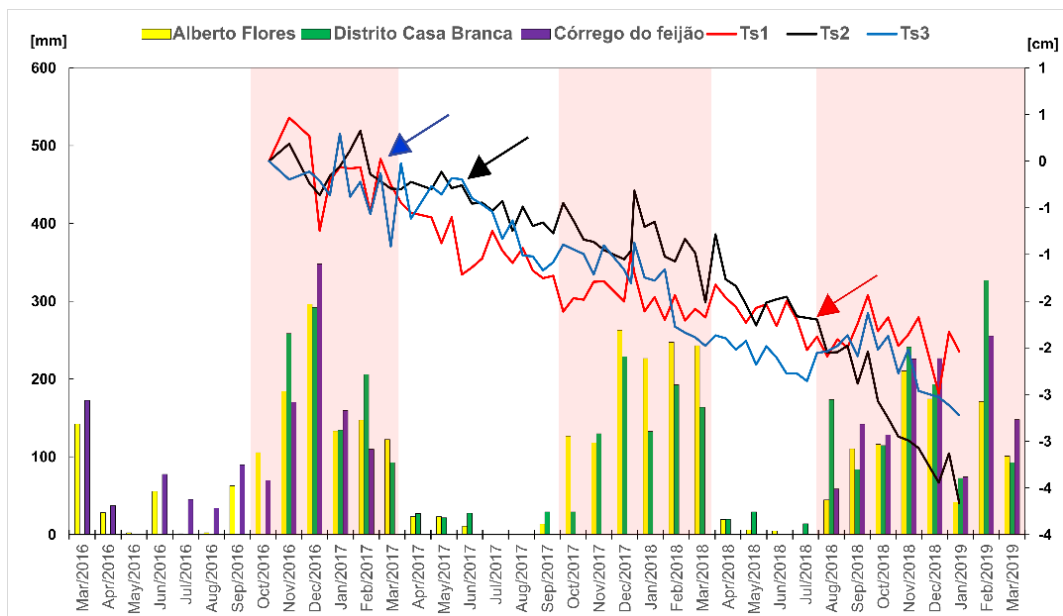


Figure 5.4. The time series of LoS-cumulated displacement (Ts1-3) integrated to rainfall measurements monthly cumulative (mm), highlighting the wet periods. The arrows highlight the increase of the displacement rate.

5.6. Conclusions

In the last years the tailings dam failures have represented a big problem in whole Brazilian area. According with WISE (World Information Service on Energy, <https://www.wise-uranium.org/mdaf.html>) project, and the chronology of major tailings dam failures in the World, during the period from 1961 to 2020, thirty-three events have been registered in South America. Specifically, seven of them are situated to Minas Gerais region. The greatest dam failure event occurred on 25

January 2020 to Brumadinho. Recently, the event has been studied in several work by means of the satellite data (Du et al. 2020; Holden et al. 2020). The authors used the interferometric technique to monitor the trailing Dam I and detected soils deformation in period before the collapsed. According with The New York Times work (<https://www.nytimes.com/interactive/2019/02/09/world/americas/brazil-dam-collapse.html>), deformations started in correspondence of the right side of the Dam I immediately before the collapse. Materials behind the dam were liquefied, but, due to rapid occurrence of the event, it is not clear if the liquefaction was the cause of the failure or it was generated later. In this work, we were able to detect deformations in the body of the dam before the collapse. Specifically, deformation started on a side of the dam and developed with higher values in the central zone. In addition, taking in consideration the meteorological reports and the rainfall data, we recognized an increase of LoS-velocity in September 2018, in a period that seems to be characterized by an anticipated anomalous rainy season. In conclusion, the A-DInSAR technique allowed to detect the centimetric displacements occurred well before the dam collapse. The integration of the remote sensing with the field surveys, could be essential, to carry out the monitoring of tailings dam allowing the authorities to manage the risk mitigation action.

6. Application of multispectral remote sensing for mapping flood-affected zones in the Brumadinho mining district (Minas Gerais, Brasil)

6.1. Abstract

The collapse of the tailing “Dam B1” of the Córrego do Feijão Mine (Brumadinho, Brasil), that occurred in January 2019, is considered a large socio-environmental flood-disaster, counting numerous people died and seriously affecting the local flora and fauna, as well as agricultural areas of the Paraopeba River. This study aims to map the land area interested by the flood by using multispectral satellite images. To pursue this aim, Level-2A multispectral images from the European Space Agency’s SENTINEL-2 sensor were acquired before and after the tailing dam collapse in the period 2019-2021. The pre- and post-failure event analysis allowed to evidence drastic changes in the vegetation rate, as well as in the nature of soil and surficial waters. The spectral signatures of the minerals composing the mining products allowed to highlight the effective area covered by the flood and to investigate the evolution of land properties after the disaster. This technique opens the possibility for quickly classifying areas interested by floods, as well as obtaining significant information potentially useful for monitoring and planning the reclamation and restoration activities in similar cases worldwide, representing an additional tool for evaluating the environmental issues related to mining operations in large areas at high temporal resolution.

6.2. Introduction

On the 25th of January 2019, the tailing dam called “Dam B1” of the Córrego do Feijão Mine (Brumadinho Iron Mine), one of the upstream iron tailing dams located around 9 km east of Brumadinho, Minas Gerais, Brazil, collapsed. The catastrophic failure was considered one of the largest environmental disasters in the World (Vergilio et al., 2020), and caused a huge flood consisting of more than 11 million m³ of mining waste spreading about 10 km downhill, that destroyed mining offices, houses, roads and resulted in a tragic loss of lives, with 259 people died. The polluting flood reached quickly the Paraopeba River: a major tributary of the São Francisco River—one of the largest rivers in Brazil. The flood affected decisively 249.5 thousand m² of the surrounding area, impacting seriously the local flora and fauna and the Paraopeba River aquatic system but also involving the vegetation and agriculture areas (Thompson et al., 2020; Silva Rotta et al., 2020). As a result, human and social consequences, including water supply in the municipalities, tourism, and agriculture economy, were seriously compromised (Vergilio et al., 2020). According to Vergilio et al. (2020) the flood event has produced an increase in Paraopeba river turbidity levels due to the high amount of fine flood material, mainly composed of silt-clay particles and higher contents of Fe and Mn. The water analysis has indicated total heavy metals values up to 21 times above the acceptable, representing risks to the ecosystem (De Minas Gerais, 2019). The environmental impact after the Brumadinho dam disaster has also caused several issues to the surrounding lands. The presence of metals, including iron, aluminum, and manganese, was registered in the affected and unaffected soils samples with values above the acceptable thresholds (Furlan et al., 2020). Even though the Brumadinho tailing dam stability has been subject to local systematic monitoring, it collapsed only three years after the end of mining operations. This was due to water accumulation and infiltration through the dam, causing the increase of moisture contents and saturation of the tailing dam. In this context, the acceleration of the seepage erosion and internal liquefaction processes caused the weakening of the structure of the dam ending into the collapse (Silva Rotta et al., 2020). Investigation about surficial displacement and subsidence rate measuring during the period before the Dam B1 disaster (2016-2019) has been subjected to several studies based on remote sensing techniques and satellite data (Holden et al., 2020; Du et al., 2020; Silva Rotta et al., 2020; Ammirati et al., 2021), such as Advanced Differential Interferometric Synthetic Aperture Radar (A-

DInSAR) analysis. These investigations revealed that before the collapse, deformations of the body of the dam started on the eastern side and progressively developed with higher values in the central zone, in relationship with anomalous rainy seasons (Ammirati et al., 2021). The current study aims to map and assess the land cover affected by the flood due to dam failure by using multispectral satellite data. Spectral sensing quickly allows classifying materials exposed at the Earth's surface based on their mineralogy and chemical properties (van der Meer et al., 2012; F.D. van der Meer et al., 2014), in this case making easier to evaluate the effective area covered by the flood and to investigate the evolution of land properties after the disaster (Gläßer and Reinartz, 2005; Aamir et al., 2021; Kasmaeeyazdi et al., 2022; Sharma et al., 2022; Yan et al., 2022). To pursue this aim, we used SENTINEL-2 images obtained from the Europe Space Agency of the Copernicus Program. The potential of multispectral remote sensing, and more specifically the use of Sentinel-2 imagery, for geological applications and mine waste monitoring has been widely studied (Mielke et al., 2014; Van der Werff et al., 2015; Ge et al., 2020), mainly referring to the VNIR Sentinel-2 bands for the detection of ferric oxides and hydroxides. In fact, if compared to other multispectral satellites commonly used in the geology field, Sentinel-2 provides several relatively narrow bands in the VNIR region of the electromagnetic spectrum (Van der Werff et al., 2015), i.e. band 4, band 8/8A, and band 9 of Sentinel-2 (Mielke et al., 2014; Van der Werff et al., 2015; Ge et al., 2020) (centered at 665 nm, 842/865 nm, and 940 nm, respectively), which fit with the Iron-bearing oxides and hydroxides diagnostic spectral features associated with the electronic transitions involving Fe³⁺ (Cudahy et al., 1997; Crowley et al., 2003). Here below we firstly describe the geology, mineralization, and spectral properties of the investigated areas. Then a short description of the data and the multispectral images processing methods is followed by discussion and conclusions.

6.2. Geological setting

The Córrego do Feijão mine is located along the ENE–WSW-striking Serra do Curral syncline, in the northwest portion of the so-called Quadrilátero Ferrífero (QF) area, located on the southern border of the São Francisco craton in the central portion of the Minas



Figure 6.1. Study area. The red zones are the principal elements (see Chapter 4).

Gerais State (northern Brazil) (Figure 6.1). The Serra do Curral is the host of several iron ore deposits where, together with the Córrego do Feijão mine, the mains are the West-, Central-, and East-Mine of the Usimi-nas mining complex, the Esperança, Jangada and the now exhausted Águas Claras ore deposits (Hensler et al., 2015). The geology of the QF is characterized by the metavol-canic greenstone belt sequence of the Rio das Velhas Supergroup (Dorr, 1969; Chemale et al., 1994), and by the Archean granite-gneiss domes, which border the metasedimentary units of the Minas Supergroup preserved as synclinal keels (Hensler et al., 2017).

The Minas Supergroup (Siderian to Rhyacian) unconformably overlies the Rio das Velhas Supergroup and is divided in the Caraça, Itabira, Piracicaba and Sabará Groups (Guimarães, 1935; Dorr, 1969; Alkmim and Marshak, 1998; Klein and Ladeira, 2000; Cabral et al., 2012). The Paleo- (Statherian) to Mesoproterozoic

metasedimentary rocks Espinhaço Supergroup and the post-Minas intrusive rocks (i. e. the Borrachudo granite; (Rosiere and Chemale, 1996; Baltazar and Zucchetti, 2007) represent the younger sequences in the QF area. Two orogenic events affected the area, (1) the Paleoproterozoic Transamazonian orogeny (2.1–1.9 Ga), which caused uplift of the crystalline basement and folding of the Rio das Velhas and Minas Supergroups, and (2) the Neoproterozoic Brasiliano orogeny (0.8–0.6 Ga), which resulted in complex structures superimposed to the previous deformation, leading to the development of a W-verging thrust belt especially in the eastern portion of the QF (Hensler et al., 2015). Metamorphic grades vary from west to east: greenschist-facies with martite-granoblastic hematite ores characterize the western domain (low-strain domain), while amphibolite-facies with microplaty and specular hematite ores occur in the central and NW parts (high-strain domain) (Herz, 1978; Renger et al., 1994; Pires, 1995).

High-grade hypogene and supergene iron ores are mostly hosted by the Cauê Formation itabirites (Neoproterozoic - (Cabral et al., 2012); or Paleoproterozoic - (Babinski et al., 1995)), basal unit of the Itabira Group (Minas Supergroup), consisting of up to 300m-thick metamorphosed BIFs with sericitic and dolomitic phyllites and marbles intercalations. The mineralization is mainly characterized by veins cross-cutting the above-mentioned metamorphosed iron formation (itabirite) of the Itabira Group (Lüders et al., 2005). Itabirites of the QF have been divided into three different types: (1) quartz-itabirite, composed of recrystallized quartz and iron oxides in alternated bands (Dorr, 1969; Spier et al., 2003; Hensler et al., 2015); (2) dolomite-itabirites, characterized by carbonates-rich layers with hematite microinclusions, iron oxides and less quartz (Rosière et al., 2008; Hensler et al., 2015); and (3) amphibolite-itabirites, that are defined by red carbonates and/or iron oxides with less quartz, similar to the dolomite-itabirite, besides of disseminated amphiboles (Guild, 1953; Dorr, 1969; Pires, 1995). The supergene alteration, which occurred mainly in Paleogene, resulted in the development of a deep weathering profile where goethite is present as the main phase, occurring as alteration rims and porosity-filling replacing former iron oxides (Hensler et al., 2015; Hensler et al., 2017).

6.3 Main features of the Brumadinho tailing Dam B1: structure and geochemical characterization

The 86m-high dam was built in 1976 by Ferteco Mineração using the upstream heightening method and was active until 2015 under operations conducted by Vale S/A. The upstream method consists of building vertically the dam, depositing the tailings through successive uphill accumulation (Silva Rotta et al., 2020; De Minas Gerais, 2019). The construction starts with an embankment where the tailings are discharged from the crest of the starter dam and form the first level. This was compacted and then used to form the foundation for subsequent levels of the wall as the dam is raised. As such, the crest of the dam moves up-stream with each raise (De Minas Gerais, 2019; Furlna et al., 2020). According to Furlan et al. (2020), the diffusion of this old type of dam is related to economic advantages, as it is the cheapest building method, as well as occupies a smaller area compared to the conventional downstream model, resulting in constructing licenses easier to obtain (Silva Rotta et al., 2020). However, the upstream method is considered very dangerous and unsafe (De Minas Gerais, 2019), due to the increasing instability after operations stop and dam deactivation (Silva Rotta et al., 2020). The geochemical characterization of the waste material of the Córrego do Feijão mine released from the Brumadinho Dam B1 collapse (Vergilio et al., 2020) revealed that the iron ore tailings are composed, amongst other elements, of Fe (26.5 wt.%), Al (1.1 wt.%), Mn (0.5 wt.%) and Ti (0.043 wt.%), contained in fine particulate material characterized by ~30% sand and ~70% silt-clay fractions, products of the wet processing method used to classify and purify the iron ore. Mineralogical characterization carried out on iron ore tailing dams from similar mines within the Quadrilátero Ferrífero area (i. e. Fundão Dam, Samarco mining company; (Almeida et al., 2018) showed that the mine waste is composed mainly of quartz and hematite, as main phases, and kaolinite, goethite, and gibbsite present in minor amounts (Almeida et al., 2018; Souza et al., 2021). Fe-bearing phases (hematite/magnetite and associated goethite) are classified as ultrafine (about 76 % of their particles occurring in the range between 37µm and 6µm) and totally free (up to 88% of the particles) material (Souza et al., 2021).

6.4. Methods of study

The present study is based on multispectral products acquired by means of the Sentinel-2 Instrument (Multi-Spectral Image - MSI) of the European Space Agency. The available images from 2019 to 2021 with cloud coverage <5% were processed. In particular, we focused on the months: January 2019, August 2020, and July 2021. The orthorectified Level-2A Bottom-Of-Atmosphere (BOA) reflectance product has been used. In order to obtain a map of the affected flooded areas, the images were selected including the Mi-nas Gerais mining district and covering a period before and after the Dam B1 failure. The thirteen Sentinel-2 bands and their combinations in the visible, Near-Infrared (NIR), and Short-wave Infrared (SWIR) spectral domains, served as proxies for identifying geologic features (F.D. van der Meer et al., 2014), mainly for studying the ferric iron, ferrous iron, laterite, gossan, ferrous silicate, and ferric oxides products. The Sentinel-2 data were very useful for studying the iron-bearing minerals because of their spectral absorption in the VNIR region (bands 6, 7, 8, and 8A), particularly regarding the narrow band 8A, centered at 865 nm (21 nm band width) (Ge et al., 2020) (Figure 6.2). The bands were resampled to the spatial resolution of band B2 (10m) so that all pixels of other bands with 20x20 m² pixel size were loaded. The main aim of the MSI processing techniques adopted in this study was to apply several steps for mapping the flood-affected zones. The work was carried out by using the Sentinel Application Platform (SNAP) developed by European Space Agency (ESA), and the tool called Spectral Unmixing. The materials on the surface are characterized by their own diagnostic spectral properties, called endmembers, and the fractions of each material composing a mixed pixel refer to fractional abundances. The spectral unmixing tool uses the decomposition of reflectance source spectrum into endmember selected. The result of the spectral unmixing is a measure of the contribution of the individual endmember to the source spectrum. This measure is related to endmember's relative abundance. Through the identification in the pre-event map of materials of interest with a spectrally unique signature, that are the so-called principal elements, and of their endmember spectral signatures, the abundance maps were calculated. Therefore, if 30% of a pixel contains the endmember X, 20% of the pixel contains Y, and 50% of the pixel contains endmember Z, the spectrum for that pixel is composed by the sum of 0.30, 0.20, and 0.50 times the single spectra of relative endmembers X, Y, Z. The fully constrained algorithm is used to obtain the sum of abundances equal to 1 and eliminate the

values below zero. An RGB color composite map can be produced, assigning the X, Y, and Z abundances, respectively red, green, blue. For the aims of this work, after the visual analysis of the pre-failure dam image, collected on the 11th of January 2019, we selected as possible principal elements: the water, vegetation, and the tailing dams and mining areas (Figures 6.1 and 6.2). Generally, water is characterized by only reflection in the visible light range, with almost no reflection in the near-infrared range. However, the reflectance may increase between 400 and 1000 nm with turbidity showing maxima between 400 and 700 nm and 800 nm for highly turbid waters (Keshava et al., 2002). Vegetation is generally characterized by an absorption caused by the chlorophyll in the blue range (450–550 nm), a high reflectance in the near-infrared region (~ 865 nm), and strong water absorption in the mid-infrared region (Adam et al., 2010). The tailing dams and mining areas have the spectral signatures of the ferric oxides. The spectral properties of iron-bearing oxide/hydroxide (i. e. hematite and goethite) have been studied in detail by several authors (Curtiss et al., 1985; Crowley et al., 2003). Hematite and goethite are characterized by diagnostic absorption features in the Visible Near InfraRed (VNIR) region of the electromagnetic spectrum, in the range between 450 nm and 1200 nm, due to electronic processes involving Fe³⁺ octahedrally bonded to ligands of oxygen (hematite α -Fe₂O₃) or oxygen and hydroxyl (goethite – α -FeO(OH)) (Hensler et al., 2015). Specifically, goethite generally exhibits the main spectral absorption ~ 940 nm, related to energy level changes in the valence electrons (Crystal Field Absorption features - CFA) (Cudahy et al., 1997). Minor absorption features are at 480 nm and 670 nm (Charge Transfer Feature – CTS) (Cudahy et al., 1997), and the water-related bands occur close to 1,400 nm and 1,900 nm. On the other hand, the major CFA feature appears shifted to shorter wavelengths for hematite, occurring typically ~ 880 nm (Crowley et al., 2003). Absorption position displacements to longer wavelengths of the main Fe-bearing oxides/hydroxides feature (~14 nm; (Scheinost et al., 1999) are due to compositional variations related to Al³⁺ substitution for Fe³⁺ iron. In the present case study, tailing dams and mining areas spectral properties resulted comparable to the hematite signature from the official USGS spectral library (Souza et al., 2020), detectable through the absorption feature in band 8 of Sentinel-2 (centered in 842 nm) which is commonly used to investigate all the iron oxides and hydroxides, i.e. Ferric oxides (Ge et al., 2020; Mielke et al., 2014) (Figure 6.2). Thus,

only water, vegetation, and ferric oxides were considered as valuable endmembers for mapping the most relevant features occurring in the study area.

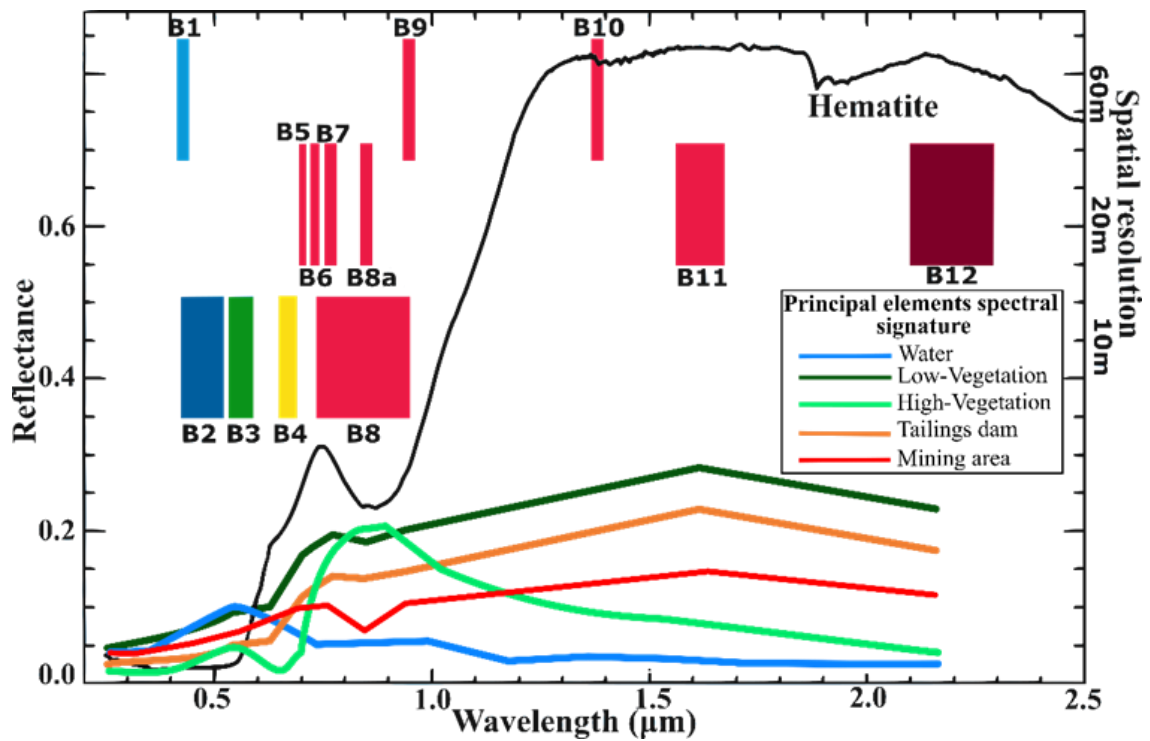


Figure 6.2. The spectral properties of Principal Elements sampled in the pre-event image. The black line is the official USGS hematite signature (Kokaly et al., 2017) compared to Sentinel-2 bands (from B1 to B12).

6.5. Results

Figure 6.3 shows the thematic maps in the Brumadinho mining district, during the pre-and post-failure event, revealing the relative abundances of selected endmember spectral signatures: i.e. ferric oxides, vegetation, and water. The maps have been characterized using a grayscale color, where the zero value indicates that the endmembers are not present, while greater values reveal where the endmembers are present. The water maps allowed to detect the water bodies present in the area, such as the river, and the dam corresponding to the principal elements in Figure 6.1. The temporal evolution of vegetation shows a different spectral response due to the decreasing of vegetated areas. The ferric oxides maps display the distribution of open-pit iron mine areas only in 2019, whereas in the years 2020 and 2021 they show an increase of the white color in the zones where the flood occurred.

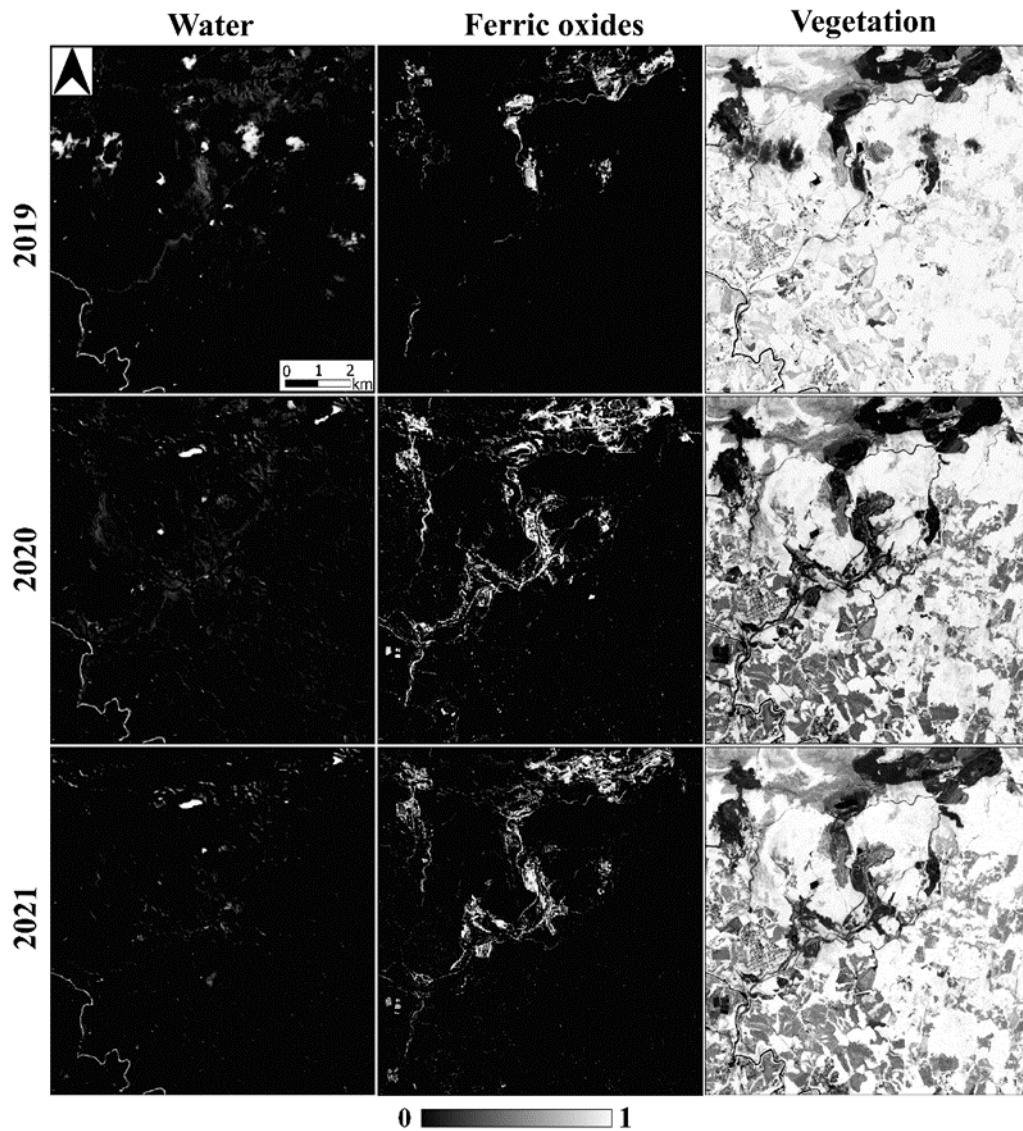


Figure 6.3. The relative abundance maps of water, ferric oxides, and vegetation endmembers, at different periods.

An RGB color composite map was produced, assigning the ferric oxides, vegetation, and water abundances, respectively red, green, blue. This process was applied for post-event satellite images, using the same training dataset as before (i. e. pre-event image). In the RGB maps (Figure 6.4) the red-colored ferric oxides-zones allow to better highlight the shape of the flooded areas in 2020 and 2021 (post-event) images. In all the images most of the considered area is covered by vegetation, but in the post-event periods (2020 and 2021), it is possible to observe a decreasing vegetative rate in flood-affected zones. Four zones have been identified like flood-affected zones where a clear change in the soil nature is not-ed. It is worth pointing out that areas 1, 2, 3 in the top, center, and bottom of the flood-ed area were characterized by an increase in the abundance of ferric oxides. In the 4th area, it is possible to detect pixels changing in the river bed (R) and riverside (RS). Figure 4 shows how in 2020

the affected area was distinguished by an increase in red pixels that are not present in 2019, while a decrease is observed in 2021. Figure 6.5 shows the mean spectral signatures of the flood-affected zones. The graphs are distinguished for the years 2019, 2020, and 2021 and shown respectively in red, black, green, blue, and orange colors. It has to be noted that the flood-affected zones 4th was divided into two mean spectra signatures obtained by the river bed (R) and river side (RS) features.

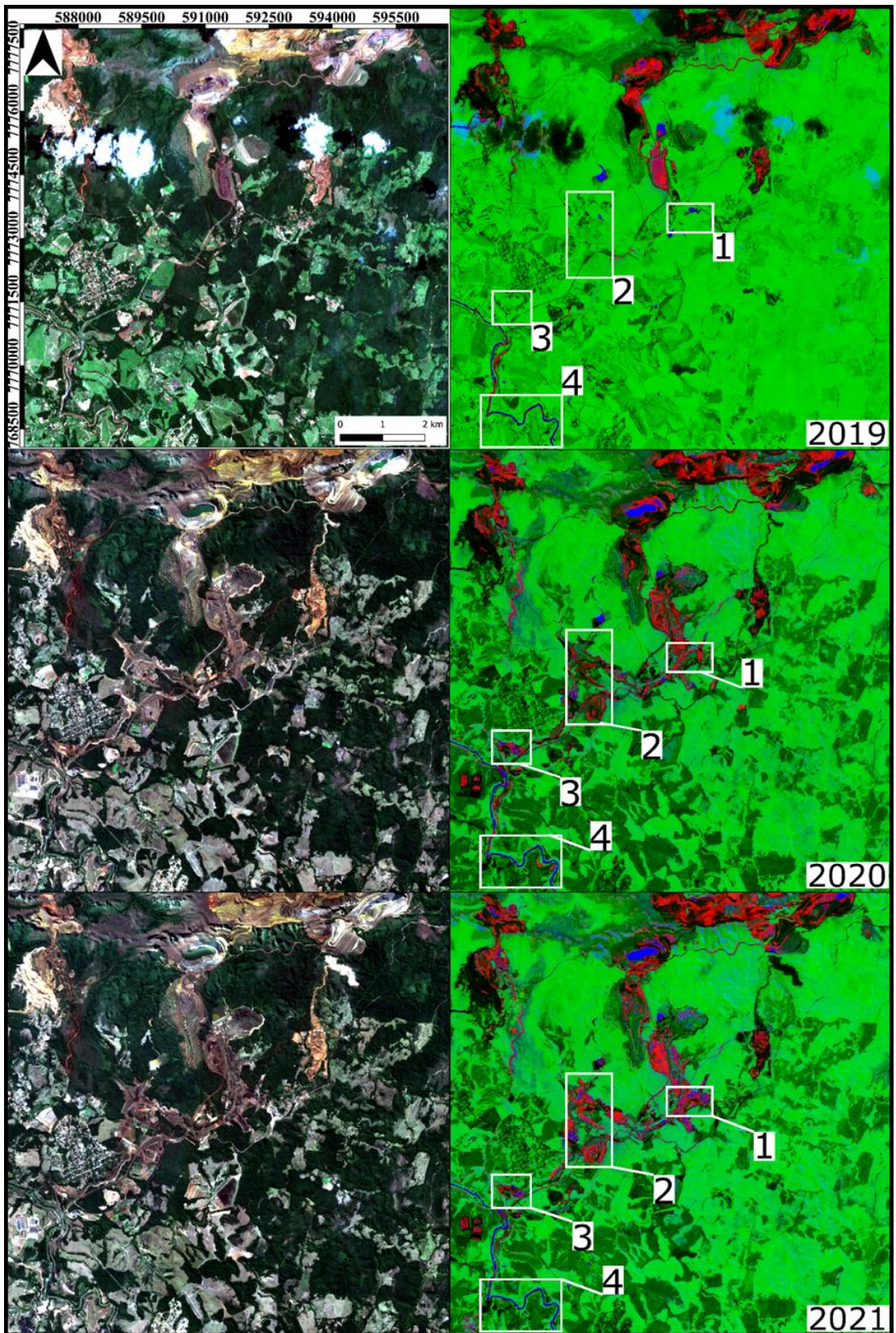


Figure 6.4. The RGB true color on left, the RGB (ferric oxides, vegetation, water) composites with endmember abundances on right. The white boxes are the flood-affected zones selected.

In 2019 (Figure 6.5a), in the Flood-affected zones 1,2,3, and RS, the spectra are characterized by a visible absorption band of about $0.56 \mu\text{m}$, corresponding to the

chlorophyll peak (Sanches et al., 2014), evidencing healthier vegetation. The R spectrum was similar to the water signature with absorption from the mid-infrared region forward. After the flood event, the 2020 and 2021 spectra change. In particular, in 2020 (Figure 6.5b), it is possible to note the main spectral absorption $\sim 0.84 \mu\text{m}$ in the VNIR region characteristic of the ferric oxides (Van der Meer et al., 2014) that decrease in 2021 (Figure 6.5c). Figures 5 b and c show in blue, the spectral signature achieved in 2020 and 2021 corresponding to the river bed area where it is possible to note light absorption in the VNIR region characteristic of the IBeM and an increase in SWIR domains.

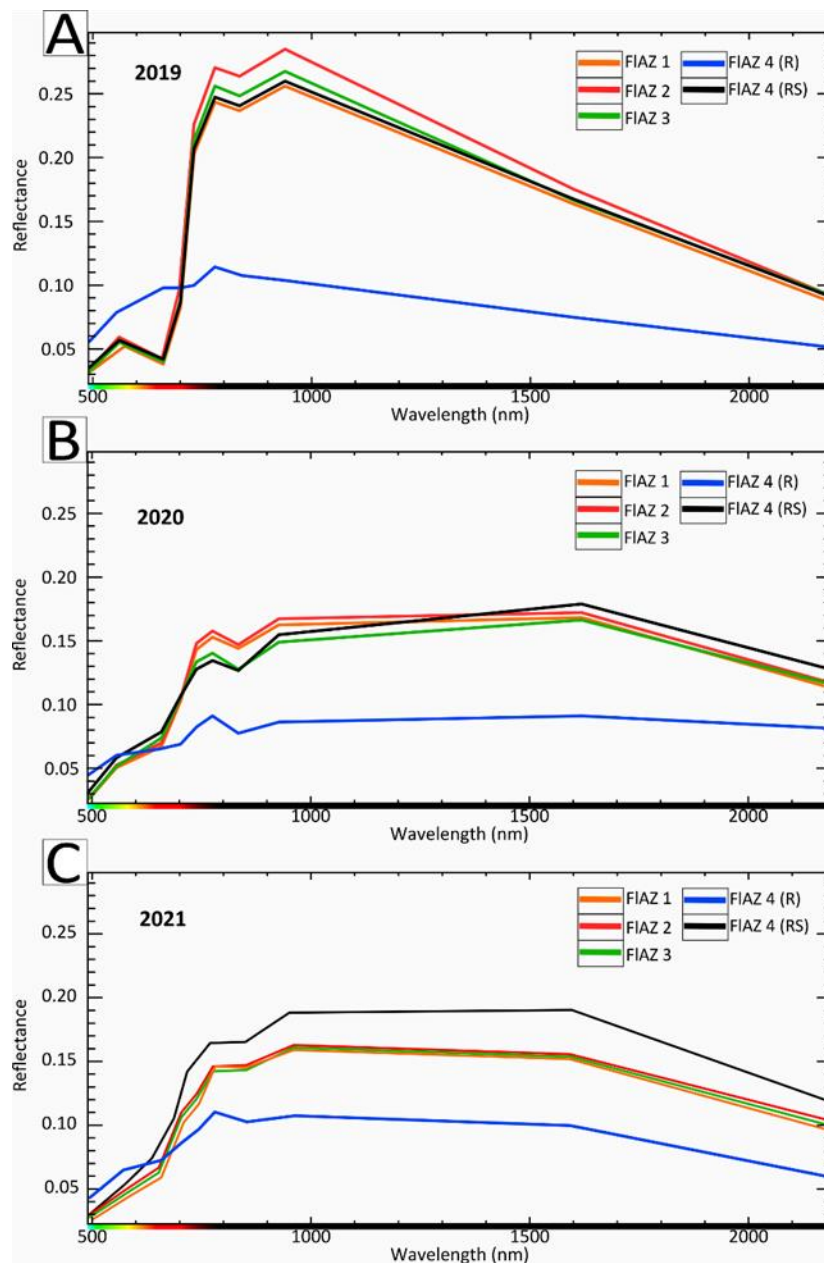


Figure 6.5. Mean spectral signatures obtained by flood-affected zones 1st, 2nd, 3rd and 4th (divided the river bed (R) and river side (RS) features) in 2019 (a), 2020 (b), 2021 (c).

6.6. Discussion

As reported by Silva Rotta et al. (2020) the flood resulted in a massive loss of local vegetation and agri-cultural areas comprising 49 % and 24 % of the areas most affected by the floods. In the present study, the obtained results allowed to investigate the Brumadinho zone affected by the flood phenomena occurred in January 2019. The dam failure provoked fatalities, infrastructure damage, as well as caused considerably environmental aftermaths, which are still now present. This paper aimed to use the potential of multispectral Sentinel-2 data (MSI) to map the flood-affected zones one and two years after the disaster to remotely detect possible signatures still existing in the area. The Spectral Unmixing tool, using the different spectral responses of each material, allowed to identify areas, called Flood-affected zones, where the ferric oxides signature was observed. Satellite Multispectral data have been recently used (Syifa et al., 2019), for studying the Brumadinho dam collapse. The authors, by using artificial intelligence (AI) techniques based on the Landsat-8 and Sentinel-2 bands, defined the pixel classification for the pre-and post-dam failure. The maps produced by using each satellite data (Syifa et al., 2019) allowed to divide the study area into seven and five classes, respectively from the Landsat-8 and the Sentinel-2. The authors affirmed that difference was attributed to the cloud that did not appear. (Syifa et al., 2019) used the AI classifications to differentiate the flood area from other land cover types, that could be negatively influenced by the input source data. Differently from (Syifa et al., 2019), we considered for our study a longer time interval (2019, 2020, 2021), and we used the specific spectral signatures of exposed materials (Figures 6.5). With this study, four areas were selected within the mining district, based on the ferric oxides impact. Considering that the images were acquired during the months of January, August, and July, the general decrease of the vegetation cover in the district from 2019 to 2021, could be associated with the seasons. However, the influence of ferric oxides related to the dam collapse doesn't depend on the seasonal vegetation rate. Figures 6.5 displays the mean spectral signatures, extracted in the selected zones, as a function of the wavelength band of the satellite. It is possible to notice that, still one year after the dam failure, the influence of ferric oxides is well defined in all the spectra (Figure 6.5b), where it is possible to note the ferric oxides absorption feature centered in 833 nm. In 2021 the ferric oxides impact continues to be highlighted by a weak absorption. Spectra collected in the river bed (Figure 6.5A) are characterized by spectral properties which

may be associated with water turbidity in the visible region. According to Gholizadeh et al. 2016 the effects of turbidity, due to suspended particles in surface waters, occur in the band range between 700 and 800 nm. Indeed, in 2019 it is possible to note a reflectance maximum at the same wavelength values, diagnostic of turbidity. While in 2020 and 2021 it is notable the ferric oxides absorption (Figure 6.5B, C), thus suggesting that waste material still occurs in the river. According to Fang et al. 2018 the clay minerals in soils show diagnostic absorptions features in the shortwave-infrared domain (SWIR), and their reflectance spectra exhibit OH-H₂O-related absorptions approximately around 1400 nm and 1900 nm, and Al-OH absorption near 2200 nm, the latter covered by Sentinel-2 in band 12 (2100–2280 nm) (Sekandari et al., 2020). In Figure 6.5 the signatures obtained in 2020 and 2021 show a spectral absorption feature in the SWIR region, which may be related to clay minerals occurring in the waste material. Indeed, the latter could be associated with the presence of kaolinite composing the silty-clayey fractions of the tailing dam material that after the failure moved in the flood and affected the surrounding areas. This observation is consistent with the mineralogical and geochemical composition of the tailing dam materials, discussed in previous studies on the Córrego do Feijão mine (Vergilio et al., 2020) and other tailing dams in the Quadrilatero Ferrifero area (Fundão Dam, Samarco mining company) (Thompson et al., 2020, Almeida et al., 2018). According to Almeida et al. 2018, hematite occurs as the main phase in the mine waste of the Fundão Dam, followed by goethite, kaolinite and, gibbsite, in line with Vergilio et al. 2020, which observed Fe concentrations up to 26.5 wt.% and Al up to 1.1 wt%, for the fine waste material of the Córrego do Feijão mine. As Sentinel-2 cannot accurately detect the clay mineral content due to the low spectral resolution in the SWIR region, it didn't allow to use of this observation to produce specific clay distribution maps.

6.7. Conclusions

In this paper, a multispectral approach was used to determine affected areas by the flood generated after the dam collapse. Starting from the spectral analysis and using the SNAP tool, the absorption features of the mining products, vegetation and water were recognized, and land cover maps were produced. The methodology uses a linear approach to obtain rapidly RGB composite maps useful to detect the flood-affected zones. The multispectral bands of the Sentinel-2 data have proved to be an extremely useful tool for mapping flooded areas. The method allows obtaining significant information potentially useful for monitoring lands affected by floods related to tailing dam collapse and planning the post activities management. To support the study and better examine the environmental impact, as essentially as possible, might be necessary to carry out a soils sampling of the flood-affected zones.

7. Discussions and conclusions

The considerable presence of worldwide-mining activities, although ensuring a continuous and fundamental supply of mineral resources, could have various negative environmental consequences. The mining activities generally can cause several geohazards (Yidana et al., 2008; Altun et al., 2010; Armah et al., 2010; Yang et al., 2020). Regardless of the progress of new technologies and security measures, we find ourselves still in situations of geological and geomorphological problems. Consequently, Earth Observation methods can be essential for mining monitoring, mechanism interpretation, and its related geohazard assessment. This thesis highlights the importance of the combination of remote sensing methods for the development of tools allowing to identify critical situations in a near-real-time or in advance and to minimize on a large scale the time needed for mining monitoring.

It is worth pointing out that a typical underground mining project follows a series of significant technical phases from planning mining to the final mine reclamation, which can be summarized in an initial development stage, that precedes the exploitation activity, which is finally followed by post-mining work. The methods developed in this thesis proved to be useful applications during the several stages of a typical underground mining operation. Specifically, in the first and second study cases, two areas affected by different types of underground mining were monitored by using the DInSAR technology that was effective for detecting the ground surface deformations. The first case regarded the Zaruma area (Ecuador), where the interferometric technique allowed to monitor urban mining areas characterized by unauthorized excavating activity that induced damage to structures. In this case, the identified subsidence events are very dangerous because excavation is carried out illegally producing unexpected sinkholes (Gutiérrez et al., 2014; Parise et al., 2015; Gee et al., 2017; Fazio et al., 2017), as it was reported near the “La Immaculada de Fe y alegría” school (Ludizaca et al., 2018; Cando et al., 2020). The horizontal and vertical components of deformations measured in selected unstable areas (called UA, chapter 3.5) varied between 2.0 and 6.0 cm. The vertical component is commonly predominant over the horizontal component, clearly indicating the occurrence of subsidence phenomena.

In the second study case, the DinSAR techniques allow detecting ground surface deformations that occurred in an area interested by underground mining in the Nuraxi

Figus coal district (Italy). The subsidence recognized in Nuraxi Figus area started in 2011 in correspondence of two panels where coal seams were mined at a depth of 450 m below the surface and was characterized by three subsidence phases: initial, principal, residual (Cui et al. 2000, Al Heib et al. 2005, Cui et al. 2020, Tajduš et al. 2021). The maximum cumulated vertical displacements were of ca. 26 cm in 2020. It is important to note that during the coal extraction between 2011 and 2012, the subsidence reported the major displacement as a horizontal component. While during the post-mining operations the vertical displacement increased respect to the horizontal components, reaching the maximum values with temporal delay respect to the end of excavation activity. According to Al Heib et al. (2005), various coal mining districts are characterized by temporal delays in the occurrence of maximum surface deformation. The residual subsidence continues after the extraction and in some cases can occur after some months or years (Huang et al., 2020, Cui et al., 2020, Modeste et al., 2021).

It is important to note that in Zaruma study case, the residual subsidence is not present and the vertical time series is more linear than the Nuraxi Figus study case. One of UA's is developed in a sinkhole which generated the collapse of the “La Inmaculada de Fe y alegría” school (Chapter 3.7). The absence of residual subsidence can be associated with shallower mining activity. Therefore, in presence of shallow and very surficial underground mining activity, the monitoring method used in this thesis can be only useful for monitoring initial excavation phases, allowing to identify unstable areas that could be possibly interested in future sinkholes. In presence of deep underground mining, instead, it is possible to apply the method in all mining phases, identifying and monitoring the subsidence during the extraction, and studying its evolution after the end of mining activities. Additionally, the method was tested for monitoring other infrastructures occurring in mining sites, such as tailings dams, which are often in unstable conditions and can be affected by collapses (Azam et al. 2010; Kossoff et al. 2014, WISE www.wise-uranium.org/mdaf.html). The designated study area was the Brumadinho district (Brazil), where on 25 January 2019 a tailings dam collapsed, generating a catastrophic flood that caused deaths and serious environmental pollution (Vergilio et al., 2020; Thompson et al., 2020). Specifically, an integrated approach of satellite radar data and multispectral data was used to investigate possible deformations occurring in the tailing dam before the collapse, and to characterize the

environmental effects occurred after the flooding. According to Furlan et al. (2020) heavy metals, including iron, aluminum, and manganese still occur with values above the acceptable in the flood-affected areas. The Sentinel-1 dataset allowed identifying maximum LoS cumulated displacement of -3.66 cm, detected in correspondence of the center of the dam. The ground surface movements started in 2017 and developed eight days before the disaster. Integrating this information with rainfall data, it was possible to notice an anomaly of rainfalls that could have triggered the event, producing an increase in the displacement rate. The environmental impact of the Brumadinho flood on the surrounding lands was studied by using the Sentinel-2 data and spectral properties of materials occurring in the area. Four distinct areas that were affected by the flood and were located at various kilometers from the dam, were selected for remote sensing spectral analysis. The investigation allowed to detect the presence in the soils of tailing dam materials (mostly Fe-oxy-hydroxides) still two years after the dam failure. This study demonstrates that the capability of combining both Sentinel-1 and Sentinel-2 data, with the addition of ancillary data (like rainfalls dataset, spectral information, etc.) can be strategic for monitoring tailings dams. It was possible to realize the monitoring and assessment of pre-collapse surface deformations and also to quickly determine the soil pollution at various times after the dam collapse. In conclusion, the methodology developed in this Ph.D. thesis could be effectively used to monitor mining areas and communicate the results in near time, allowing fact-based discussions and being of support to managing the pre- and post-mining activities. Future perspectives could be the development of an automated software able to manage the data from EO techniques integrated with other information that will provide support for mining stakeholders.

References

- Aamir, M., Ali, T., Irfan, M., Shaf, A., Azam, M. Z., Glowacz, A., Brumerick, F., Glowacz, W., Alqhtani, S., and Rahman, S., 2021, Natural Disasters Intensity Analysis and Classification Based on Multispectral Images Using Multi-Layered Deep Convolutional Neural Network: *Sensors*, v. 21, p. 2648.
- Abdallah, M.; Verdel, T. Behavior of a masonry wall subjected to mining subsidence, as analyzed by experimental designs and response surfaces. *Int. J. Rock Mech. Min. Sci.* 2017, 100, 199–206.
- Adam, E., Mutanga, O., and Rugege, D., 2010, Multispectral and hyperspectral remote sensing for identification and mapping of wetland vegetation: a review: *Wetlands Ecology and Management*, v. 18, p. 281–296.
- Akcin, H. (2021). A GIS-based building risk assessment for the subsidence due to undercity coal mining activities in Zonguldak, Turkey. *Arabian Journal of Geosciences*, 14(5), 1-13.
- Al Heib, M. Nicolas, J. F. Noirel, and Francis Wojtkowiak. "Residual subsidence analysis after the end of coal mine work. Example from Lorraine colliery, France. (2005)
- Al Heib, M., Linkov, A. M., & Zoubkov, V. V. (2001). On numerical modeling of subsidence induced by mining. In *International symposium of the international society for rock mechanics (EUROCK 2001)*.
- Alkmim, F. F., and Marshak, S., 1998, Transamazonian Orogeny in the Southern São Francisco Craton Region, Minas Gerais, Brazil: evidence for Paleoproterozoic collision and collapse in the Quadrilátero Ferrífero: *Precambrian Research*, v. 90, p. 29–58.
- Almeida, C. A., Oliveira, A. F. de, Pacheco, A. A., Lopes, R. P., Neves, A. A., and Lopes Ribeiro de Queiroz, M. E., 2018, Characterization and evaluation of sorption potential of the iron mine waste after Samarco dam disaster in Doce River basin – Brazil: *Chemosphere*, v. 209, p. 411–420.
- Ammirati, L., Mondillo, N., Calcaterra, D., and Di Martire, D., 2021, Sentinel-1 Data for Monitoring a Pre-failure Event of Tailings Dam, in Rizzo, P. and Milazzo, A. eds., *European Workshop on Structural Health Monitoring: Cham, Springer International Publishing*, p. 140–148.
- Ammirati, L., Mondillo, N., Rodas, R.A., Sellers, C., Di Martire, D.: Monitoring Land Surface Deformation Associated with Gold Artisanal Mining in the Zaruma City (Ecuador). *Remote Sensing*. 12, 2135 (2020).
- Antonielli, B., Sciortino, A., Scancella, S., Bozzano, F., & Mazzanti, P. (2021). Tracking Deformation Processes at the Legnica Glogow Copper District (Poland) by Satellite InSAR—I: Room and Pillar Mine District. *Land*, 10(6), 1-20.
- ARCOM Realizó en 5 Meses 150 Colapsos Mineros en la Zona de Exclusión de Zaruma. Available online: <http://www.controlminero.gob.ec/arcom-realizo-en-5-meses-150-colapsos-mineros-en-la-zona-de-exclusion-de-zaruma>. (accessed on 11 May 2020).
- Ardau, F.; Balia, R.; Bianco, M.; De Waele, J. Assessment of cover-collapse sinkholes in SW Sardinia (Italy). *Geol. Soc.* 2007, 279, 47–57. .
- Armah A.F., S. Obiri, D.O. Yawson, A.N.M. Pappoe, B. Akoto. Mining and heavy metal pollution: assessment of aquatic environments in Tarkwa (Ghana) using multivariate statistical analysis. *Journal of Environmental Statistics*, 14 (2010), pp. 1-13
- Artisanal and Small-Scale Gold Mining. Available online: www.gold.org/goldmining/responsible-mining/artisanal-and-small-scale-mining (accessed on 11 May 2020).
- Artisanal Mining: The Dangers that Come with the Job. Available online: <https://www.mining-technology.com/features/artisanal-mining-the-danger-that-come-with-the-job> (accessed on 11 May 2020).
- Asner, G.P., 1998, Biophysical and Biochemical Sources of Variability in Canopy Reflectance, *Remote Sensing of Environment*, 64:234-253.
- Assorgia A., Cincotti F., Fadda A., Gimeno D., Morra V., Ottelli L., Secchi F.A., (1992). Il complesso comenditico miocenico dell'entroterra sulcitano (Sardegna sud-occidentale). Caratteri geologici, vulcanologici e petrochimici. *Boll. Serv. Geol. It., Sp. Issue*, pp. 292-303. (in italian)
- Assorgia A., Fadda A., Gimeno Torrente D., Morra V., Ottelli L., Secchi F.A., (1990). Le Successioni ignimbriche terziarie del Sulcis (Sardegna sud-occidentale). *Mem. Soc. Geol. It.*, 45, pp. 951-963. (in italian).

- Assorgia, A., Fadda, A., Gimeno, D., Morra, V., Ottelli, L., Pujolriu, L. & Secchi, F. A. 1992b. Tectono-sedimentary evolution of the Upper Tertiary volcanic succession of Sulcis area (SW Sardinia, Italy). *Paleontologia i Evolució* 24–25, 307–20
- Azam, S., & Li, Q. Tailings dam failures: a review of the last one hundred years. *Geotechnical news*, 28(4), 50-54 (2010).
- Babinski, M., Chemale, F., and Van Schmus, W. R., 1995, The Pb/Pb age of the Minas Supergroup carbonate rocks, Quadrilátero Ferrífero, Brazil: *Precambrian Research*, v. 72, p. 235–245.
- Baek, W.K. and Jung, H.S., 2019. A review of change detection techniques using multi-temporal synthetic aperture radar images. *Korean Journal of Remote Sensing*, 35(5_1), pp.737-750.
- Baldock, J. *Geology of Ecuador: Explanatory Bulletin of the National Geological Map of the Republic of Ecuador 1:100,000 Scale 1982; Technical Report; Ministerio de Recursos Naturales y Energéticos: San Francisco, Costa Rica, 1982.*
- Baltazar, O. F., and Zucchetti, M., 2007, Lithofacies associations and structural evolution of the Archean Rio das Velhas greenstone belt, Quadrilátero Ferrífero, Brazil: A review of the setting of gold deposits: *Ore Geology Reviews*, v. 32, p. 471–499.
- Barca, S. & Costamagna, Luca Giacomo. (2000). Il bacino paleogenico del Sulcis-Iglesiente (Sardegna SW): nuovi dati stratigrafico-strutturali per un modello geodinamico nell'ambito dell'orogenesi pirenaica. *Boll. Soc. Geol. It.* 119. 497-515.
- Bedell, R., 2004. Remote sensing in mineral exploration. *SEG Discovery*, (58), pp.1-14.
- Bell, F.; Stacey, T.; Genske, D. Mining subsidence and its effect on the environment: Some differing examples. *Environ. Geol.* 2000, 40, 135–152. .
- Bell, F.G., Donnelly, L.J., Genske, D.D. et al. Unusual cases of mining subsidence from Great Britain, Germany and Colombia. *Environ Geol* 47, 620–631 (2005).
- Berardino, P., Fornaro, G., Lanari, R., Sansosti, E. (2002). A new Algorithm for Surface Deformation Monitoring based on Small Baseline Differential SAR Interferograms. *IEEE Transactions on Geoscience and Remote Sensing*, 40(11), 2375-2383.
- Bieniawski, Z. T. (1989). *Engineering rock mass classifications: a complete manual for engineers and geologists in mining, civil, and petroleum engineering.* Wiley-Interscience. pp. 40–47
- Billingsley, P. *Geology of the Zaruma gold district of Ecuador.* *Am. Inst. Min. Metall. Eng.* 1926, 74, 255–275.
- Blanco, P., Mallorquí, J.J., Duque, S. and Monells, D. (2008). The Coherent Pixels Technique (CPT): an Advanced DInSAR Technique for Non-linear Deformation Monitoring. *Pure and Applied Geophysics*, 165 (6), 1167-1193.
- Bonì, R.; Pilla, G.; Meisina, C. Methodology for detection and interpretation of ground motion areas with the A-DInSAR time series analysis. *Remote Sens.* 2016, 8, 686. .
- Bozzano, F.; Cipriani, I.; Mazzanti, P.; Prestininzi, A. Displacement patterns of a landslide affected by human activities: insights from ground-based InSAR monitoring. *Natural Hazards* 2011, 59, 1377–1396, doi:10.1007/s11069-011-9840-6.
- Brinkgreve, R. B. J., W. Broere, and D. Waterman. "Plaxis: finite element code for soil and rock analyses: 2D-version 8. User's manual." (2008).
- Bürgmann, R.; Rosen, P.A.; Fielding, E.J. Synthetic aperture Radar interferometry to measure Earth's surface topography and its deformation. *Annu. Rev. Earth Planet. Sci.* 2000, 28, 169–209.
- Cabral, A. R., Zeh, A., Koglin, N., Gomes Jr, A. A. S., Viana, D. J., and Lehmann, B., 2012, Dating the Itabira iron formation, Quadrilátero Ferrífero of Minas Gerais, Brazil, at 2.65 Ga: depositional U–Pb age of zircon from a metavolcanic layer: *Precambrian Research*, v. 204, p. 40–45.
- Cando Jácome, M.; Martínez-Graña, A.M.; Valdés, V. Detection of Terrain Deformations Using InSAR Techniques in Relation to Results on Terrain Subsidence (Ciudad de Zaruma, Ecuador). *Remote Sens.* 2020, 12, 1598. .
- Carlà, T., Farina, P., Intrieri, E., Ketizmen, H., Casagli, N., 2018. Integration of ground-based radar and satellite InSAR data for the analysis of an unexpected slope failure in an open-pit mine. *Engineering Geology* 235, 39–52.
- Carlà, T.; Intrieri, E.; Raspini, F.; Bardi, F.; Farina, P.; Ferretti, A.; Colombo, D.; Novali, F.; Casagli, N. Perspectives on the prediction of catastrophic slope failures from satellite InSAR. *Scientific Reports* 2019, 9, doi:10.1038/s41598-019-50792-y.

- Casagli, N., Frodella, W., Morelli, S., Tofani, V., Ciampalini, A., Intrieri, E., Raspini, F., Rossi, G., Tanteri, L. and Lu, P., 2017. Spaceborne, UAV and ground-based remote sensing techniques for landslide mapping, monitoring and early warning. *Geoenvironmental Disasters*, 4(1), pp.1-23.
- Cascini, L.; Fornaro, G.; Peduto, D. Advanced low-and full-resolution DInSAR map generation for slow-moving landslide analysis at different scales. *Eng. Geol.* 2010, 112, 29–42. .
- Casu, F., Bonano, M., Castaldo, R., De Luca, C., De Novellis, V., Lanari, R., ... & Zinno, I. (2019, July). Monitoring Volcano Deformation from Space with Sentinel-1 Data for Civil Protection. In *IGARSS 2019-2019 IEEE International Geoscience and Remote Sensing Symposium* (pp. 9303-9306). IEEE.
- Centro Nacional de Monitoramento e Alertas de Desastres Naturais. Available: <http://www.cemaden.gov.br>. Accessed: 04/07/2020.
- Chemale, F., Rosière, C. A., and Endo, I., 1994, The tectonic evolution of the Quadrilátero Ferrífero, Minas Gerais, Brazil: *Precambrian Research*, v. 65, p. 25–54.
- Chen, B., Mei, H., Li, Z., Wang, Z., Yu, Y., & Yu, H. (2021). Retrieving three-dimensional large surface displacements in coal mining areas by combining SAR pixel offset measurements with an improved mining subsidence model. *Remote Sensing*, 13(13), 2541.
- Chiaradia, M.; Fontboté, L.; Beate, B. Cenozoic continental arc magmatism and associated mineralization in Ecuador. *Miner. Dep.* 2004, 39, 204–222. .
- Chronology of major tailings dam failures, (<https://www.wise-uranium.org/mdaf.html>).
- Cigna, F.; Confuorto, P.; Novellino, A.; Tapete, D.; Di Martire, D.; Ramondini, M.; Calcaterra, D.; Plank, S.; Ietto, F.; Brigante, A.; et al. 25 years of satellite InSAR monitoring of ground instability and coastal geohazards in the archaeological site of Capo Colonna, Italy. In *Proceedings of the SPIE 10003, SAR Image Analysis, Modeling, and Techniques XVI*, Edinburgh, UK, 18 October 2016. .
- Colesanti, C.; Wasowski, J. Investigating landslides with space-borne Synthetic Aperture Radar (SAR) interferometry. *Eng. Geol.* 2006, 88, 173–199. .
- Costantini M., S. Falco, F. Malvarosa, F. Minati, “A new method for identification and analysis of persistent scatterers in series of SAR images,” in *Proc. Int. Geosci. Remote Sensing Symp. (IGARSS)*, Boston MA, USA, 7-11 July 2008, pp. 449-452.
- Costantini M., Ferretti A., Minati F., Falco S., Trillo F., Colombo D., Novali F., Malvarosa F., Mammone F., Vecchioli F., Rucci A., Fumagalli A., Allievi J., Ciminelli M.G. and Costabile S.; 2017: Analysis of surface deformations over the whole Italian territory by interferometric processing of ERS, Envisat and COSMO-SkyMed radar data. *Remote Sensing Environ.*
- Costantini, M., Iodice, A., Magnapane, L., Pietranera, L. (2000). Monitoring terrain movements by means of sparse SAR differential interferometric measurements. In *Geoscience and Remote Sensing Symposium, 2000. Proceedings. IGARSS 2000. IEEE 2000 International*, 7, 3225-3227.
- Crosetto, M., Biescas, E., Duro, J., Closa, J., Arnaud, A. (2008). Generation of Advanced ERS and Envisat Interferometric SAR Products Using the Stable Point Network Technique. *Photogrammetric Engineering and Remote Sensing*, 74(4), 443-451.
- Crowley, J. K., Williams, D. E., Hammarstrom, J. M., Piatak, N., Chou, I.-M., and Mars, J. C., 2003, Spectral reflectance properties (0.4–2.5 μm) of secondary Fe-oxide, Fe-hydroxide, and Fe-sulphate-hydrate minerals associated with sulphide-bearing mine wastes: *Geochemistry: Exploration, Environment, Analysis*, v. 3, p. 219–228.
- Cudahy, T.J.; Ramanaidou, E.R. Measurement of the Hematite:Goethite Ratio Using Field Visible and Near-infrared Reflectance Spectrometry in Channel Iron Deposits, Western Australia. *Australian Journal of Earth Sciences* 1997, 44, 411–420, doi:10.1080/08120099708728322.
- Cui, X., Zhao, Y., Wang, G., Zhang, B., & Li, C. (2020). Calculation of residual surface subsidence above abandoned longwall coal mining. *Sustainability*, 12(4), 1528.
- Cui, X.; Miao, X.; Wang, J.; Yang, S.; Liu, H.; Song, Y.; Liu, H.; Hu, X. Improved prediction of differential subsidence caused by underground mining. *Int. J. Rock Mech. Min. Sci.* 2000, 37, 615–627.
- Curtiss, B., 1985, Evaluation of the Physical Properties of Naturally Occurring Iron (III) Oxyhydroxides on Rock Surfaces in Arid and Semi-arid Regions Using Visible and Near Infrared Reflectance Spectroscopy:

- Darlington S.; Glanz J.; Andreoni M.; Bloch M.; Peçanha S.; Singhvi S.; Griggs T.: A Tidal Wave of Mud. Available: <https://www.nytimes.com/interactive/2019/02/09/world/americas/brazil-dam-collapse.html>. Accessed: 04/07/2020.
- De Minas Gerais, C. de S., and do Brasil, S. G., 2019, Informativo n° 32-Informativo diário dos parâmetros de qualidade das águas nos locais monitorados ao longo do Rio Paraopeba, após o desastre na barragem B1 no complexo da Mina Córrego Feijão da Mineradora Vale/SA de Brumadinho-Minas Gerais.
- De Novellis, V., Carlino, S., Castaldo, R., Tramelli, A., De Luca, C., Pino, N. A., ... & Tizzani, P. (2018). The 21 August 2017 Ischia (Italy) earthquake source model inferred from seismological, GPS, and DInSAR measurements. *Geophysical Research Letters*, 45(5), 2193-2202.
- Demirel, N.; Emil, M.K.; Duzgun, H.S. Surface coal mine area monitoring using multi-temporal high-resolution satellite imagery. *Int. J. Coal Geol.* 2011, 86, 3–11.
- Di Martire D., De Luca, G., Ramondini, M., Calcaterra, D., 2013. Landslide-Related PS Data Interpretation by Means of Different Techniques. *Landslide Science and Practice* 347–355.
- Di Martire, D.; Iglesias, R.; Monells, D.; Centolanza, G.; Sica, S.; Ramondini, M.; Pagano, L.; Mallorquí, J.J.; Calcaterra, D. Comparison between Differential SAR interferometry and ground measurements data in the displacement monitoring of the earth-dam of Conza della Campania (Italy). *Remote Sens. Environ.* 148, 58–69. (2014).
- Di Martire, D.; Tessitore, S.; Brancato, D.; Ciminelli, M.G.; Costabile, S.; Costantini, M.; Graziano, G.V.; Minati, F.; Ramondini, M.; Calcaterra, D. Landslide detection integrated system (LaDIS) based on in-situ and satellite SAR interferometry measurements. *Catena* 2016, 137, 406–421. .
- Dong S, Yin H, Yao S, Zhang F. Detecting surface subsidence in coal mining area based on DInSAR technique. *Journal of Earth Science.* 2013;24(3):449-456. doi:10.1007/s12583-013-0342-1.
- Dong, S., Samsonov, S., Yin, H., Yao, S. and Xu, C., 2015. Spatio-temporal analysis of ground subsidence due to underground coal mining in Huainan coalfield, China. *Environmental Earth Sciences*, 73(9), pp.5523-5534.
- Dorr, J. V. N., 1969, Physiographic, stratigraphic, and structural development of the Quadrilatero Ferrífero, Minas Gerais, Brazil, (<https://pubs.er.usgs.gov/publication/pp641A>).
- Doxaran, D.; Froidefond, J.-M.; Lavender, S.; Castaing, P. Spectral Signature of Highly Turbid Waters: Application with SPOT Data to Quantify Suspended Particulate Matter Concentrations. *Remote Sensing of Environment* 2002, 81, 149–161, doi:10.1016/S0034-4257(01)00341-8.
- Du Z., Ge L., Ng A.N.G., Zhu O., Horgan O., Zhang O.: Risk assessment for tailings dams in Brumadinho of Brazil using InSAR time series approach. *Science of The Total Environment* (2020).
- Du, Z.; Ge, L.; Li, X.; Ng, A.H.M. Subsidence monitoring over the Southern Coalfield, Australia using both L-Band and C-Band SAR time series analysis. *Remote Sens.* 2016, 8, 543.
- El Kamali, M., Abuelgasim, A., Papoutsis, I., Loupasakis, C. and Kontoes, C., 2020. A reasoned bibliography on SAR interferometry applications and outlook on big interferometric data processing. *Remote Sensing Applications: Society and Environment*, p.100358.
- En Zaruma Piden la Reapertura de su Hospital, Cerrado Hace Cinco Meses. Available online: <https://www.elcomercio.com/actualidad/zaruma-reapertura-hospital-mineria-sismo.html> (accessed on 13 May 2020).
- European Space Agency—ESA, Sentinels Scientific Data Hub. Available online: <https://scihub.copernicus.eu> (accessed on 13 May 2020).
- Explotación Minera y Mala Planificación Urbana son los dos Riesgos de Zaruma. Available online: <https://www.elcomercio.com/actualidad/zaruma-mineria-legal-planificacion-urbana-secretariadegestionderiesgos-eloro.html> (accessed on 13 May 2020).
- F.D. van der Meer, H.M.A. van der Werff, and F.J.A. van Ruitenbeek, 2014, Potential of ESA's Sentinel-2 for geological applications: *Remote sensing of environment*, v. 148, p. 124–133.
- Fadda, A., Ottelli, L., & Perna, G. (1994). *Il Bacino lignitifero del Sulcis: Geologia, Idrogeologia, Miniere*. Cagliari: Carbosulcis S.p.A.
- Fan H, Gao X, Yang J, Deng K, Yu Y.: Monitoring Mining Subsidence Using A Combination of Phase-Stacking and Offset-Tracking Methods. *Remote Sensing* (2015).

- Fang, Q., Hong, H., Zhao, L., Kukulich, S., Yin, K., and Wang, C., 2018, Visible and Near-Infrared Reflectance Spectroscopy for Investigating Soil Mineralogy: A Review: *Journal of Spectroscopy*, v. 2018, p. e3168974.
- Fazio, N.L.; Perrotti, M.; Lollino, P.; Parise, M.; Vattano, M.; Madonia, G.; Di Maggio, C. A three-dimensional back-analysis of the collapse of an underground cavity in soft rocks. *Eng. Geol.* 2017, 228, 301–311. .
- Ferretti, A., Fumagalli, A., Novali, F., Prati, C., Rocca, F., Rucci, A. (2011). A new algorithm for processing interferometric data-stacks: SqueeSAR. *IEEE Transactions on Geoscience and Remote Sensing*, 49(9), 3460-3470.
- Ferretti, A., Prati, C., Rocca, F. (2000). Nonlinear subsidence rate estimation using permanent scatterers in differential SAR interferometry. *IEEE Transactions on Geoscience and Remote Sensing*, 38 (5), 2202-2212.
- Ferretti, A., Prati, C., Rocca, F. (2001). Permanent scatterers in SAR interferometry. *IEEE Transactions on Geoscience and Remote Sensing* 39(1), 8-20.
- Ferretti, A., Savio, G., Barzaghi, R., Borghi, A., Musazzi, S., Novali, F., Prati, C., Rocca, F. (2007) Sub-millimeter Accuracy of InSAR Time Series: Experimental Validation. *IEEE Transactions On Geoscience And Remote Sensing*, 45, 5.
- Fiaschi, S.; Tessitore, S.; Bonì, R.; Di Martire, D.; Achilli, V.; Borgstrom, S.; Ibrahim, A.; Floris, M.; Meisina, C.; Ramondini, M.; et al. From ERS-1/2 to Sentinel-1: Two decades of subsidence monitored through A-DInSAR techniques in the Ravenna area (Italy). *GISci. Remote Sens.* 2017, 54, 305–328. .
- Foumelis, M., Papageorgiou, E., & Stamatopoulos, C. (2016). Episodic ground deformation signals in Thessaly Plain (Greece) revealed by data mining of SAR interferometry time series. *International Journal of Remote Sensing*, 37(16), 3696-3711.
- Franceschetti G., Migliaccio M., Riccio D. & Schirinzi G. (1992) - Saras: a synthetic aper-ture radar (SAR) raw signal simulator. *IEEE Trans. Geosci. Remote Sens.*, 30, 110–123.
- Franceschetti, G.; Lanari, R. *Synthetic Aperture Radar Processing*; CRC Press: Boca Raton, FL, USA, 1999.
- Furlan, J. P. R., dos Santos, L. D. R., Moretto, J. A. S., Ramos, M. S., Gallo, I. F. L., Alves, G. de A. D., Paulelli, A. C., Rocha, C. C. de S., Cesila, C. A., Gallimberti, M., Devóz, P. P., Júnior, F. B., and Stehling, E. G., 2020, Occurrence and abundance of clinically relevant antimicrobial resistance genes in environmental samples after the Brumadinho dam disaster, Brazil: *Science of The Total Environment*, v. 726, p. 138100.
- Gabriel, A. K., Goldstein, R. M., & Zebker, H. A. (1989). Mapping small elevation changes over large areas: Differential radar interferometry. *Journal of Geophysical Research: Solid Earth*, 94(B7), 9183-9191.
- GAD ZARUMA on Twitter: “Colapsó Aula afecta por Hundimiento en la Escuela La Inmaculada. Available online: <https://twitter.com/gadzaruma/status/815997958059655168> (accessed on 13 May 2020).
- Gama, F.F., Paradella, W.R., Mura, J.C., de Oliveira, C.G., 2019. Advanced DINSAR analysis on dam stability monitoring: A case study in the Germano mining complex (Mariana, Brazil) with SBAS and PSI techniques. *Remote Sensing Applications: Society and Environment* 16, 100267.
- Gazzola, L., Ferronato, M., Frigo, M., Janna, C., Teatini, P., Zoccarato, C., Antonelli, M., Corradi, A., Dacome, M.C. and Mantica, S., 2021. A novel methodological approach for land subsidence prediction through data assimilation techniques. *Computational Geosciences*, 25(5), pp.1731-1750.
- Ge, W., Cheng, Q., Jing, L., Wang, F., Zhao, M., and Ding, H., 2020, Assessment of the Capability of Sentinel-2 Imagery for Iron-Bearing Minerals Mapping: A Case Study in the Cuprite Area, Nevada: *Remote Sensing*, v. 12, p. 3028.

- Gee, D.; Bateson, L.; Sowter, A.; Grebby, S.; Novellino, A.; Cigna, F.; Marsh, S.; Banton, C.; Wyatt, L. Ground motion in areas of abandoned mining: Application of the intermittent SBAS (ISBAS) to the Northumberland and Durham Coalfield, UK. *Geosciences* 2017, 7, 85. .
- Giardina, G., Milillo, P., DeJong, M. J., Perissin, D., & Milillo, G. (2019). Evaluation of InSAR monitoring data for post-tunnelling settlement damage assessment. *Structural Control and Health Monitoring*, 26(2), e2285.
- Gholizadeh, M.H.; Melesse, A.M.; Reddi, L. A Comprehensive Review on Water Quality Parameters Estimation Using Remote Sensing Techniques. *Sensors* 2016, 16, 1298, doi:10.3390/s16081298.
- Gläßer, C., and Reinartz, P., 2005, Multitemporal and Multispectral Remote Sensing Approach for Flood Detection in the Elbe-Mulde Region 2002: *Acta hydrochimica et hydrobiologica*, v. 33, p. 395–403.
- Gobierno Nacional Presentará el Plan Zaruma—Portovelo 2022. Available online: <http://www.controlminero.gob.ec/gobierno-nacional-presentara-el-plan-zaruma-portovelo-2022> (accessed on 11 May 2020).
- González, A.O.O.; Pozo, A.F.R.; Amaya, R.J.G. Inestabilidad del terreno en zonas de actividad minera: Caso ciudad de Zaruma Ecuador. *Redes De Ing.* 2017, 8, 69–81. .
- Grzovic, M. and Ghulam, A., 2015. Evaluation of land subsidence from underground coal mining using TimeSAR (SBAS and PSI) in Springfield, Illinois, USA. *Natural Hazards*, 79(3), pp.1739-1751.
- Guéguen, Y.; Deffontaines, B.; Fruneau, B. Monitoring residual mining subsidence of Nord/Pas-de-Calais coal basin from differential and Persistent Scatterer Interferometry (Northern France). *J. Appl. Geophys.* 2009, 69, 24–34
- Guerriero, L., Confuorto, P., Calcaterra, D., Guadagno, F. M., Revellino, P., & Di Martire, D. (2019). PS-driven inventory of town-damaging landslides in the Benevento, Avellino and Salerno Provinces, southern Italy. *Journal of Maps*, 15(2), 619–625.
- Guild, P. W., 1953, Iron deposits of the Congonhas District, Minas Gerais, Brazil: *Economic Geology*, v. 48, p. 639–676.
- Guimarães, D., 1935, Contribuição ao estudo da origem dos depositos de minerio de ferro e manganez do centro de Minas Geraes:
- Guo H, Yuan L, Shen BT, Qu QD, Xue JH (2012) Mining-induced strata stress changes, fractures and gas flow dynamics in multi-seam long wall mining. *Int J Rock Mech Min Sci* 54:129–139
- Gutiérrez, F. Sinkhole hazards. In *Oxford Research Encyclopedia of Natural Hazard Science*; 2016; pp. 1–92. <http://oxfordre.com/naturalhazardscience/view/10.1093/acrefore/9780199389407.001.0001/acrefore-9780199389407-e-40?print=pdf> (accessed on 13 May 2020).
- Gutiérrez, F.; Parise, M.; De Waele, J.; Jourde, H. A review on natural and human-induced geohazards and impacts in karst. *Earth-Sci. Rev.* 2014, 138, 61–88. .
- Hedenquist, J.W.; Arribas, A.R.; Gonzalez-Urien, E. Exploration for epithermal gold deposits. *Rev. Econ. Geol.* 2000, 13, 45–77.
- Hensler, A.-S., Hagemann, S. G., Rosière, C. A., Angerer, T., and Gilbert, S., 2015, Hydrothermal and metamorphic fluid-rock interaction associated with hypogene “hard” iron ore mineralisation in the Quadrilátero Ferrífero, Brazil: Implications from in-situ laser ablation ICP-MS iron oxide chemistry: *Ore Geology Reviews*, v. 69, p. 325–351.
- Hensler, A.-S., Rosière, C. A., and Hagemann, S. G., 2017, Iron Oxide Mineralization at the Contact Zone Between Phyllite and Itabirite of the Pau Branco Deposit, Quadrilátero Ferrífero, Brazil—Implications for Fluid-Rock Interaction During Iron Ore Formation: *Economic Geology*, v. 112, p. 941–982.
- Herz, N., 1978, metamorphic rocks of the quadrilatero ferrifero, Minas Gerais, Brazil.
- Ho Tong Minh, D., Hanssen, R. and Rocca, F., 2020. Radar interferometry: 20 years of development in time series techniques and future perspectives. *Remote Sensing*, 12(9), p.1364.
- Holden, D, Donegan, S & Pon, A 2020, 'Brumadinho Dam InSAR study: analysis of TerraSAR-X, COSMO-SkyMed and Sentinel-1 images preceding the collapse', in PM Dight (ed.), *Proceedings of the 2020 International Symposium on Slope Stability in Open Pit Mining and Civil Engineering*,

- Australian Centre for Geomechanics, Perth, pp. 293-306, https://doi.org/10.36487/ACG_repo/2025_15
- Holla, L., Barclay, E., 2000. Mine Subsidence in the Southern Coalfield, NSW, Australia. Sydney, New South Wales Department of Mineral Resources.
- Huang, C., Li, Q., & Tian, S. (2020). Research on prediction of residual deformation in goaf of steeply inclined extra-thick coal seam. *Plos one*, 15(10), e0240428.
- Iannacone, J. P., Lato, M., Troncoso, J., & Perissin, D. (2018, July). InSAR monitoring of active, inactive and abandoned tailings facilities. In *Proceedings of the 5th International Seminar on Tailings Management, Santiago, Chile* (pp. 11-13). *IEEE Trans. Geosci. Remote Sens.* 2006, 44, 2861–2870.
- Iglesias, R.; Mallorqui, J.J.; Monells, D.; López-Martínez, C.; Fabregas, X.; Aguasca, A.; Gili, J.A.; Corominas, J. PSI deformation map retrieval by means of temporal sublook coherence on reduced sets of SAR images. *Remote Sens.* 7, 530–563 (2015).
- Intrieri, E.; Fontanelli, K.; Bardi, F.; Marini, F.; Carlà, T.; Pazzi, V.; Fanti, R. Definition of sinkhole triggers and susceptibility based on hydrogeomorphological analyses. *Environ. Earth Sci.* 2018.
- Ismaya F., J. Donovan, Applications of DInSAR for Measuring Mine-Induced Subsidence and Constraining Ground Deformation Model, *GeoCongress 2012*. (2012).
- JARS, 1993. Remote Sensing Note. Japan Association on Remote Sensing
- Jing Z., J. Wang, Y. Zhu, Y. Feng, Effects of land subsidence resulted from coal mining on soil nutrient distributions in a loess area of China, *Journal of Cleaner Production*. 177 (2018) 350–361.
- Kasmaeeyazdi, S., Braga, R., Tinti, F., and Mandanici, E., 2022, Mapping Bauxite Mining Residues Using Remote Sensing Techniques: *Materials Proceedings*, v. 5, p. 91.
- Keshava, N.; Mustard, J.F. Spectral Unmixing. *IEEE Signal Processing Magazine* 2002, 19, 44–57, doi:10.1109/79.974727.
- Klein, C., and Ladeira, E. A., 2000, *Geochemistry and Petrology of Some Proterozoic Banded Iron-Formations of the Quadrilátero Ferrífero, Minas Gerais, Brazil: Economic Geology*, v. 95, p. 405–427.
- Kokaly, R. F., Clark, R. N., Swayze, G. A., Livo, K. E., Hoefen, T. M., Pearson, N. C., Wise, R. A., Benzel, W. M., Lowers, H. A., Driscoll, R. L., and Klein, A. J., 2017, *USGS Spectral Library Version 7: U.S. Geological Survey Data Series 1035*, 68 p., accessed January 21, 2022, at USGS Spectral Library Version 7 at <http://pubs.er.usgs.gov/publication/ds1035>.
- Kossoff, D., Dubbin, W. E., Alfredsson, M., Edwards, S. J., Macklin, M. G., & Hudson-Edwards, K. A. (2014). Mine tailings dams: Characteristics, failure, environmental impacts, and remediation. *Applied Geochemistry*, 51, 229-245.
- Li, J., & Wang, L. (2021). Mining subsidence monitoring model based on BPM-EKTF and TLS and its application in building mining damage assessment. *Environmental Earth Sciences*, 80(11), 1-18.
- Litherland, M. *The Metamorphic Belts of Ecuador*; British Geological Survey: Nottingham, UK, 1994.
- Lobo, F. de L.; Souza-Filho, P.W.M.; Novo, E.M.L. de M.; Carlos, F.M.; Barbosa, C.C.F. Mapping Mining Areas in the Brazilian Amazon Using MSI/Sentinel-2 Imagery (2017). *Remote Sensing* 2018, 10, 1178, doi:10.3390/rs10081178.
- Londoño-Peláez J.M. (2022) Detection of Opencast Mining Sites from Multispectral Satellite Images. In: Rocha Á., Fajardo-Toro C.H., Rodríguez J.M.R. (eds) *Developments and Advances in Defense and Security. Smart Innovation, Systems and Technologies*, vol 255. Springer, Singapore. https://doi.org/10.1007/978-981-16-4884-7_13
- López Gayarre, F.; Álvarez-Fernández, M.I.; González-Nicieza, C.; Álvarez-Vigil, A.E.; Herrera García, G. Forensic analysis of buildings affected by mining subsidence. *Eng. Fail. Anal.* 2010, 17, 270–285.
- Lu, P.; Casagli, N.; Catani, F.; Tofani, V. Persistent Scatterers Interferometry Hotspot and Cluster Analysis (PSI-HCA) for detection of extremely slow-moving landslides. *Int. J. Remote Sens.* 2012, 33, 466–489. .
- Lüders, V., Romer, R. L., Cabral, A. R., Schmidt, C., Banks, D. A., and Schneider, J., 2005, Genesis of itabirite-hosted Au–Pd–Pt-bearing hematite-(quartz) veins, Quadrilátero Ferrífero, Minas Gerais,

- Brazil: constraints from fluid inclusion infrared microthermometry, bulk crush-leach analysis and U–Pb systematics: *Mineralium Deposita*, v. 40, p. 289–306.
- Ludizaca Piedra, E.F.; Ochoa Briones, K.H. Propuesta Para Implementación de un Sistema Integrado de Gestión de Riesgos Por Hundimiento de Suelo en la Zona Urbana del Cantón Zaruma; Trabajo de titulación; Environmental engineering, Universidad Politécnica Salesiana: Cuenca, Ecuador, 2018.
- M. Ji, X. Li, S. Wu, Y. Gao, and L. Ge, “Use of SAR interferometry for monitoring illegal mining activities: a case study at Xishimen iron ore mine,” *Mining Science and Technology (China)*, vol. 21, no. 6, pp. 781–786, 2011.
- Marian, D. P., Onica, I., Marian, R. R., & Floarea, D. A. (2020). Finite element analysis of the state of stresses on the structures of buildings influenced by underground mining of hard coal seams in the jiu valley basin (Romania). *Sustainability*, 12(4), 1598.
- Marschalko, M., Yilmaz, I., Bednárík, M., Kubečka, K., Bouchal, T., Závada, J., 2012. Subsidence map of underground mining influence for urban planning: an example from the Czech Republic. *Quarterly Journal of Engineering Geology and Hydrogeology* 45, 231–241. <https://doi.org/10.1144/1470-9236/11-048>.
- Massonnet, D.; Feigl, K.L. Radar interferometry and its application to changes in the Earth’s surface.
- Mazzanti, P., Antonielli, B., Sciortino, A., Scancelli, S., & Bozzano, F. (2021). Tracking Deformation Processes at the Legnica Glogow Copper District (Poland) by Satellite InSAR—II: Żelazny Most Tailings Dam. *Land*, 10(6), 654.
- McNairn, H. and Shang, J., 2016. A review of multitemporal synthetic aperture radar (SAR) for crop monitoring. *Multitemporal remote sensing*, pp.317-340.
- Meng, Q.; Li, W.; Raspini, F.; Xu, Q.; Peng, Y.; Ju, Y.; Zheng, Y.; Casagli, N. Time-series analysis of the evolution of large-scale loess landslides using InSAR and UAV photogrammetry techniques: a case study in Hongheyan, Gansu Province, Northwest China. *Landslides* 2020, 18, 251–265, doi:10.1007/s10346-020-01490-8.
- Miano, A., Mele, A., Calcaterra, D., Martire, D. D., Infante, D., Prota, A., & Ramondini, M. (2021). The use of satellite data to support the structural health monitoring in areas affected by slow-moving landslides: a potential application to reinforced concrete buildings. *Structural Health Monitoring*, 1475921720983232.
- Mielke, C.; Boesche, N.K.; Rogass, C.; Kaufmann, H.; Gauert, C.; De Wit, M. Spaceborne Mine Waste Mineralogy Monitoring in South Africa, Applications for Modern Push-Broom Missions: Hyperion/OLI and EnMAP/Sentinel-2. *Remote Sensing* 2014, 6, 6790–6816, doi:10.3390/rs6086790.
- Milillo P, Burgmann R, Lundgren P, Salzer J, Perissin D, Fielding E, Biondi F, Milillo G Space geodetic monitoring of engineered structures: the ongoing destabilization of the Mosul dam Iraq. *Nat Sci Rep*. <https://doi.org/10.1038/srep37408> *New Civil Engineering* (2016).
- Milillo, P., Giardina, G., DeJong, M., Perissin, D., Milillo, G., 2018. Multi-Temporal InSAR Structural Damage Assessment: The London Crossrail Case Study. *Remote Sensing* 10, 287.
- Mills, K. W., & O’Grady, P. (1998). Impact of longwall width on overburden behaviour.
- Mills, K. W., (2009). Subsidence engineering, Chapter 37. In Kininmouth, R. J and Baafi, E. Y (editors) *Australasian Coal Mining Practice*, third edition, Australasian Institute of Mining and Metallurgy, Monograph 12, pp. 874–902.
- Modeste, G., Doubre, C., & Masson, F. (2021). Time evolution of mining-related residual subsidence monitored over a 24-year period using InSAR in southern Alsace, France. *International Journal of Applied Earth Observation and Geoinformation*, 102, 102392.
- Mora, O., Mallorquí, J.J., Broquetas, A. (2003). Linear and nonlinear terrain deformation maps from a reduced set of interferometric SAR images. *IEEE Transactions on Geoscience and Remote Sensing*, 41, 2243-2253.
- Moreira, A., Prats-Iraola, P., Younis, M., Krieger, G., Hajnsek, I. and Papathanassiou, K.P., 2013. A tutorial on synthetic aperture radar. *IEEE Geoscience and remote sensing magazine*, 1(1), pp.6-43.

- Morejón, M.; Andrés, E. Aplicación de modelos teóricos para estimar la subsidencia minera que afecta el área de la Unidad Educativa “La Inmaculada Fe y Alegría” cantón Zaruma; Trabajo de titulación; Carrera de Ingeniería en Minas: Quito, Ecuador, 2019.
- Morra V., Secchi F. A., Assorgia A., (1994). Petrogenetic significance of peralkaline rocks from Cenozoic calc-alkaline volcanism from SW Sardinia, Italy. *Chemical Geology*, 118(1-4), pp. 109-142.
- Mura, J.C., Paradella, W.R., Gama, F.F., Silva, G.G., Galo, M., Camargo, P.O., Silva, A.Q. and Silva, A., 2016. Monitoring of non-linear ground movement in an open pit iron mine based on an integration of advanced DInSAR techniques using TerraSAR-X data. *Remote Sensing*, 8(5), p.409.
- Mura, J.C.; Gama, F.F.; Paradella, W.R.; Negrão, P.; Carneiro, S.; De Oliveira, C.G.; Brandão, W.S. Monitoring the Vulnerability of the Dam and Dikes in Germano Iron Mining Area after the Collapse of the Tailings Dam of Fundão (Mariana-MG, Brazil) Using DInSAR Techniques with TerraSAR-X Data. *Remote Sens.* (2018).
- Murillo, R. ZARUMA, Historia Minera. Identidad en Portovelo; ABYA-YALA: Quito, Ecuador, 2000; Volume 1.
- Musa, Z. N., I. Popescu, and A. Mynett. "A review of applications of satellite SAR, optical, altimetry and DEM data for surface water modelling, mapping and parameter estimation." *Hydrology and Earth System Sciences* 19, no. 9 (2015): 3755-3769.
- Nascimento, F. S., Gastauer, M., Souza-Filho, P. W. M., Nascimento, W. R., Santos, D. C., & Costa, M. F. (2020). Land cover changes in open-cast mining complexes based on high-resolution remote sensing data. *Remote Sensing*, 12(4), 611.
- National Coal Board (NCB). *Subsidence engineer's handbook*. NCB Mining Department; London, 1965 & 1975.
- Necsoiu, M., Walter, G.R., 2015. Detection of uranium mill tailings settlement using satellite-based radar interferometry. *Engineering Geology* 197, 267–277.
- Pappalardo, G.; Mineo, S.; Angrisani, A.C.; Di Martire, D.; Calcaterra, D. Combining field data with infrared thermography and DInSAR surveys to evaluate the activity of landslides: The case study of Randazzo Landslide (NE Sicily). *Landslides* 2018, 15, 1–21. .
- Paradella, W.R., Ferretti, A., Mura, J.C., Colombo, D., Gama, F.F., Tamburini, A., Santos, A.R., Novali, F., Galo, M., Camargo, P.O., Silva, A.Q., Silva, G.G., Silva, A., Gomes, L.L., 2015. Mapping surface deformation in open pit iron mines of Carajás Province (Amazon Region) using an integrated SAR analysis. *Engineering Geology* 193, 61–78.
- Parise, M. A procedure for evaluating the susceptibility to natural and anthropogenic sinkholes. *Georisk Assess. Manag. Risk Eng. Syst. Geohazards* 2015, 9, 272–285. .
- Parise, M.; Vennari, C. A chronological catalogue of sinkholes in Italy: The first step toward a real evaluation of the sinkhole hazard. In *Sinkholes and the Engineering and Environmental Impacts of Karst*. In *Proceedings of the 13th Multidisciplinary Conference on Sinkholes and the Engineering and Environmental Impacts of Karst*, Carlsbad, NM, USA, 6–10 May 2013; Land, L., Doctor, D.H., Stephenson, J.B., Eds.; National Cave and Karst Research Institute, 2013; pp. 383–392.
- Pasci, S., Carmignani, L., Pisanu, G., Sale, V., Ulzega, A., Orru, P., Pintus, C., & Deiana, G. (2010). Note illustrative della carta geologica d'Italia -Foglio 564 Carbonia. Regione autonoma della Sardegna, 272 pp (in italian).
- Pastor, J. L., Tomás, R., Lettieri, L., Riquelme, A., Cano, M., Infante, D., Ramondini M., Di Martire, D. (2019). Multi-Source Data Integration to Investigate a Deep-Seated Landslide Affecting a Bridge. *Remote Sensing*, 11(16), 1878.
- Pawluszek-Filipiak K., A. Borkowski, Integration of DInSAR and SBAS Techniques to Determine Mining-Related Deformations Using Sentinel-1 Data: The Case Study of Rydułtowy Mine in Poland, *Remote Sensing*. 12 (2020) 242.

- Pawluszek-Filipiak, K.; Borkowski, A. Monitoring mining-induced subsidence by integrating differential radar interferometry and persistent scatterer techniques. *Eur. J. Remote Sens.* 2020, 53, 1–3.
- Pellicani, R.; Spilotro, G.; Gutiérrez, F. Susceptibility mapping of instability related to shallow mining cavities in a built-up environment. *Eng. Geol.* 2017, 217, 81–88. .
- Peng, S. S. (1992) *Surface Subsidence Engineering*. Society for Mining, Metallurgy and Exploration: Littleton, Colorado
- Pepe, S.; De Siena, L.; Barone, A.; Castaldo, R.; D’Auria, L.; Manzo, M.; Casu, M.; Fedi, M.; Lanari, R.; Bianco, F.; et al. Volcanic structures investigation through SAR and seismic interferometric methods: The 2011–2013 Campi Flegrei unrest episode. *Remote Sens. Environ.* 2019, 234, 111440.
- Pettorelli, N., Safi, K. and Turner, W., 2014. Satellite remote sensing, biodiversity research and conservation of the future. *Philosophical Transactions of the Royal Society B: Biological Sciences*, 369(1643), p.20130190.
- Pilatasig, L.; Gordón, D.; Palacios, O.; Sánchez, J. *Dominios Litotectónicos Del Sur Del Ecuador y Norte Del Perú*; Technical Report; Proyecto Multinacional Andino Geociencias para las Comunidades Andinas-Ecuador-Perú-Canadá, 2015.
- Pires, F., 1995, Textural and mineralogical variations during metamorphism of the proterozoic itabira iron formation in the quadrilátero Ferrífero, minas gerais, Brazil: *Anais da Academia Brasileira de Ciências*, v. 67, p. 77–106.
- Potts, E.L.J. Ground movement in mining areas. *J. Environ. Plan. Manag.* 2011, 2, 24–32.
- Prakash, A., R. D. Lokhande, and K. B. Singh. "Impact of rainfall on residual subsidence in old coal mine workings." *Journal of environmental science & engineering* 52, no. 1 (2010): 75-80.)
- Pratt, W.; Figueroa, J.; Flores, B. *Geology of the Cordillera Occidental of Ecuador between 3°00, and 4°00, S*. World Bank Min. Dev. Environ. Control Proj. CODIGEM Rep. 1997, 1, 58.
- Przyłucka, M.; Herrera, G.; Graniczny, M.; Colombo, D.; Béjar-Pizarro, M. Combination of conventional and advanced DInSAR to monitor very fast mining subsidence with TerraSAR-X Data: Bytom City (Poland). *Remote Sens.* 2015, 7, 5300–5328. .
- Qiu, Y., Zhang, R., Chou, I.M., Wang, X., Hu, W., Zhang, W., Lu, J., Li, G. and Li, Z., 2021. Boron-rich ore-forming fluids in hydrothermal W-Sn deposits from South China: Insights from in situ Raman spectroscopic characterization of fluid inclusions. *Ore Geology Reviews*, 132, p.104048.
- Renger, F. E., Noce, C. M., Romano, A. W., and Machado, N., 1994, *Evolução Sedimentar Do Supergrupo Minas: 500 Ma. De Registro Geológico No Quadrilátero Ferrífero, Minas Gerais, Brasil: Geonomos.Rev. Geophys.* 1998, 36, 441–500.
- Roberts, D., Wilford, J., & Ghattas, O. (2019). Exposed soil and mineral map of the Australian continent revealing the land at its barest. *Nature communications*, 10(1), 1-11.
- Rodbell, D. T., Delman, E., Abbott, M., Besonen, M. & Tapia, P. The heavy metal contamination of Lake Junín National Reserve, Peru: An unintended consequence of the juxtaposition of hydroelectricity and mining. *GSA Today* 24, 4–10 (2014).
- Rosdi, M.A.H.M.; Othman, A.N.; Abdul, M.A.M.Z.Z.; Yusoff, Z.M. Sinkhole susceptibility hazard zones using GIS and analytical hierarchical process (AHP): A case study of Kuala Lumpur and Ampang Jaya. *Int. Arch. Photogramm. Remote Sens. Spat. Inf. Sci.* 2017, XLII-4/W5, 145–151. .
- Rosen, P.A.; Hensley, S.; Joughin, I.R.; Li, F.K.; Madsen, S.R.; Rodriguez, E.; Goldstein, R.M. Synthetic aperture Radar interferometry. *Proc. IEEE* 2000, 88, 333–382
- Rosiere, C. A., and Chemale, F., 1996, Genesis of banded iron-formations; discussion: *Economic Geology*, v. 91, p. 466–468.
- Rosière, C. A., Spier, C. A., Rios, F. J., and Suckau, V. E., 2008, *The Itabirites of the Quadrilátero Ferrífero and Related High-Grade Iron Ore Deposits: An Overview*:
- Salmi E.F., M. Nazem, M. Karakus, The effect of rock mass gradual deterioration on the mechanism of post-mining subsidence over shallow abandoned coal mines, *International Journal of Rock Mechanics and Mining Sciences*. 91 (2017) 59–71.

- Samsonov S., N. d'Oreye, B. Smets, Ground deformation associated with post-mining activity at the French–German border revealed by novel InSAR time series method, *International Journal of Applied Earth Observation and Geoinformation*. 23 (2013) 142–154.
- Samsonov, S., d'Oreye, N. (2012). Multidimensional time-series analysis of ground deformation from multiple InSAR data sets applied to Virunga Volcanic Province. *Geophysical Journal International*, 191, 1095-1108.
- Sanches, I. D., Filho, C. R. S., and Kokaly, R., 2014, Spectroscopic remote sensing of plant stress at leaf and canopy levels using the chlorophyll 680 nm absorption feature with continuum removal: Sanmiquel, L., Bascompta, M., Vintró, C., & Yubero, T. (2018). Subsidence management system for underground mining. *Minerals*, 8(6), 243.
- Sansosti, E.; Berardino, P.; Manunta, M.; Serafino, F.; Fornaro, G. Geometrical SAR image registration.
- Scheinost, A. C., Schulze, D. G., and Schwertmann, U., 1999, Diffuse reflectance spectra of Al substituted goethite: a ligand field approach: *Clays and Clay Minerals*, v. 47, p. 156–164.
- Schmullius, C. C., and D. L. Evans. "Review article Synthetic aperture radar (SAR) frequency and polarization requirements for applications in ecology, geology, hydrology, and oceanography: A tabular status quo after SIR-C/X-SAR." *International Journal of Remote Sensing* 18, no. 13 (1997): 2713-2722.
- Scifoni, S., Bonano, M., Marsella, M., Sonnessa, A., Tagliafierro, V., Manunta, M., ... & Sciotti, M. (2016). On the joint exploitation of long-term DInSAR time series and geological information for the investigation of ground settlements in the town of Roma (Italy). *Remote Sensing of Environment*, 182, 113-127.
- Sekandari, M., Masoumi, I., Beiranvand Pour, A., M Muslim, A., Rahmani, O., Hashim, M., Zoheir, B., Pradhan, B., Misra, A., and Aminpour, S. M., 2020, Application of Landsat-8, Sentinel-2, ASTER and WorldView-3 Spectral Imagery for Exploration of Carbonate-Hosted Pb-Zn Deposits in the Central Iranian Terrane (CIT): *Remote Sensing*, v. 12, p. 1239.
- Shadbolt, C. H., 1978, Mining subsidence-historical review and state of the art, in Geddes, J. D., ed., *Conference on large ground movements and structures: Cardiff, Wales, July 4-7, 1977*, Proceedings, p. 705-748.
- Sharma, V. K., Azad, R. K., Chowdary, V. M., and Jha, C. S., 2022, Delineation of Frequently Flooded Areas Using Remote Sensing: A Case Study in Part of Indo-Gangetic Basin, in Pandey, A., Chowdary, V. M., Behera, M. D., and Singh, V. P. eds., *Geospatial Technologies for Land and Water Resources Management: Cham*, Springer International Publishing, p. 505–530.
- Silva Rotta, L. H., Alcântara, E., Park, E., Negri, R. G., Lin, Y. N., Bernardo, N., Mendes, T. S. G., and Souza Filho, C. R., 2020, The 2019 Brumadinho tailings dam collapse: Possible cause and impacts of the worst human and environmental disaster in Brazil: *International Journal of Applied Earth Observation and Geoinformation*, v. 90, p. 102119.
- Silverman, B.W. *Density Estimation for Statistics and Data Analysis*; Chapman and Hall: London, UK, 1986.
- Singh K. B., and Singh T. N. 1998. Ground movement over longwall workings in the Kamptee coalfield, India, *Engineering Geology* 50 (1998) 125-139.
- Solari, L.; Barra, A.; Herrera, G.; Bianchini, S.; Monserrat, O.; Béjar-Pizarro, M.; Crosetto, M.; Sarro, R.; Moretti, S. Fast detection of ground motions on vulnerable elements using Sentinel-1 InSAR data. *Geomatics* 2018, 9, 152–174.
- Solari, L.; Del Soldato, M.; Montalti, R.; Bianchini, S.; Raspini, F.; Thuegaz, P.; Bertolo, D.; Tofani, V.; Casagli, N. A Sentinel-1 based hot-spot analysis: Landslide mapping in north-western Italy. *Int. J. Remote Sens.* 2019, 40, 7898–7921.
- Souza, A. H. de, Krüger, F. L. von, Araújo, F. G. da S., and Mendes, J. J., 2021, Mineralogical Characterization Applied to Iron Ore Tailings from the Desliming Stage with Emphasis on Quantitative Electron Microscopy (QEM): *Materials Research*, v. 24.
- Spier, C. A., de Oliveira, S. M. B., and Rosière, C. A., 2003, Geology and geochemistry of the Águas Claras and Pico Iron Mines, Quadrilátero Ferrífero, Minas Gerais, Brazil: *Mineralium Deposita*, v. 38, p. 751–774.

- Sunwoo, C.; Song, W.K.; Ryu, D.W. A case study of subsidence over an abandoned underground limestone mine. *Geosyst. Eng.* 2010, 13, 147–152. .
- Syifa, M., Park, S. J., Achmad, A. R., Lee, C.-W., and Eom, J., 2019, Flood Mapping Using Remote Sensing Imagery and Artificial Intelligence Techniques: A Case Study in Brumadinho, Brazil: *Journal of Coastal Research*, v. 90, p. 197–204.
- Taheri, K.; Shahabi, H.; Chapi, K.; Shirzadi, A.; Gutiérrez, F.; Khosravi, K. Sinkhole susceptibility mapping: A comparison between Bayes-based machine learning algorithms. *Land Degrad. Dev.* 2019, 30, 730–745. .
- Tajduś, K.; Sroka, A.; Misa, R.; Hager, S.; Rusek, J.; Dudek, M.; Wollnik, F. Analysis of Mining-Induced Delayed Surface Subsidence. *Minerals* 2021, 11, 1187. <https://doi.org/10.3390/min11111187>
- Tempfli, K., Huurneman, G., Bakker, W., Janssen, L. L., Feringa, W. F., Gieske, A. S. M., ... & Woldai, T. (2009). Principles of remote sensing: an introductory textbook. International Institute for Geo-Information Science and Earth Observation.
- Teng, H., Xu, J., Xuan, D., & Wang, B. (2016). Surface subsidence characteristics of grout injection into overburden: case study of Yuandian No. 2 coalmine, China. *Environmental Earth Sciences*, 75(6), 530.
- Tessitore S., Di Martire D., Mondillo N., Ammirati L., Boni M., Calcaterra D. (2018). Detection of Subsidence by Radar Interferometric Data in the Seruci-Nuraxi Figus Coal Mine Area (Sardinia, Italy). *IAEG/AEG Annual Meeting Proceedings*. Volume 3 pages 51-5.
- Thompson, F., de Oliveira, B. C., Cordeiro, M. C., Masi, B. P., Rangel, T. P., Paz, P., Freitas, T., Lopes, G., Silva, B. S., S. Cabral, A., Soares, M., Lacerda, D., dos Santos Vergilio, C., Lopes-Ferreira, M., et al., 2020, Severe impacts of the Brumadinho dam failure (Minas Gerais, Brazil) on the water quality of the Paraopeba River: *Science of The Total Environment*, v. 705, p. 135914.
- Todd, A.L.; Ivey-Burden, L. A method of mapping sinkhole susceptibility using a geographic information system: A case study for interstates in the karst counties of Virginia. Available online: https://ntlrepository.blob.core.windows.net/lib/55000/55200/55267/UVA_2013-04.pdf (accessed on 13 May 2020).
- Tong, L.; Liu, L.; Qiu, Y.; Liu, S. Tunneling in abandoned coal mine areas: Problems, impacts and protection measures. *Tunn. Undergr. Sp. Technol.* 2013, 38, 409–422
- Ullo, S.L.; Addabbo, P.; Di Martire, D.; Sica, S.; Fiscante, N.; Cicala, L.; Angelino, C.V. Application of DInSAR Technique to High Coherence Sentinel-1 Images for Dam Monitoring and Result Validation Through in Situ Measurements. *IEEE J. Sel. Top. Appl. Earth Obs. Remote Sens.* 12, 875–890. (2019).
- Ünver, B., and M. S. Ünal. "Analysis of a possible root cause and mechanism for Soma mine disaster." *Journal of Mining and Environment* 10, no. 1 (2019): 1-26.
- URGENTE: Nuevo hundimiento en Zaruma activa al COE cantonal—MachalaMovil. Available online: <https://machalamovil.com/urgente-nuevo-hundimiento-en-zaruma-activa-al-coe-cantonal/> (accessed on 13 May 2020).
- USGS EROS Archive - Sentinel-2 - Comparison of Sentinel-2 and Landsat. U.S. Geological Survey <https://www.usgs.gov/centers/eros/science/usgs-eros-archive-sentinel-2-comparison-sentinel-2-and-landsat> (accessed on Jan 16, 2022).
- Van der Meer, F. D., van der Werff, H. M. A., van Ruitenbeek, F. J. A., Hecker, C. A., Bakker, W. H., Noomen, M. F., van der Meijde, M., Carranza, E. J. M., Smeth, J. B. de, and Woldai, T., 2012, Multi- and hyperspectral geologic remote sensing: A review: *International Journal of Applied Earth Observation and Geoinformation*, v. 14, p. 112–128.
- Van Sambeek, L.L. Measuring Surface subsidence at Colonsay, Saskatchewan, Potash Mine. In *Proceedings of the Rock Mechanics and Ground Control in the Soft Rock and Coal Industries Workshop*; Canadian Institute of Mining, Metallurgy, and Petroleum: Saskatoon, SK, Canada, 1997.

- Van Thournout, F.; Salemink, J.; Valenzuela, G.; Merlyn, M.; Boven, A.; Muchez, P. Portovelo: A volcanic-hosted epithermal vein-system in Ecuador, South America. *Miner. Dep.* 1996, 31, 269–276.
- Vergilio, C. dos S., Lacerda, D., Oliveira, B. C. V. de, Sartori, E., Campos, G. M., Pereira, A. L. de S., Aguiar, D. B. de, Souza, T. da S., Almeida, M. G. de, Thompson, F., and Rezende, C. E. de, 2020, Metal concentrations and biological effects from one of the largest mining disasters in the world (Brumadinho, Minas Gerais, Brazil): *Scientific Reports*, v. 10, p. 5936.
- Vervoort, A. (2020). Long-term impact of coal mining on surface movement: Residual subsidence versus uplift. *Min. Rep. Glückauf*, 156, 136-141.
- Vick, S.: *Planning, design, and analysis of tailings dams*. Publishers, Vancouver (1990).
- Vikentyev, I.; Banda, R.; Tsepin, A.; Prokofiev, V.; Vikentyeva, O. Mineralogy and formation conditions of Portovelo-Zaruma gold-sulphide vein deposit, Ecuador. *Geochem. Mineral. Petrol.* 2005, 43, 148–154.
- Villegas T., Nordlund E., Dahner-Lindqvist C. 2011. Hangingwall surface subsidence at the Kiirunavaara Mine, Sweden. *Engineering Geology*, 121, 18–27.
- Vu Khac D., Thanh Dong Nguyen, Ngoc Hung Dao, Thi Loi Duong, Xuan Vinh Dinh & Christiane Weber (2021) Land subsidence induced by underground coal mining at Quang Ninh, Vietnam: persistent scatterer interferometric synthetic aperture radar observation using Sentinel-1 data, *International Journal of Remote Sensing*, 42:9, 3563-3582
- Vušović, N., & Vlahović, M. (2020). Prediction of surface subsidence and deformations due to the underground coal mining. *Mining and Metallurgy Engineering Bor*, (3-4), 37-56.
- Wang B, Cui CQ, Zhao YX, Yang B, Yang QZ (2018) Carbon emissions accounting for China's coal mining sector: invisible sources of climate change. *Nat Hazards* 99:1345–1364
- Wasowski, J. and Bovenga, F., 2022. Remote sensing of landslide motion with emphasis on satellite multi-temporal interferometry applications: an overview. *Landslide Hazards, Risks, and Disasters*, pp.365-438.
- Werner, C., Wegmuller, U., Strozzi, T., Wiesmann, A. (2003). Interferometric point target analysis for deformation mapping. *Proceeding of IEEE Geoscience and Remote Sensing Symposium. IGARSS*, Toulouse, France, 7, 4362-4364.
- Whittaker B N and Reddish D J. *Subsidence occurrence, prediction and control*. Elsevier, Amsterdam 1989.
- World Information Service on Energy Uranium Project: Chronology of major tailings dam failures. Available: <https://www.wise-uranium.org/mdaf.html>. Accessed: 04/07/2020.
- Wu, Q. and Guo, L.Z.N., 2009. Precise segmentation of bone marrow cells by using multispectral imaging analysis techniques. *Intell Eng Serv*, 2(3), pp.36-43.
- Xie, P., Luo, Y., Wu, Y., Gao, X., Luo, S., & Zeng, Y. (2020). Roof deformation associated with mining of two panels in steeply dipping coal seam using subsurface subsidence prediction model and physical simulation experiment. *Mining, Metallurgy & Exploration*, 37(2), 581-591.
- Xu X., C. Ma, D. Lian, D. Zhao, Inversion and Analysis of Mining Subsidence by Integrating DInSAR, Offset Tracking, and PIM Technology, *Journal of Sensors*. 2020 (2020) 1–15.
- Xue, J. and Su, B., 2017. Significant remote sensing vegetation indices: A review of developments and applications. *Journal of sensors*, 2017.
- Yan, D., Zhang, H., Li, G., Li, X., Lei, H., Lu, K., Zhang, L., and Zhu, F., 2022, Improved Method to Detect the Tailings Ponds from Multispectral Remote Sensing Images Based on Faster R-CNN and Transfer Learning: *Remote Sensing*, v. 14, p. 103.
- Yang, B., Bai, Z. & Zhang, J. Environmental impact of mining-associated carbon emissions and analysis of cleaner production strategies in China. *Environ Sci Pollut Res* 28, 13649–13659 (2021). <https://doi.org/10.1007/s11356-020-11551-z>
- Ye, S., Luo, Y., Wu, J., Yan, X., Wang, H., Jiao, X., & Teatini, P. (2016). Three-dimensional numerical modeling of land subsidence in Shanghai, China. *Hydrogeology Journal*, 24(3), 695-709.
- Yidana, Sandow M., Duke Ophori, and Bruce Banoeng-Yakubo. "A multivariate statistical analysis of surface water chemistry data—The Ankobra Basin, Ghana." *Journal of Environmental Management* 86.1 (2008): 80-87.

- Yue, H., Liu, G., Guo, H., Li, X., Kang, Z., Wang, R., & Zhong, X. (2011). Coal mining induced land subsidence monitoring using multiband spaceborne differential interferometric synthetic aperture radar data. *Journal of Applied Remote Sensing*, 5(1), 053518.
- Zakhvatkina, N., Smirnov, V. and Bychkova, I., 2019. Satellite sar data-based sea ice classification: An overview. *Geosciences*, 9(4), p.152.
- Zaruma se hunde por la minería clandestina. *El Comercio*. Available online: <http://www.elcomercio.com/actualidad/zaruma-hundimientos-mineria-clandestina-escuela.html> (accessed on 13 May 2020).
- Zhang, Z., Wang, C., Tang, Y., Zhang, H. and Fu, Q., 2015. Analysis of ground subsidence at a coal-mining area in Huainan using time-series InSAR. *International Journal of Remote Sensing*, 36(23), pp.5790-5810.
- Zhao, Chaoying, Zhong Lu, and Qin Zhang. "Time-series deformation monitoring over mining regions with SAR intensity-based offset measurements." *Remote Sensing Letters* 4, no. 5 (2013): 436-445.
- Zhao, X., Pan, S., Sun, Z., Guo, H., Zhang, L., & Feng, K. (2021). Advances of satellite remote sensing technology in earthquake prediction. *Natural Hazards Review*, 22(1), 03120001.
- Zhou, DW., Wu, K., Cheng, GL. et al. Mechanism of mining subsidence in coal mining area with thick alluvium soil in China. *Arab J Geosci* 8, 1855–1867 (2015).
- Zingano A., A. Weiss, Subsidence over room and pillar retreat mining in a low coal seam, *International Journal of Mining Science and Technology*. 29 (2019) 51–57.

Acknowledgments

First and foremost I am extremely grateful to Prof. Domenico Calcaterra, his invaluable supervision, support, and tutelage during the years of my Ph.D. degree for the opportunity and means to complete my Ph.D. project. My gratitude to the Department of Earth, Environmental and Resource Sciences for the opportunity to undertake my studies. Thanks are due to the Ph.D. coordinator Prof. Morra. I would like to express my gratitude to my advisor Dr. Nicola Mondillo who believed in me and awarded me with this Ph.D. project, even though he hardly knew me at that time. His remarks, his objective criticism, his encouragements, and his advice were the main engine for my growth, as a researcher. I would like to thank Dr. Diego Di Martire for their invaluable advice, continuous support, and patience during my Ph.D. study. His immense knowledge and plentiful experience have encouraged me in all the time of my academic research and daily life. I wish to acknowledge the help provided by the technical and support staff in the mining company Carbosulcis S.p.A. My gratitude extends to my industrial advisor Dr. Fabrizio Bordicchia his invaluable supervision, support, and tutelage during my period in the mining company. I would also like to show my deep appreciation to Ing. Elisabetta Fois who helped to frame me in the company. I would like to thank the British Geological Survey and my tutor Dr. Alessandro Novellino for their technical support on my study. Many thanks are due to DARES technology for the support to DInSAR elaborations. Gratefully acknowledged to C.U.G.RI (Consortium between the Federico II University of Naples and the University of Salerno for the Prediction and Prevention of Major Hazards) for supporting this research with hardware/software facilities. I am also grateful for the precious support given by the reviewers for their valuable observations and suggestions to improve the quality of the thesis.

Appendix 1

1. SUBSIDENCE software and Coherent Pixels Technique (CPT)

The algorithm implemented by Mora et al., 2003 - Coherent Pixels Technique (CPT) at the Remote Sensing Laboratory (RSLab) of the Universitat Politècnica de Catalunya (UPC), considered one of the top universities in terms of research of Radar Technology in the world. The developed SUBSIDENCE Satellite Radar software can process data coming from all different SAR sensors and acquired through different mode settings. CPT algorithm can extract from a stack of differential interferograms the deformation evolution over wide areas during large periods. The former is achieved thanks to the coverage provided by current SAR satellites, like ESA's Sentinel-1, Japanese satellites ALOS-1 and ALOS-2, Terrasar-X, Radarsat-1 and 2 and Cosmo-SkyMed, while the latter is due to the large archive of images acquired since 1992 (ERS1-2). The interferometric chain is divided into two phases: PRISAR and CPT.

The first refers to the registration and generation of interferograms, coherence maps and differential phase matrices. PRISAR chain is in charge of preparing the inputs of the second phase. The latter was implemented in Subsoft where the advanced DInSAR algorithm is used. The Radar chain algorithm consists of four main parts (Fig. A1):

- 1) Pixel selection of distributed and point-like scatterers. Radar chains can work with different methods and provide deformation measures at different resolutions to maximize the total number of processed points.
- 2) Linear estimation process. This step estimates the main component of the displacement and the point height.
- 3) Estimation and removal of atmospheric artifacts and retrieval of the temporal evolution of the deformation also called non-linear deformation.
- 4) Geocoding and projection of the maps are saved in different format files, such as Google Earth or GIS programs, to increase the flexibility and make easier the interpretation and representation of the final products.

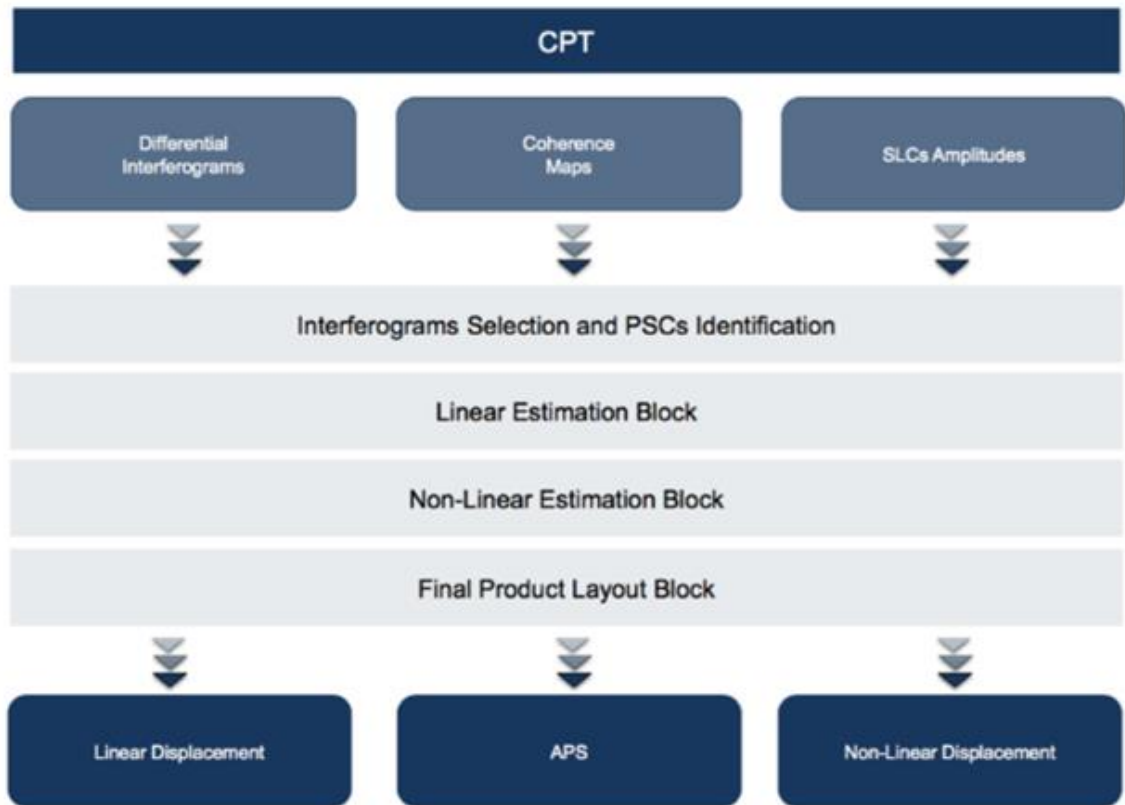


Figure A1. CPT general workflow. The outcomes correspond to maps of linear and non-linear deformations.

The generation of the best interferogram set aims to identify the minimum number of interferograms in the stack which have the maximum quality overall. To do the selection, from all the available images, the spatial baseline, the temporal baseline (Bt), and the Doppler frequency (Df) are considered. To estimate the perpendicular baseline values (Bn) a reference image (master) is selected (Figure A2).

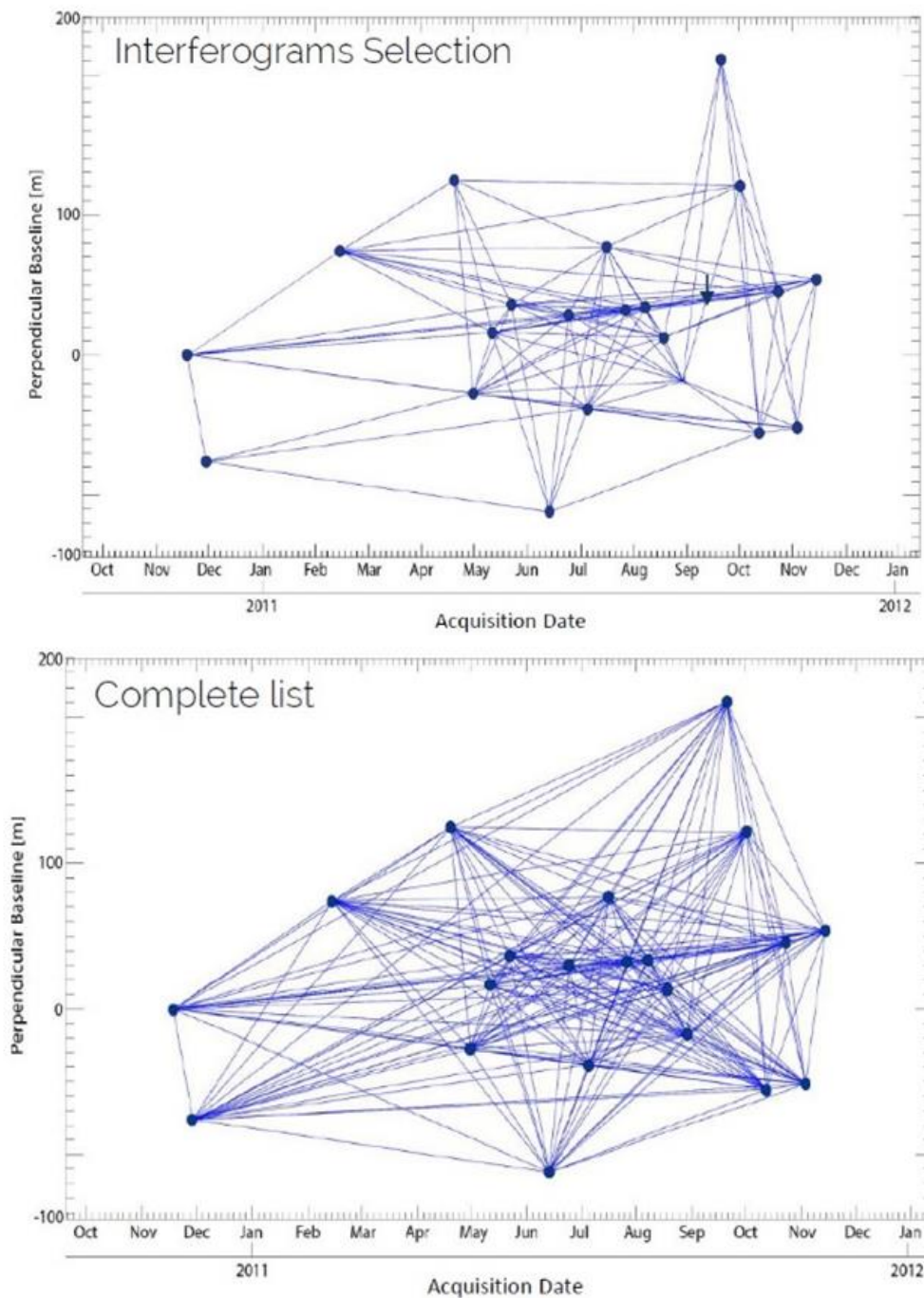


Figure A2. Interferogram selection (top) considering the complete list available (down) to minimize geometrical and temporal decorrelation.

Generally, the image is used as the reference in the co-registering process. After that, interferograms selection is done through Delaunay triangulation of the available images in the space, so every connecting pair of images represents an interferogram. The pixel selection is a very important step to obtain reliable results. Only pixels characterized by a considerable phase quality are selected. There are several criteria for selecting pixels, one based on the coherence stability (Berardino et al., 2002), the other one based on the amplitude dispersion (Ferretti et al., 2001). More recently, also

the Temporal Sublook Coherence method (TSC, Iglesias, et al., 2015) has been produced. The first one is based on the spatial coherence estimator (Seymour et al., 1994) and the pixel will be selected if it shows a coherence higher than an assigned threshold; the second one, as a PS-like method, exploits the dispersion index, where all the pixels characterized by a D_a value below a certain threshold are selected; the latter is a selection method able to detect point-like scatterer analyzing the spectral properties of the scattered signal. The advantage of the PS selection based on the amplitude dispersion is that there is no need of applying a radiometric calibration. Hence, in this case, pixel selection is carried out by exploiting the spectral properties of point-like scatterers. The last step consists of the phase analysis, to calculate their linear deformation time series within the observation period. In this case, the CPT algorithm employs the Delaunay triangulation allowing the connection between neighboring pixels, and, after that, to evaluate the phase increment between two neighboring pixels. CPT algorithm applies both the Delaunay and the Spider-Web triangulation simultaneously (Figure A3).

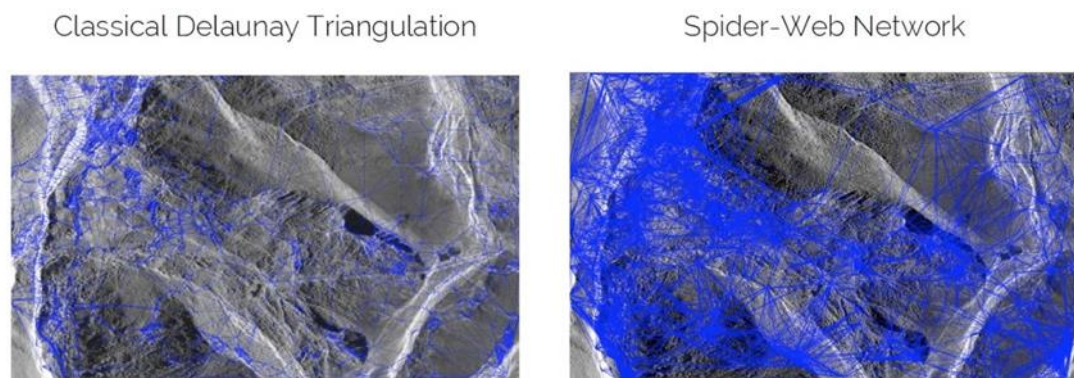


Figure A3. implementation of CPT triangulation methods to cancel the phase offsets between interferograms.

Finally, an integration process is necessary to obtain the velocity values for each pixel: it is necessary to identify a control point (named seed) characterized by linear velocity and height well known. A good distribution of control points helps to reduce the offsets that could appear among zones badly connected. Depending on the chosen threshold, selected pixels may vary in a wide quality range, and consequently, so it will the quality of the estimations on the increments of the linear parameters. Selected pixels are divided into different layers according to their quality (Blanco et al., 2006). After that, beginning with the top layer, the linear block is iteratively executed by adding successive layers, so the obtained absolute values of each layer act as the seed

values to the following integration process. In this way, the results obtained with the high-quality layers are preserved and the estimation of the low-quality layers improves. Consequently, multi-layer processing improves linear results and rises pixel density while providing a quality label for each one. Subsequently, the non-linear component has been calculated to obtain the complete evolution of deformation. The first step of the non-linear model consists of the calculation of the phase residues $\varphi_{residue}$ (equation 6), obtained by subtracting the absolute linear phase model φ_{model} from the original interferometric phases φ for the selected pixels:

$$\varphi_{residue} = \varphi - \varphi_{model}$$

The residual phases are calculated only in correspondence with reliable pixels and consist of two conditions:

- a) Atmospheric perturbations. This term can be explained as a low spatial frequency signal in each image due to its correlation distance. However, for each acquisition date atmospheric conditions can be considered random.
- b) Non-Linear deformation. This term can be assumed to present a narrower correlation window in space (or at least much narrower than atmospheric artifacts) and a low pass behavior in time. Starting from these considerations is possible to separate the atmospheric artifacts from the non-linear deformation by applying a filtering process in both spatial and temporal domains to obtain the time-series of the deformation.

Figure A4 shows the end of the analysis of the time-series deformation and its temporal evolution for each PS individuated can be computed combining the estimated linear model and the non-linear component.

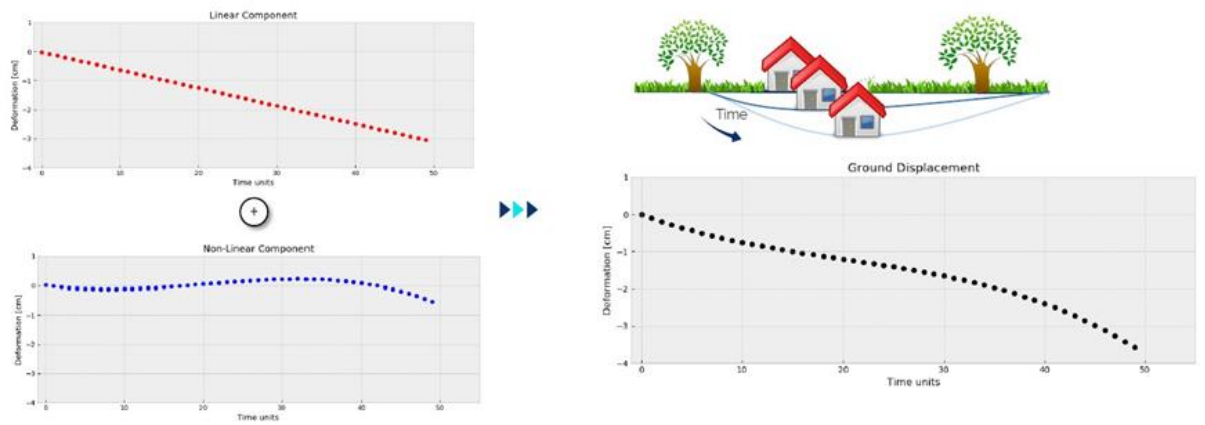


Figure A4. Time-series evolution with the integration of linear and non-linear components.

SUBSIDENCE outcomes can be exported in the .csv format allowing the reading, consultation and analysis of them. Geocoded data can be also exported in the ESRI Shapefile (.shp) format which is suitable for loading the associated features on GIS platforms and web maps. For each point (PS), the output files give information on height (meters a.s.l.), incidence angle (degrees), rate of displacement (cm/year), the quality of the InSAR measurement and the accumulated displacement for each satellite acquisition date (cm).